Master's thesis

NTNU
Norwegian University of Science and Technology
Faculty of Engineering
Department of Geoscience and Petroleum

Anne Hyllseth

# Experimental Analysis and Characterization of Deep-Sea Sediment Samples From Loki's Castle and Mohn's Treasure

Master's thesis in Technical Geosciences
Supervisor: Kurt Aasly
July 2021

NTNU
Norwegian University of
Science and Technology

Anne Hyllseth

# Experimental Analysis and Characterization of Deep-Sea Sediment Samples From Loki's Castle and Mohn's Treasure

Master's thesis in Technical Geosciences
Supervisor: Kurt Aasly
July 2021

Norwegian University of Science and Technology
Faculty of Engineering
Department of Geoscience and Petroleum

NTNU
Norwegian University of
Science and Technology

# Summary

The world is heading for a green energy transition. Facilitating this change will require significant amounts of metals such as copper, zinc and cobalt. As terrestrial mines are exploited, progressively more land area are restricted to industrial usage. In addition to creating an incentive for land conflicts, the continuous exploitation of terrestrial deposits leads to the depletion of these mines.

As a consequence new sources for such resources are a necessity for the future increase in electrification and energy demand . The craving for such resources has led to a continuous search for natural resources, and within recent years the search has pursued the deep seas.

This thesis is written as part of the MarMine research project, which aim is to contribute with knowledge and research of the possible deep-sea mineral deposits within the Norwegian exclusive economic zone. Sediment samples from two possible marine mineral deposits located on the ultra-slow arctic mid-ocean ridge have been studied through this thesis. The two sites represent two different types of marine mineral deposits, one active hydrothermal field, Loki's Castle, and one extinct field, Mohn's Treasure.

Sediment from the two sites was collected by push-core and scoop sampling. The sediment consist of a mix of three different types of marine sediments; lithogenous, biogenous, and hydrogenous. A method proposed by Metz et al. (1988) was utilized to estimate the proportion of hydrothermal material in the sediment samples. The method showed hydrothermal components close to 100% in the sediments from Loki's Castle, while the sediments from Mohn's Treasure showed hydrothermal components between 9-28%. This is due to Loki's Castle being an active hydrothermal field where black smoke settles rapidly on the surrounding seafloor. Mohn's treasure is an extinct field, and sediments transported from the continental shelf have gradually covered the site, causing a higher degree of mixing with terrestrial sediment.

Iron concentrations from Mohn's Treasure showed a positive correlation with the theoretical hydrothermal component. This is concluded to be an indicator of hydrothermal activity affecting the composition of the sediments. The presence of a magnetic anomaly at the site further confirms that the site previously has been hydrothermally active. Evidence from automated mineralogy of fragments from Mohn's Treasure is also part of the argument. This fragment shows evidence of iron-rich fluids interacting with the bedrock at the site.

Chlorite concentrations at Mohn's treasure also showed a positive correlation with the hydrothermal component. As chlorite is a low-temperature hydrothermal alteration product, chlorite is an indicator of low-temperature fluids percolating the sediments. Two possible explanation for the observation of this phase is proposed. Either, late-stage hydrothermal venting has occurred as the temperature of the hydrothermal system has cooled. Low-temperature fluids would then have percolated the recently deposited sediments, leading to a low-temperature alteration. The other possibility is that area represents a diffuse venting site, which is related to a larger extinct hydrothermal field.

The sediments from Loki's Castle are concluded to be metalliferous hydrogenous sediments, with little mix of terrestrial compounds. This is due to the elevated iron concentrations and elevated hydrothermal components of the samples. Base metal grades recorded from the site place Loki's Castle in the category of mafic host rock lithology. The deposit is still believed to have a sedimental influence, but not strong enough to affect the Pb-grades of the deposit. Based on the base metal ratios, the deposits can also be described as a Cu-Zn deposit.

# Sammendrag

Verden står i dag overfor det grønne skiftet. Ved overgang til grønn energi, vil behovet for metaller som kobber, sink og kobolt øke. I tilleg til å skape et insentiv for arealkonflikter fører den kontinuerlige utnyttelsen av landbaserte forekomster til en utarming av forekomstene. Som en konsekvens er nye kilder for slike ressuser nødvendige for den framtidige elektrifisering og det framtidige energibehovet.

Disse forholdene har ført til en kontinuerlig jakt å naturressurser. Denne jakten har ført til at søkelyset i de seinere årene er blitt rettet mot slike ressurser i havdypene.

Denne oppgaven er skrevet som en del av forskningsprosjektet MarMine, som har som mål å bidra med kunnskap og forskning om mulige dyphavsmineralforekomster innenfor utvidet norsk sokkel. Sedimentprøver fra to mulige marine mineralforekomster på den arktiske midthavsryggen, er studert gjennom denne oppgaven. De to stedene representerer to forskjellige typer marine mineralforekomster, et aktivt hydrotermisk felt, Lokeslottet og et inaktivt felt, Mohnsskatten.

Sediment fra de to forekomstene ble samlet inn ved ”push-core” og ”scoop sampling”. Sedimentene består av en blanding av tre forskjellige typer marine sedimenter; litogene, biogene og hydrogene sediment. En metode foreslått av Metz et al. (1988) ble brukt til å estimere andelen hydrotermalt materiale i sedimentprøvene. Metoden viste hydrotermale komponenter nær 100 % i sedimentene fra Lokeslottet, mens sedimentene fra Mohnsskatten viste hydrotermale komponenter mellom 9-28 %. Dette skyldes at Lokeslottet er et aktivt hydrotermisk felt der svart skortsteinsrøyk raskt avsettes på den omkringliggende havbunnen. Mohnsskatten er et inaktivt felt, og sedimenter som har blitt transportert fra kontinentalsokkelen har gradvis blitt avsatt på stedet, og forårsaket høyere grad av blanding med landbasert sediment.

Jernkonsentrasjoner fra Mohnsskatten viste positiv korrelasjon med den teoretiske hydrotermale komponenten. Dette konkluderes med å være en indikator på at hydrotermal aktivitet har påvirket sammensetningen av sedimentene. Tilstedeværelsen av en magnetisk anomali på stedet bekrefter videre at stedet tidligere har vært et område preget av hydrotermal aktivitet. Bevis fra automatisert mineralogi av fragmenter fra Mohnsskatten er også en del av argumentet. Dette fragmentet viser bevis på at jernrike væsker har samhandlet med bergartene på stedet.

Klorittkonsentrasjoner ved Mohnsskatten viste også en positiv sammenheng med den hydrotermale komponenten. Ettersom kloritt er et hydrotermalt lav-temperaturs omvandlingsprodukt, er kloritt en indikator på at lavtemperaturvæsker har sirkulert gjennom sedimentene. To mulige forklaringer på observasjonen av denne kloritt foreslås. Enten har sen hydrotermal sirkulering forekommet mens temperaturen i det hydrotermale systemet har blitt avkjølt. Væsker ved lav temperatur ville da ha omvandlet de nylig avsatte sedimentene, noe som førte til en lav temperatur omvandling av sedimentene. Den andre muligheten er at området representerer et diffus utsiving av hydrotermale væslker, som er relatert til et større inaktivt hydrotermalt felt.

Sedimentene fra Lokeslottet konkluderes med å være metallholdige hydrogene sedimenter, med liten innblanding av landbaserte sedimenter. Denne konklusjonen trekkes basert på de forhøyede jernkonsentrasjonene og forhøyede hydrotermale komponenter i prøvene. Konsentrasjon av basemetaller i området plasserer Lokeslottet i en mafisk kategori, selv om forekomsten tidligere er blitt beskrevet som å ha blitt påvirket av begravde lag av sedimenter. Disse begravde sedimentpakkene er konkludert med å ikke påvirke konsentrasjonen av bly i forekomsten, og kan dermed klassifiseres som en Cu-Zn forekomst.

# Preface

This thesis is part of a five year intergrated master within technical geosciences and is carried out at the department of geoscience and petroleum at NTNU. The thesis is written as part of the MarMine research project and the research cruise that took place in 2016.

First of all i would like to express my gratitude to my supervisor, associated professor Kurt Aasly for valuable discussions, critical questions and for guiding me through my last year at NTNU.

This project would not have been completed without the help and guidance from the people at the NTNU laboratories, and I would like to extend my gratitude to senior engineers Torill Sørløk and Laurentius Tijhuis at the chemical/mineralogical laboratory.

I would also like to thank my family for supporting me through my studies at NTNU. A special thanks to Sondre Torset for motivating me through the final weeks of writing.

*Trondheim 08.07.2021*
Anne Hyllseth

# Contents

# List of Tables

# List of Figures

Chapter 1

# Introduction

In a world with a growing population and an ever growing demand for energy, facilitating a steady supply of raw materials for green technologies will be essential. Whilst terrestrial mines will be able to provide some of these materials, there is increased conflict between need for materials, and the consequences of such processes. These conflicts include aspects such as the re-regulation of land, and the dumping of waste materials. Increased use of re-cycling will also help feed the demand, but the number of people and businesses that need green energy supply means that more material is needed. This is where marine mineral deposits could provide a solution. The technological challenges are still many for conducting such operations, but mapping out the potential for these resources could become key in planning the expansion of green technologies.

Increasing metal prices as well as increasing industrialisation has lead the mining industry to look for resources at new places, such as at the seabed. A possible source of such deposits are found in relation to hydrothermal fluid activity on the seabed, in areas associated with tectonic extensional regimes.

Several localities on the Norwegian Extended Continental shelf have shown presence of such hydrothermal sources and related mineralisations on the seafloor (Pedersen et al. (2010b), Ellefmo et al. (2019)). This thesis will study samples from the overlying sediment of two such sites located on the Norwegian extended continental shelf and within the Norwegian Exclusive economic Zone. The samples are collected from the Loki's Castle and Mohn's Treasure localities and are put through a series of laboratory tests, in order to evaluate their composition and what information the sediments can give about the deposits.

Some of the geological theory as to why these localities might be interesting is described, before a run through of the materials and methods used is provided. The results form the basis for a discussion where it will be evaluated how the findings may contribute to increased understanding of the deposits found within the Norwegian economic zone.

## 1.1 Historic Perspective

Deep sea marine mineral deposits has long been known to scientists, however it is within recent years it has gotten the attention as a possible profitable resource for raw materials. With increasing interest in marine mineral resources, technological development, as well as the establishment of the International Seabed Authority (1993), extraction of marine minerals has now become a reality.

The history of deep sea mining starts with the discovery of metalliferrous sediments by the HMS Challenger expedition in the 1870's. Here, a dredge on the seabed of the east pacific rise, collected

sediments containing anomalous high iron and low aluminium contents(Cherkashov, 2017). These data was registered, but not given a proper explanation at that time.

Later in the 1880's anomalies in temperature and salinity in the red sea was registered by a Russian expedition(Cherkashov, 2017). However, these findings were not connected to hydrothermal activity and was overlooked. Metalliferous sediments from the East Pacific Rise was also collected in the 1940's by the USS Carneige, but was again not studied further.

When the theory of plate tectonics emerged in the beginning of the $20^{th}$ century, hydrothermal activity on the seabed became an important evidence for such movements in the crust (Cherkashov, 2017)). In the 1960's and 70's the connection between metalliferrous sediments, hydrothermal activity and plate tectonics was made, leading to increasing research within the field (e.g Boström and Peterson (1969), Boström et al. (1972)). Through the 80's and 90s numerous exploration programs started mapping out the seabed and related seafloor deposits, such as the Deep-Sea Drilling Project (1966-1983) and the Ocean Drilling Program (1983-2003) (Gurvich, 2006).

In 1993 the International Seabed Authority (ISA) was established as an independent autonomous organization that regulate the UN convention International law of the sea. The ISA lays the foundation for exploration and exploitation of marine minerals in international waters. The purpose of the ISA is to organize and control the exploitation of marine mineral resources that are within international waters, making these resources benefit the whole population.

From a Norwegian perspective, the resources that lie within the Norwegian exclusive economic zone and in the are of particular interest. The exploration for marine mineral resources on the Norwegian extended continental shelf began as a consequence of increased global interest in mapping of the seabed, as well as international findings of marine mineral resources in relation to extensional tectonic regimes. In 2008 the first active hydrothermal vent field was discovered on the Arctic Mid-Ocean Ridge (AMOR), which was named Loki's Castle (Pedersen et al., 2010a). Through the first decade of the 21st century, a number of other hydrothermal vent fields have also been discovered on the AMOR (Ellefmo et al. (2019)). In this thesis,samples gathered as part of NTNUs MarMine research project is to be analysed in hope that it will contribute to a better understanding of the marine mineral deposits that are located on the Norwegian extended continental shelf.

## 1.2 Project Description

The goal of this thesis is to evaluate the physical and chemical properties of sediments from Loki's Castle and Mohn's Treasure SMS deposits located on the Norwegian Extended Continental Shelf. These observations could be used to better describe the deposits, and perhaps give information about the influence of the tectonic setting and proximity to the continental shelf. The sediments typically overlie the deposits and will have to be removed in order to access the whole deposit. If the sediments are of economic value, the production of them could increase the net value of the deposit.

A characterisation of the sediments will also give insight in what to expect for sediments related to similar types of deposits, hence contribute to a better understanding of SMS deposits in general.

These objectives will be realized through a number of laboratory tests and methods, to characterise the geochemical signatures of the sediment samples. The laboratory analysis will emphasize on the content of base metals and precious metals, such as Cu, Zn, Ag and Au as well as sulphur and iron, so that the economic potential of the sediments can be evaluated. The analyses will also focus on the presence of other hydrothermal phases and traces of hydrothermal activity.

## 1.3 Outline

The thesis consist of 7 chapters, which is each divided into several sections and sub-sections. Chapter 1 gives an introduction to the topic, as well as describing the necessity of the work. In Chapter 2, background information of the sample locations, as well the sample collection procedure will be explained. The regional geology related to the sites is also presented. The relevant background theory is presented in Chapter 3. Laboratory material and methods used to characterise the samples is presented in Chapter 4. Chapter 5 presents the results from the laboratory tests, as well as observations from optical microscopy. In Chapter 6 a discussion related to the observations and results is made. Conclusion of the thesis is presented in chapter 7 along with suggestions for future work.

Chapter 2

# Background

## 2.1 Geological Setting

The Arctic-Mid-Ocean Ridge (AMOR) stretches from the north side of Iceland, through the Norwegian sea and into the Eurasia Bassin, north of Russia (Figure 2.1). With a spreading rate of between $15 - 20mma^{-1}$ it classifies as an ultra-slow spreading ridge (Pedersen et al. (2010b)).The ridge is looked upon as an extension of the Mid-Atlantic Ridge (MAR), only disconnected by the island of Iceland. As can be seen on figure 2.1, the ridge may be divided into six sub-segments after Pedersen et al. (2010b): (1) Kolbeinsy Ridge (KR), (2) Mohns Ridge (MR), (3) Knipovich Ridge (KnR), (4) Molloy Ridge/Fracture Zone (MFZ), (5) the Lena Trough (LT) and (6) Gakkel Ridge (GR).

It was earlier believed that ultraslow-spreading ridges did not supply favourable conditions for extensive hydrothermal activity, due to the low geothermal gradient in such settings (Alt (1995)). However, all along the 4000km long Arctic mid-ocean ridge and sub-segments, hydrothermal activity has been observed in the form of larger hydrothermal fields, extinct fields and as single hydrothermal plumes. Sulfide deposits have also been discovered at certain locations, which have been connected to the extensive hydrothermal activity observed in the area(Ellefmo et al. (2019)).

The AMOR is also a ridge that, compared to the rest of the mid ocean ridge, lie close to the continental shelf. Due to the short distance to the continental plate, the sediments found in the area have often been described as pelagic and/or lithogenic (Bruvoll et al. (2009), Baumberger et al. (2016)), due to the erosion processes wearing on the continental shelf and sediments being deposited off shore.

The samples studied throughout this thesis are collected from two different locations found along the Arctic Mid-Ocean Ridge, Loki's Castle and Mohn's Treasure. Both of the locations are places that are thought to be of interest for finding metallic-sulfides (Pedersen et al. (2010a), Pedersen et al. (2010b) and Ellefmo et al. (2019)), but the geological setting of the two locations are somewhat different. Loki's Castle is classified as an active venting field, and previous studies have analysed samples shown to contain elevated concentrations of iron, copper and zinc, comparable with other hydrothermal fields found on the Atlantic mid-ocean ridge (Snook et al. (2018)). Mohn's Treasure can be described as an inactive vent field in the sense that no hydrothermal activity has been discovered in the area(Lim et al. (2019),Pedersen et al. (2010b) ). However, Pedersen et al. (2010b) discovered traces of sulfides in fragments when collecting sediments by a dredge in 2010 (dredge line is drawn into figure 2.2). The location is thus marked as a "sulfide deposit" in figure 2.1. The two sites are of close proximity of each other and is situated approximately 73°CN, 8°CE in the Norwegian-Greenland sea,

where the Knipovich ridge bends into the Mohn's Ridge (Bruvoll et al., 2009). Relatively to one another, Loki's Castle is situated $30km$ north-east of Mohn's treasure (estimated from Pedersen et al. (2010b)).

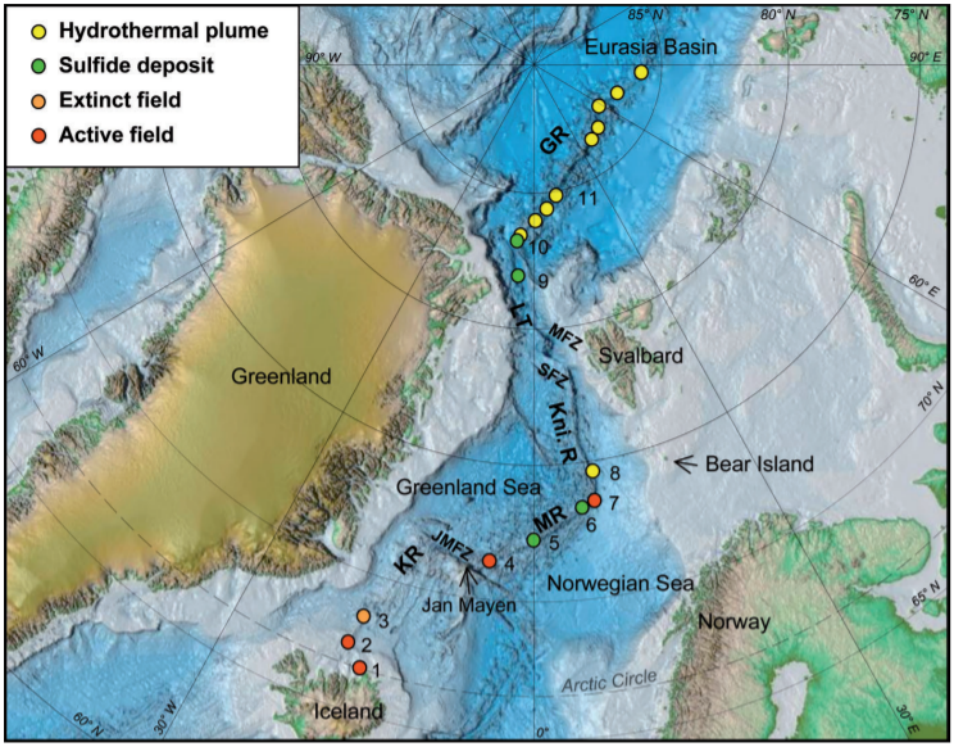


**Figure 2.1:** Figure showing the AMOR with its defined "sub-ridges". From the south: Kolsbein Ridge(KR), Mohns Ridge (MR), Knipovich Ridge (KnR). Loki's castle is point 7, and Mohns Treasure is point 6. Figure from Pedersen et al. (2010b).

## 2.2 The MarMine Project

MarMine is the name of a research project initiated by NTNU which aims to contribute with knowledge and research to the growing deep sea mining industry. It focuses on the technology relevant for the Arctic mid-ocean ridge, and deposits found on the extended Norwegian continental shelf. The project has a number of research and industrial partners, such as Equinor/Statoil, NIVA, NGU and LNS. In 2016, the project launched a research cruise to some of the most promising locations for finding massive sulfide deposits on the AMOR. The purpose was to give more detailed descriptions of those locations, collect samples for geochemical and biological analysis, but also to test relevant exploration technology for such deposits.
The cruise took place on the ship Polar King and different types of remotely operative vehicles (ROVs) was used for sample collection (Ludvigsen et al. (2016)).

### 2.2.1 Sample Collection

In this thesis, 19 of the sediment samples collected by push-core and scoop sampling during the cruise, have been studied.

As the name implies, push core samples are collected by pushing plastic tubes down into the loose upper layer sediments. During the MarMine cruise the arm of the ROV was used to push the cores into the sediment. When the push-core is pushed through the sediment, the water is allowed to escape

the tube through one-way valves at the top. This allows for easy recovery of the samples, when the cores are pulled out and brought to surface.

The Scoop sampling method collected sediment by ”taking a bite” of the upper sediment layer before the samples are brought to surface. The scoops collected the upper 10cm of the sediments and were controlled by the ROV's.

The main practical difference between the two sampling methods is that the push cores allow for the detection of vertical variations in the sediment layering. However, an error discovered during the cruise made it impossible to preserve the layering of the push-cores.

At Loki's Castle two scoop samples were collected, LC-10007 and LC-10008. For practical reasons they were both divided into sub-samples. LC-SS-10007 was divided into three sub-samples which were named named LC-SS-10007-1, -2 and -3, while LC-SS-10008 was divided into two sub-samples named LC-SS-10008-1 and -2. The third sample from Loke is sample LC-SAMLE-10007, which was not collected by scoop. This sample consist of left over material from the tank containing the collected grab samples from the Loki's Castle mound. The material contain small fragments and left over sediments which followed the grab samples.

At Mohn's treasure, both scoop sampling and push-cores were used for collection. In total 1 scoop sample and 7 push cores was collected at Mohn's Treasure. The different sampling methods will not have any implications for the laboratory or analysing methods executed in this study due to the error concerning the push-cores. Some of the Mohn's Treasure samples were also divided into sub-samples, with sub-IDs $>1/2$ or $<1/2$ and $>5$ or $<5$. These ID's illustrate whether the sample is the upper/lower half/5cm of the push cores.

When the sediment samples were brought to the surface they were first drained using a filter and vacuum-pump. The samples was then put in sealed plastic bags, which was first flushed by nitrogen and then vacuum-packed. This was done in order to prevent oxidation. The samples was then put for storage at -20°C in a freezer at the NTNU laboratory. Further details regarding sediment sample storage and collection can be found in the MarMine cruise report, see Ludvigsen et al. (2016).

**Table 2.1:** Table showing the samples studied and their separate sub-samples. LC=Loki's Castle, MT=Mohn's treasure, SS=scoop sampling, PC=push core. Approximate sample collection points are shown in fiugre 2.2 and 2.3

| | Sample Material | |
|---|---|---|
| Location | Sample ID | Sub-ID |
| LC | LC-SS-10007 | 1 |
| LC | LC-SS-10007 | 2 |
| LC | LC-SS-10007 | 3 |
| LC | LC-Samle-10007 | - |
| LC | LC-SS-10008 | 1 |
| LC | LC-SS-10008 | 2 |
| MT | MT-SS-10023 | 1 |
| MT | MT-PC-10028 | 1 |
| MT | MT-PC-10029 | <5 |
| MT | MT-PC-10029 | >5 |
| MT | MT-PC-10031 | <5 |
| MT | MT-PC-10031 | >5 |
| MT | MT-PC-10033 | <1/2 |
| MT | MT-PC-10033 | >1/2 |
| MT | MT-PC-10035 | <1/2 |
| MT | MT-PC-10035 | >1/2 |
| MT | MT-PC-10036 | >1/2 |
| MT | MT-PC-10037 | <1/2 |
| MT | MT-PC-10037 | >1/2 |

### 2.2.2 Mohn's Treasure

Mohn's Treasure was discovered by Pedersen et al. (2010b) in 2002, when a dredge brought up more than 100kg of hydrothermal material from the area. The material contained mostly fine-grained, porous chimney fragments composed of mainly pyrite. These findings was assumed as being evidence of hydrothermal activity in the area. However, the lack of seawater anomalies lead to the conclusion of it being an extinct field. The field is located 2600m below sea level on a ledge situated on the inner western rift wall. The dredge track is shown in figure 2.2, together with approximate samples collecting points for the push cores studied through this thesis. Figure 2.2 shows two maps were the upper show a bathymetry map while the lower show a magnetometry map of the site. Both of the maps include the sample collection points for the push cores.

Magnetometry and bathymetry data were collected during the MarMine cruise by AUVs from Kongsberg maritime. The process of sample collection is described detailed in Lim et al. (2019). Lim et al. (2019) described and interpreted the anomalies found in the magnetometry map. As seen on figure 2.2 the site demonstrate three positive magnetic anomalies which all are concluded on being a result of hydrothermal alteration zones, affecting the magnetic responses of the bed rock. Lim et al. (2019) noted that the northernmost anomaly coincides with parts of the dredge track reported by Pedersen et al. (2010b), and conclude that this anomaly is caused by a buried sulfide deposit at the site. Some of the push cores studied in this thesis were also collected in close proximity to this anomaly and the dredge track. Elevated concentrations of sulfides are expected in these samples.

The two southernmost anomalies are stronger than the northern one and are interpreted by Lim et al. (2019) as being two larger fossil hydrothermal fields, similar to the northernmost one. However this area was not studied in detail during the MarMine cruise. The Norwegian Petroleum Directorate recently proved this field to be a hydrothermal field consisting of hydrothermal material and chimney fragments (personal communication, Kurt Aasly, unpublished results from the Norwegian petroleum directorate). Generally the area surrounding Mohn's Treasure is covered in sediments that represent distal parts of the Bear Island sediment fan (Bruvoll et al. (2009),Lim et al. (2019). The area is also described to contain large fractures and faults, which were uncovered by mass wasting of overlying material (Lim et al. (2019), Pedersen et al. (2010b)).

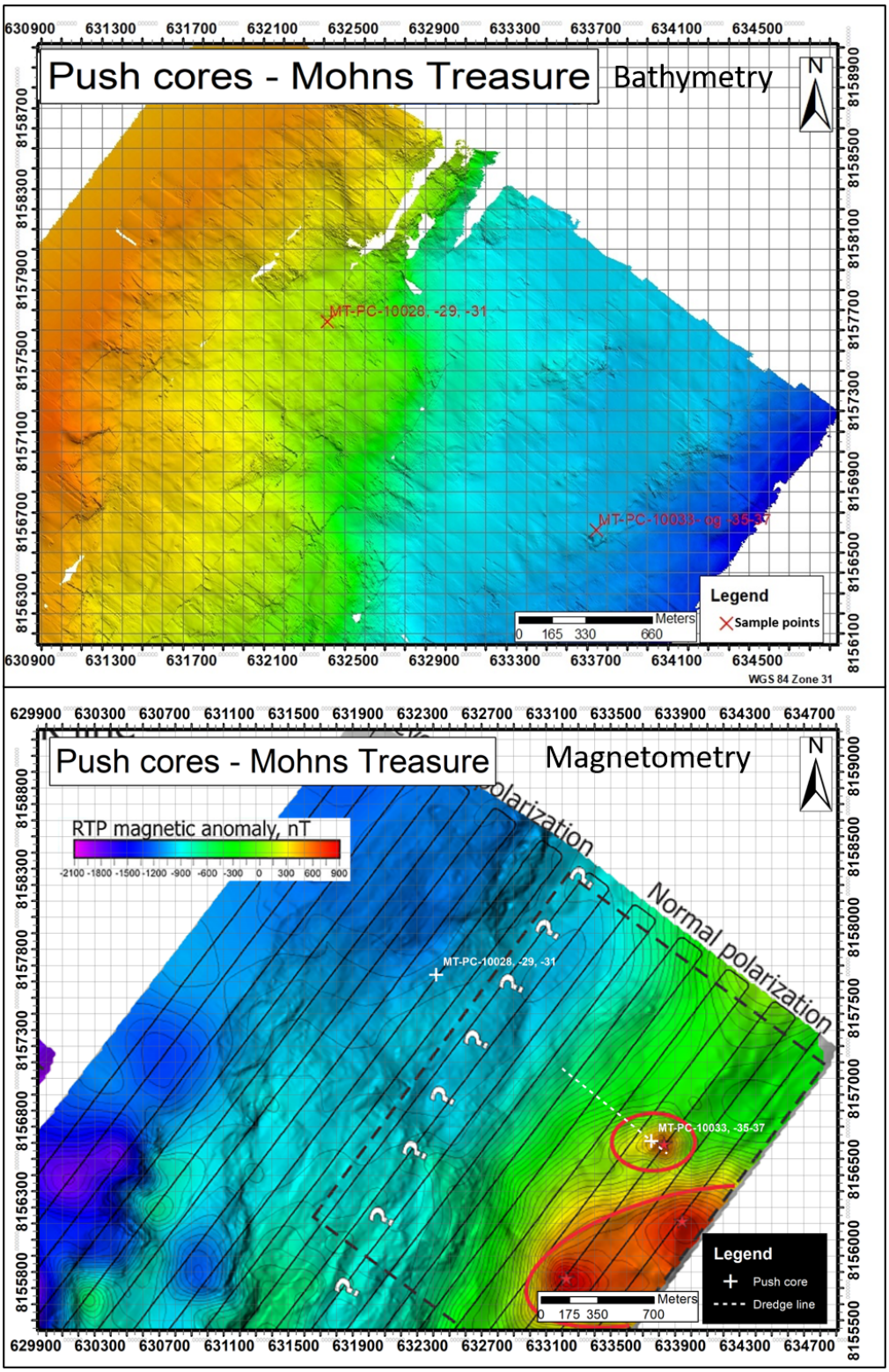


**Figure 2.2:** Figure showing the bathymetry and magnetometry maps based on the data gathered as part of the MarMine cruise. (maps were produced by C. Juliani and S. Ellefmo/NTNU-MarMine as part of marMine research project.)

### 2.2.3 Loki's Castle

In 2008 an active hydrothermal field consisting of 5 active black smoker chimneys was discovered by Pedersen et al. (2010a). The site was named Loki's castle and is located at 79°C30 N, 30°CE, on the summit of an axial volcanic ridge(AVR) at the center of the ridge (Lim et al. (2019)) . The venting occurs at the top of two mounds located approximately 150m apart west and and east from each other. 4 black smokers are situated on the westernmost mound, while 1 black smoker is located on the eastern mound. The two mounds have a height of approximately 20-30m and have a diameter of 150-200m. Combined, the two mounds are comparable in size to the TAG, which is one of the largest active mounds known today. Previous analysis of chimney fragments from Loki, found that valuable elements such as Cu (found in isocubanite and chalcopyrite), Zn (hosted in sphalerite), as well as some Ag and Au, was present in considerable amounts (Snook et al. (2018)).

Baumberger et al. (2016) concluded on Loki's castle being a sediment influenced hydrothermal field after studying the chemical composition of the hydrothermal fluids emitting the site. As mentioned in Herzig and Hannington (1995), hydrothermal fluids may react with the sediment layers as they pass through them. This may lead to leaching of Pb and Ba from feldspar, causing higher Pb and Ba grades in such deposits. However such observations has not yet been observed at Loki's Castle, but might be expected based on the sedimental influence. Another common feature of sediment influenced deposits is that hydrothermal fluids may react with the buried organic matter that is part of the sediment. As fluids react with the organic compounds the conditions become more reducing, leading to pyrrhotite being more common in such settings (Herzig and Hannington (1995)).

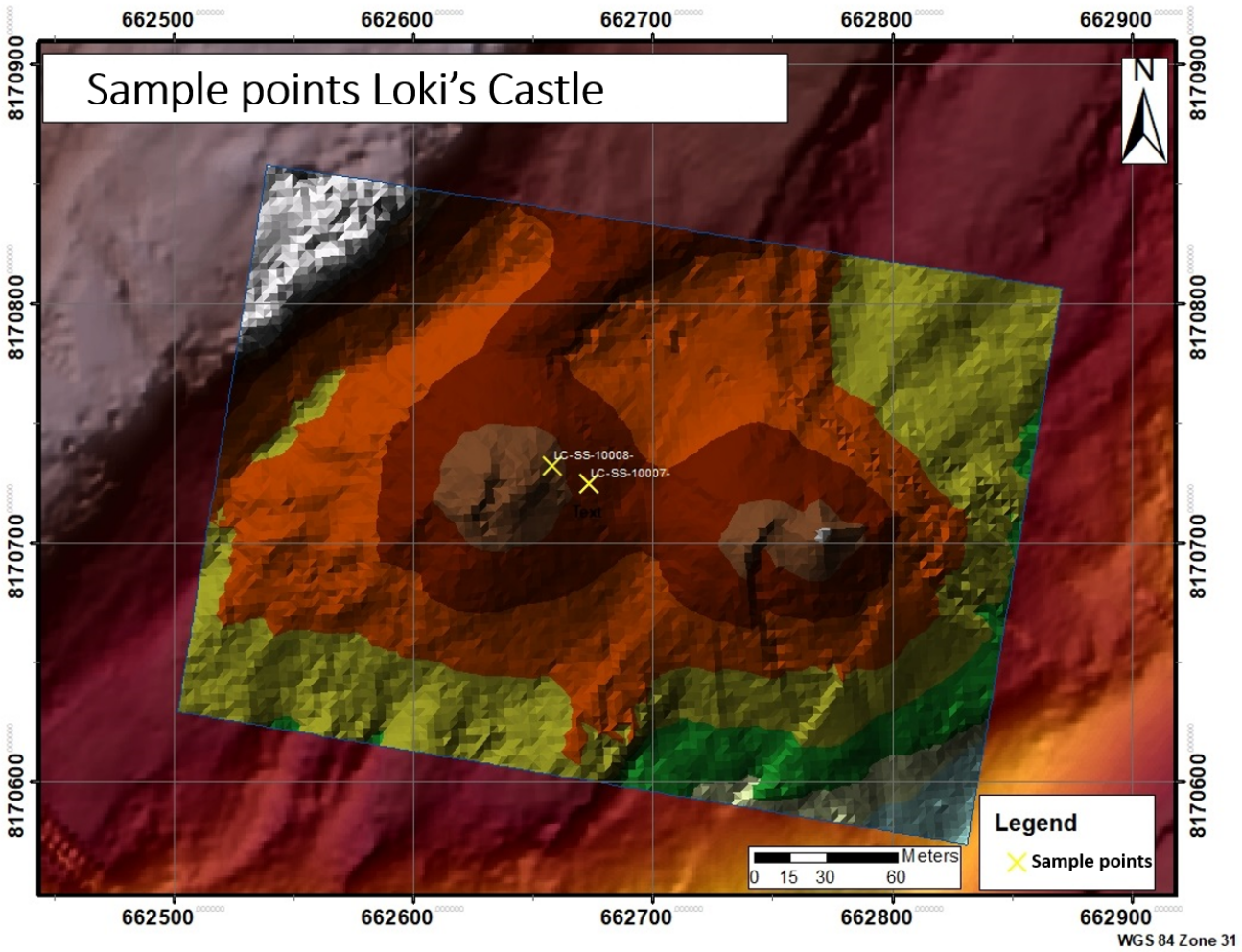


**Figure 2.3:** Figure showing the sample poins from Loki's Castle. The samples were both collected on the western mound. Sample LC-SS-10008 was collected closer to the center of the mound, while LC-SS-10007 was collected towards the flank of the mound.

Chapter 3

# Theory

The following chapter gives a run through of all the theory relevant for the performed laboratory analysis, data processing and discussion. The laboratory methods and equipment used for characterisation are described separately in chapter 4. Much of the background theory related to the geological setting and chemical processes leading to the formation of Seafloor Massive Sulfide (SMS) deposits is already described in the specialization project, and is not as thoroughly described in this thesis. Some of the most relevant parts from Hyllseth (2020) is added in appendix A were some of the principles and definitions are explained.

The samples examined through this thesis are relevant for both studies regarding marine sediments and especially hydogenous and metalliferrous sediments, but also for studying Seafloor Massive sulfide deposits and how such deposits leave a mark on their surroundings. Both theory related to seafloor hydrothermal processes, formation of SMS deposits as well as marine sediment characteristics is relevant for this study and is presented in the following sections.

## 3.1 Seafloor Hydrothermal Processes

As mentioned in the introduction, tectonic spreading settings are important in the formation of deep-sea mineral deposits, e.g bac arc spreading settings, island arcs or mid-ocean ridges . These settings present an environment favourable for seawater infiltration, and associated metasomatism of the crust (Bach et al. (2013)). Even though seawater metasomatism occur all over the ocean floor, the induced faulting and fracturing at spreading centers allow for deeper and more extensive alteration in these zones. The uprising of magma due to the reduced pressure also lead to an elevated geothermal gradient in these settings.

The first alterations occur is in the reaction zone (Figure A.1 found Appendix A illustrate the processes) were only the upper part of the crust is affected. These upper layer processes include oxidation and alkali fixation in the upper basaltic layer. The basaltic crust, including olivine and plagioclase, is altered by *oxidation* to ferric micas and smectites, Fe-rich oxyhydroxides and Mg-rich smectite. In this alteration process alkali metals, such as K, Rb and Cs, B and $H_2O$ is transferred from the sea-water and into the mineral assemblage. Elements such as Si and S is transferred from the minerals and into the fluid (Tivey (2007)). Oxidation is only an important part of the alterations occurring i close proximity of the seafloor. As the fluids penetrate deeper the environment become more reducing, and the oxidation processes stagnate. In such settings different reactions and alteration processes take place. The seawater is already saturated with Mg, and precipitation in the ocean crust as the fluids penetrate deeper, is common. This is observed by the abundance of clay minerals which

suggest the precipitation of Mg-silicate, in form of e.g Mg-rich smectite or chlorite (Alt (1995)). The precipitaiton of these clays start at temperatures above 150°C, which usually occurs at depths of 300-450m (Alt (1995)). The removal of Mg can be shown by the reaction below were Albite-anorthite in basalt reacts with water and Mg, resulting in the formation of Mg-chlorite, and a release of $H^+$-ions resulting in a lower pH in the fluids (Tivey (2007)).

$$\underset{Albite-Anorthite}{4(NaSi)_{0.5}(CaAl)_{0.5}AlSi_2O_8} + 15Mg^{2+} + 24H_2O \Rightarrow \underset{Chlorite}{3Mg_5Al_2Si_3O_{10}(OH)_8} + SiO_2 + 2Na^+ + 2Ca^{2+} + 24H^+$$

Another important process that occur at such depths is the albitization of feldspar, from anorthite to albite, which releases Ca into the fluids. As the temperature increases further the fluids become enriched in alkalis and Boron(B). Other reactions taking place is hydrothermal alteration of the ultramafic host rock including olivine and pyroxene (serpentinization), which produces hydrogen, $H^+$.

The deeper penetration of acidic fluids combined with an elevated geothermal gradient, eventually lead to leaching of metals such as copper(Cu), iron(Fe), zinc(Zn), lead(Pb), silver(Ag) and gold from the host rock (reaction zone, appendix A). As these metal-rich fluids penetrates deeper they will reach the point of phase separation, and the fluids will become extremely buoyant leading to rapid ascendance towards the seafloor. This fluid phase will focus along fluid pathways such as fracture- and fault-zones were they face little resistance and there is high permeability . This results in a focused discharge of the metal-rich fluids where the fluids reach the seabed(discharge zone, appendix A). When the hot fluids meets the cold seawater they are quickly cooled, resulting in the precipitation of metal-sulfides. Here, they manifest as black and white smokers, expelling fluids containing sulfide-particles into large underwater clouds known as hydrothermal plumes.

The black and white smokers are usually located on the top of larger hydrothermal mounds that extend laterally and vertically downwards from the chimneys. They have formed as a result of persistent hydrothermal discharge of fluids and associated precipitation of sulfides. The classic example of a hydrothermal mound is the one found at the TAG deposit in the mid-Atlantic. This mound is also comparable in size with two mounds found at Loki's Castle.

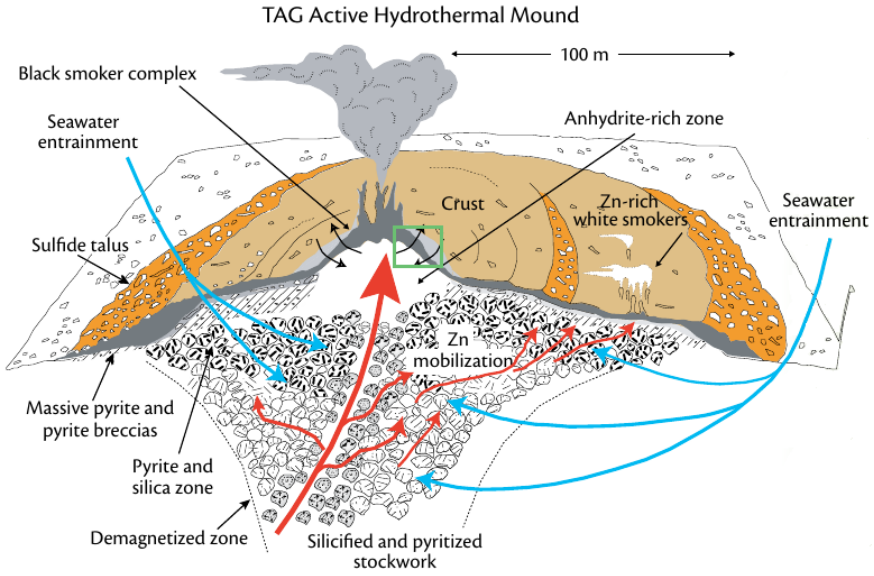


**Figure 3.1:** Figure showing a sketch of the hydrothermal mound found at the TAG deposit. Black smokers are found in the center of the mound, where the fluids with the highest temperatures are discharged. Towards the edge of the mound white smokers may appear as a result of the temperature gradient present within the mound. Figure from Tivey (2007).

The temperature of the fluids exiting these chimneys correlates with their colours. While white smokers usually expell fluids with temperature between 30 to 350°C, black smokers expel fluids with temperatures exceeding 350°C(Trujillo and Thurman (2014)). As a consequence the white smokers usually appear further away from the central discharge zone towards the edge of the mound where the temperature of the fluids is lower (Figure 3.1). There is also a large contrast in the chemical composition of the chimneys and the fluids they emit between black and white smokers. The black smoke get their characteristic colour as a result of elevated concentrations of metal sulfides, such as iron, nickel, copper and zinc. Oppositely, the white smoke emitted from white smokers contain various light-coloured compounds, including anhydrite, baryte($BaSO4$) and amorphous silica(Janecky and Seyfried (1984), Trujillo and Thurman (2014)). White smokers do not have the same concentrations of Cu-sulfides like black smokers, due to these phases being precipitated at higher temperatures (Janecky and Seyfried (1984)). Sphalerite (Zn-sulfide) is however common in the mound beneath the white smokers. Additionally to the zoning on a large scale through the mound, there is commonly a zonation pattern within the chimney-structures as well. The zonation pattern largely depend on the temperature gradient and degree of mixing between the seawater and hydrothermal fluid (Janecky and Seyfried (1984), Dekov et al. (2008)). In active chimneys that have increasing temperatures towards the center of the structure, chalcopyrite is most commonly precipitated in the inner walls along with isocubanite. Pyrite is present all across the chimney wall and is the most common Fe-sulfide in these structures. (German and Von Damm (2006), Janecky and Seyfried (1984)). Pyrrhotite can however replace pyrite and is more common in the black smoke emitting the chimneys.

Other common composites that precipitate when the hot hydrothermal fluids mix with the cold seawater is anhydrite, smectites and Mg-phyllosilicates such as talc, keolite-smectites and chlorite (Janecky and Seyfried (1984), Dekov et al. (2008)). Mg-phyllosilicates form as a result cold Mg-rich seawater reacting with hot silica-rich hydrothermal fluids (Dekov et al. (2008)). Higher talc respective to other Mg-phyllosilicates indicate higher silica-activity.

Anhydrite is the first of these phases that precipitate, and is often present in the edges of chimney structures, as well as the edges of mounds. Chlorite-smectite and chlorite form at temperature be-

tween 150-200°C by alteration of sediment matrix. These compounds usually form as a result of low temperature diffuse venting through hydrothermal conduits within sediments at the edge of the hydrothermal field and mound. If the hydrothermal source is sediment covered, then these compounds might be intercalated with the sediment cover (Buatier et al. (1995).
Talc is precipitated at temperatures around 280-330°C, and is a high-termperature phase. The precipitation of talc leads to the generation of protons leading to a reduced pH, which might initiate alteration of some of the primary sulfides. E.g already precipitated pyrrhotite may be converted into FeOOH or jarosite. If there is high enough concentrations of reactive Al then kerolite-smectite might precipitate, rather than talc. Dekov et al. (2008) suggest that talc likely form in the upper layer of sediments where Mg-rich seawater is easily accessible, while further down in the sediment layers and within the mound Al-rich layers of kerolite-smectites may form due to a lower Mg/Al-ratio. Talc may also form an Fe-rich variety due to Fe-rich hydrothermal fluids (Dekov et al. (2008)).

## 3.2 Marine sediments

The worlds ocean floor is covered with marine sediment layers of varying thickness with the thinnest layers found in the deepest oceans and on top of fresh oceanic crust (Mid-Ocean Ridges). Thick layers of sediment accumulate in areas close the continental shelf near big rivers, or glaciers(Trujillo and Thurman (2014)). Marine sediments are usually classified after their source of origin, and generally four types of marine sediments are accepted (Boström et al. (1973b), Trujillo and Thurman (2014)):

1. Lithogenous
2. Biogenous
3. Hydrogenous
4. Cosmogenous

Most of the lithogenic material is of terrestrial origin and created through land based erosion and weathering processes, such as rivers, glaciers or wind which is then dispersed/scattered into the oceans where they settle/are deposited (Trujillo and Thurman (2014)). The composition of these sediments is thus similar to the rock in which they originated from, and reflect the composition of the continental crust (rich in quartz, clay and rock fragments).

Settlement and deposition of these terrigenous sediments are most frequent closer to the continental crust and accumulate rapidly on the continental shelf as well as the continental slope and rise(Gurvich (2006)). The thickness of the lithogenous sediments gradually decrease further away from the continental shelf and as a consequence this type of sediment is not as common in the deep-oceans. However if deep-ocean turbidity currents are present, they can be carried beyond the margins of the continental shelf (Trujillo and Thurman (2014). In areas where glaciers have eroded the continental shelf (e.g during the end of last ice age 18,000 years ago) the sediments have accumulated rapidly (Trujillo and Thurman (2014)). As a consequence large parts of the upper northern hemisphere is covered in continental lithogenous sediment both on the continental shelf as well as in the deeper parts of the ocean(Trujillo and Thurman (2014), Bruvoll et al. (2009)).

Biogenous sediment is sediment that is produced by living organisms which leave behind calcarous or silicious material, which is precipitated in the water or on the seabed when the organism die(Trujillo and Thurman (2014)). This type of sediment is generally either siliceous or calcareous, based on what type of organism produce the sediment. The productivity of biogenous oozes depend

on whether the conditions are favourable for organic life. Productivity is lowest in centrals areas of the oceans and highest at the equator and in zones of coastal up-welling. Siliceous biogenous sediment consist of mostly silica and/or opal (silica $\cdot$ $nH_2O$) and is easily dissolved in seawater. Silicious ooze is thus dependent on high biologic activity in order to form accumulations. Carbonate ooze is also dissolved in seawater, but only in areas that are not saturated in calcium usually at great depths (below 4000m)(Trujillo and Thurman (2014)). Silicious ooze is in general more common in the pacific ocean, and the floor of the indian ocean(Rafferty (2009)). Carbonate ooze is more dominate in the seafloors of the Atlantic ocean (Trujillo and Thurman (2014), Metz et al. (1988)).

Biogenous and lithogenous sediments make up approximately 85% of the marine sediments present at the seafloor, while hydrothermal and cosmogenous sediment are more rare (Trujillo and Thurman (2014)).

Hydrogenous sediments are sediments that have formed by precipitation of particles as a result of chemical reactions taking places in the water (Trujillo and Thurman (2014), Gurvich (2006)). This includes several different types of minerals, several of them being classified as possible marine mineral resources. Manganese nodules is an examples of metal-rich hydrogenous sediment, which primarily consist of manganese- and iron-oxide with accessory metals such as copper, nickel and cobalt. Other examples of such sediments are evaporites and oolites[1]. Precipitation from water usually occcur due to a change in the physical conditions such as changing pressure or temperature.
Cosmogenous sediments are created as meteors or other kinds of extraterrestrial matter enter the earths atmosphere(Trujillo and Thurman (2014)). These sediments are usually located in close proximity of existing meteor craters and not relevant for the sediments studied through this thesis.
These four types of sediment does not only occur separately but usually there is a mix of two or more of the sediment types (Trujillo and Thurman (2014)).

### 3.2.1 Metalliferrous sediments

Another kind of marine sediments are *metalliferrous sediments*, which are not defined by their source of origin but by their chemical composition. Metalliferous sediments are described as being anomalously rich in iron and being depleted in aluminium (Gurvich (2006)). These sediments are present in all of the worlds ocean floors today, but are most frequent in areas related to spreading ridges and oceanic subduction zones. After the discovery of submarine hydrothermal systems it became apparent that these sediments was formed as a result of discharge of iron rich hydrothermal material mixed with background sediments. In that sense, metalliferrous sediments can, by the definition above, be classified as a type of hydrogenous sediment.

There are several criteria commonly used in order to define sediments as metalliferous, but usually there are criteria based on the ratio between iron and aluminium. Boström et al. (1973b) defined metaliferrous sediments as having Al/(Al+Fe+Mn) $<$ 0.3, Fe/(Al+Fe+Mn)$>$ 0.5 and (Fe+Mn)/Al $>$25. Another scheme define metalliferrous sediments as having a (Fe+Mn)/Ti $>$ 25. Specifically looking at the concentration of Fe is also a possible way of defining metalliferrous sediments, and Lisitizin et al. (1976) defined metalliferrous sediments as containing more than 10% Fe in their abiogenic part and being depleted in Al and Ti. If the metalliferrous sediments contain more than 30% Fe they can also be referred to as *ore sediments* (Gurvich (2006)).

Metalliferous sediments are usually found in relation to mid-ocean rift systems and back arc spreading centers, and are created by the submarine discharge of hydrothermal fluids that have been circulat-

[1]Sand-sized particles consisting of calcite. This type of hydrogenous sediment precipitate from the warm waters in tropical regions (Trujillo and Thurman (2014))

ing within the spreading ridge (German and Von Damm (2006), Gurvich (2006)). High-temperature hydrothermal fluids are rich in metallic sulfides, and the metals iron, zinc, copper and nickel, and are believed to be the main source of metalliferous sediments in the oceans(Gurvich (2006)). The hydrothermal fluids manifest themselves as large buoyant clouds, known as plumes, exiting tall chimney structures on the seafloor. The buoyant plumes rises upwards until they reach neutral buoyancy level (NBL) when the density of the plume is equal to the density of the surrounding water(Gurvich (2006),German and Von Damm (2006)). The temperature of the plume as it exits the chimney is what decides the height of the plume. Above a typical high-temperature vent the height of the plume usually lie between 150-400m (Gurvich (2006)). Here the plume stagnate and spread laterally by gravity currents. Other ambient seawater currents may also influence the spreading direction of the plume, and the presence of large, stable underwater-currents may carry the plume material great distances before the material settles(Dissanayake et al. (2014), Gurvich (2006)). As a consequence, the hydrothermal material may be spread out over large areas. The tectonic environment in which the hydrothermal source is located is also a controlling factor for the spreading pattern of the hydrothermal plumes. Slow spreading rifts usually have a deeper rift valley which constrain the hydrothermal plume. In such settings the plume tend to move along the rift valley and may also settle on shelves along the rift wall. Plumes forming in a fast spreading setting, are not constrained by the rift walls and can spread out latterly in all directions, hundreds of kilometers away from their hydrothermal source (Gurvich (2006)).

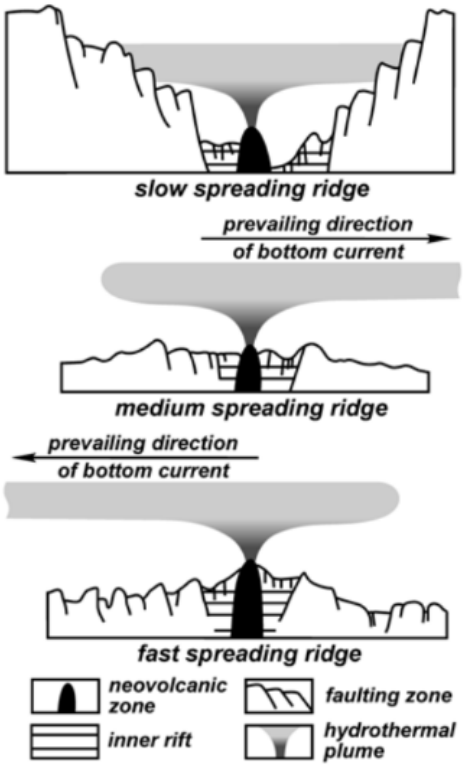


**Figure 3.2:** Illustration showing the plume changing from buoyant to nonbuoyant as it is cooled and mixes with the cold seawater. Particle settle as the momentum of the plume ceases and the plume spread out latterly. The sketch also show how different morphological settings as well as ambient underwater current may affect the spreading direction. Figure from German and Von Damm (2006)

### 3.2.2 Hydrothermal component

Even though marine sediments are characterised after the 4 types presented above, most places a combination of two or more of the types is more likely. One of the challenges will then be how to differentiate the different types of sediment from the others in one sample. Metz et al. (1988) faced a problem related to this when analysing gravity cores consisting of sediments from the TAG hydrothermal field. They were interested in finding out how much of the gravity core that were of hydrothermal origin. The method utilizes the amount of biogenic and lithogenic material present in the sample, in order to estimate the hydrothermal fraction. Biogenic sediments are defined as sediments containing mostly remains of living organisms, such as calcite or opaline silica. Lithogenicc material is defined as material that is derived from the degradation of pre-existing rock that has been transported to the seabed.

The biogenic component is assumed to be equal to the amount of carbonate in the samples, which was studied through XRD. The lithogenic component has a correlation with the aluminium content of the samples. For North-Atlantic sediments the study assumes that the amount of de-trial clay is equal to 10 times the Al-concentration, which is argued to be typical for sediments in this area. The hydrothermal fraction can then be calculated by substracting the percentage of biogenic and lithogenic material from 100% which gives a simple estimate for the concentration of hydrogenous material.

$$Hydrothermal\ component = 100 - (\%\ biogenic\ matter + \%\ lithogenic\ matter) \tag{3.1}$$

This equation assumes that all of the biogenic material consists of calcarous ooze. As described above, this might not be accurate as some of the biogenous material might also be siliceous. However calcarous oozes are the most common biogenic sediment type in the Atlantic ocean (Metz et al. (1988), Trujillo and Thurman (2014)) and silicious ooze is assumed to be near or equal to zero.

After calculating the hydrothermal component of the samples, Metz et al. (1988) plotted it against the Fe-concentrations. If the assumptions made are correct, then the hydrothermal component should make a linear correlation when plotted against Fe. Their calculations are shown in figure 3.3, which shows a strong positive and linear correlation pattern.

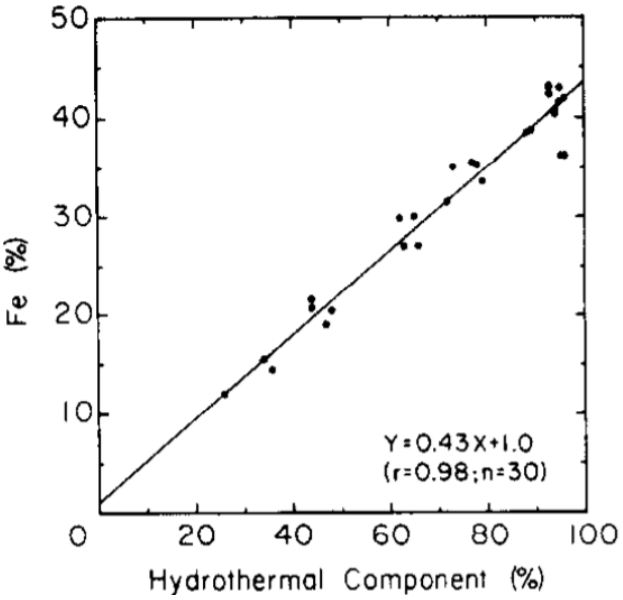


**Figure 3.3:** The calculated hydrothermal component versus Fe concentrations from gravity cores taken from the TAG hydrothermal deposit. There is a clear linear trend between the calculated hydrothermal component and Fe content, which validates the method(Metz et al. (1988)

## 3.3 Characterisation of Massive Sulfide Deposits

Seafloor Massive Sulfide (SMS) deposits is often looked upon as a modern analogue to Volcanogenic Massive sulfide (VMS) deposits. Hence, many of the methods used to characterize VMS deposits is also applicable when characterizing SMS deposits.
VMS deposits form in a range of submarine volcanic arc settings, e.g mid-ocean ridges, back-arc basins, fore-arcs and island arcs etc (Barrie and Hannington (1997)). There are several methods used to classify VMS deposits. Some are based on the tectonic setting, while others look more specifically at the base metal contents.

One of the most widely used methods today is to look at the host rock lithology associated with the deposit(e.g Piercey (2011), Barrie and Hannington (1997), Franklin et al. (2005), Galley et al. (2007)) . The fact that most of the metals mobilised during VMS formation are leached from the host rock, makes this classification scheme convenient in also predicting the metals present in different formations. The system classifies the deposits into 5 main categories from primitive to evolved composition (Barrie and Hannington (1997)):

1. *Mafic*: Consist of predominantely mafic host rock ($> 75\%$) and $< 1\%$ felsic volcanic rock.
2. *Bimodal-mafic*: Defined as having $> 50\%$ mafic rock and $> 3\%$ felsic rock.
3. *Mafic-siliciclastic*: Sometimes referred to as the *pelite*[2]*-mafic* type. A type that consist of equal concentrations of mafic rock and siliciclastic rock type.
4. *Bimodal-felsic*: Defined as consisting of more $> 50\%$ mafic and $< 15\%$ siliciclastic host rock.
5. *Bimodal-siliciclastic*: This type contains approximately equal proportions of siliciclastic and volcanic (felsic or mafic) host rock. Felsic rock is more abundant than mafic as the volcanic constituent, leading to the type also being known as *Felsic siliciclastic.*

[2]Pelitic rocks are derived from mudstone (shale) protoliths and are rich in potassium (K), aluminum (Al), silicon (Si), iron (Fe), magnesium (Mg), and water (H2O).

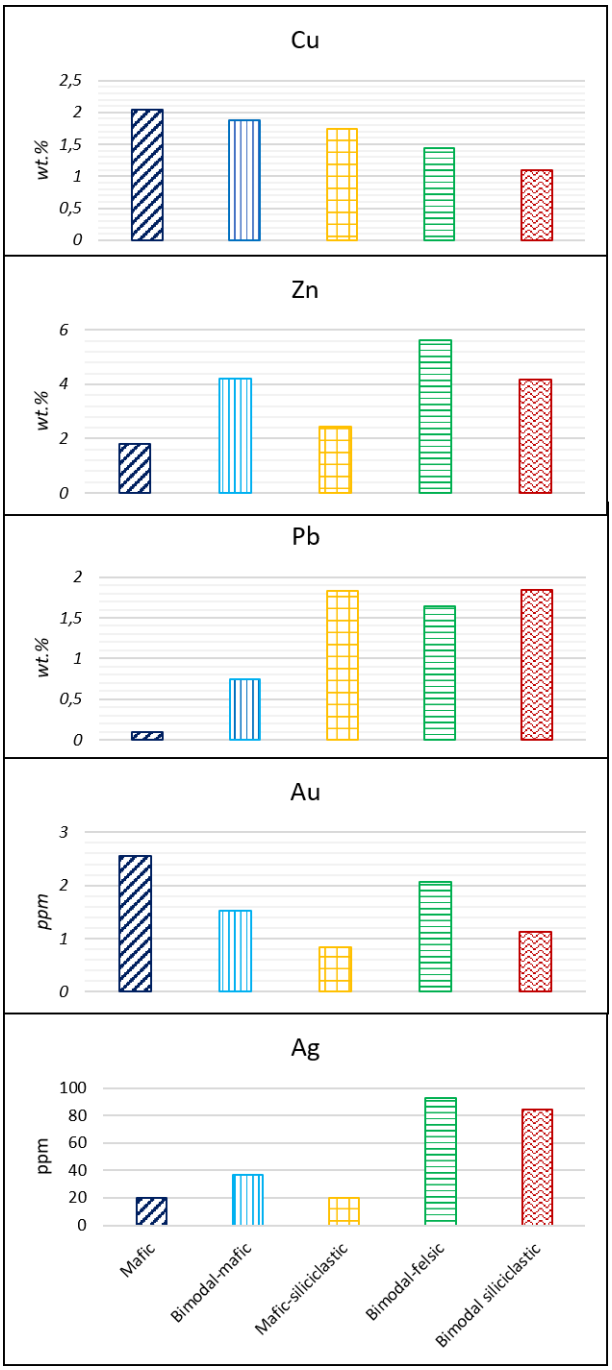


**Figure 3.4:** Figure showing the average base metals concentrations/grades in wt.% for the different deposit types. Numbers are calculated from in total 879 deposits and the figure is based on Barrie and Hannington (1997)

The advantages with this classification system is that each type is found to be directly correlated to different tectonic settings and regimes (Galley et al. (2007)). Mafic-dominated groups(1,2 and 3) are less evolved and reflect the tectonic settings found at ocean spreading ridges and oceanic arcs. The more evolved felsic dominated groups are most common in continental arc regimes and arc-continent margins (Galley et al. (2007)).

The base metal contents also show correlation with the VMS types and Barrie and Hannington (1997) has, by studying in total 879 deposits, found a pattern regarding the respective base metal contents for each type. Some of the results are found in table 3.1, figure 3.4.

Figure 3.4 shows the plotted data from table 3.1. Here the trends of base metal content become clearer. The mafic hosted deposits generally show high Cu-grades, with gradually decreasing grades towards the more evolved settings. Contrarily, Pb show the lowest abundances in mafic settings and higher concentrations towards the more mature compositions. Especially the settings with a siliciclsatic host rock show high grades of Pb. As discussed in (Piercey (2011) lead is an element often leached from feldspar, making such settings favourable for lead being introduced to the hydrtohermal system. Zinc shows varying abundances with the lowest grade deposits found in mafic and siliciclastic lithologies.

The highest grades of gold is found in mafic hosted deposits as well as bimodal felsic. Silver shows highest abundances in bimodal felsic and bimodal siliciclastic settings which is the most evolved host rock lithologies.

**Table 3.1:** Average sizes and ore grades for the different types of VMS deposits. Data from Barrie and Hannington (1997))

| Type | Average size (million tonnes) | Average Cu grade in wt. % | Average Pb grade in wt.% | Average Zn grade in wt.% | Average Au grade in ppm | Average Ag grade in ppm |
|---|---|---|---|---|---|---|
| Mafic | 2.8 | 2.04 | 0.10 | 1.82 | 2.56 | 20.0 |
| Bimodal-mafic | 5.1 | 1.88 | 1.75 | 4.22 | 1.52 | 36.5 |
| Mafic-siliciclastic | 11.0 | 1.74 | 1.83 | 2.43 | 0.84 | 19.8 |
| Bimodal-felsic | 5.2 | 1.44 | 1.64 | 5.63 | 2.06 | 92.8 |
| Bimodal siliciclastic | 23.7 | 1,10 | 1.84 | 4.16 | 1.13 | 84.4 |

### 3.3.1 Base metal content

Classification of VMS by base metal contents is also a widely used method to characterise these deposits. As shown in the section above, the base metal grades vary between the different formation settings. E.g if a deposit show enrichment in Cu and is lead-poor, this indicates that a mafic formation setting is more likely than a bimodal siliciclastic one. One of the schemes used to clarify these trends is by plotting the Cu-, Pb-, and Zn-grades in a ternary phase diagram (Galley et al. (2007), Barrie and Hannington (1997), Large (1992), Lydon (1984)). This classification scheme is only based on the metal grades and is thus an easier applied method, because it requires less interpretation of the tectonic environment.

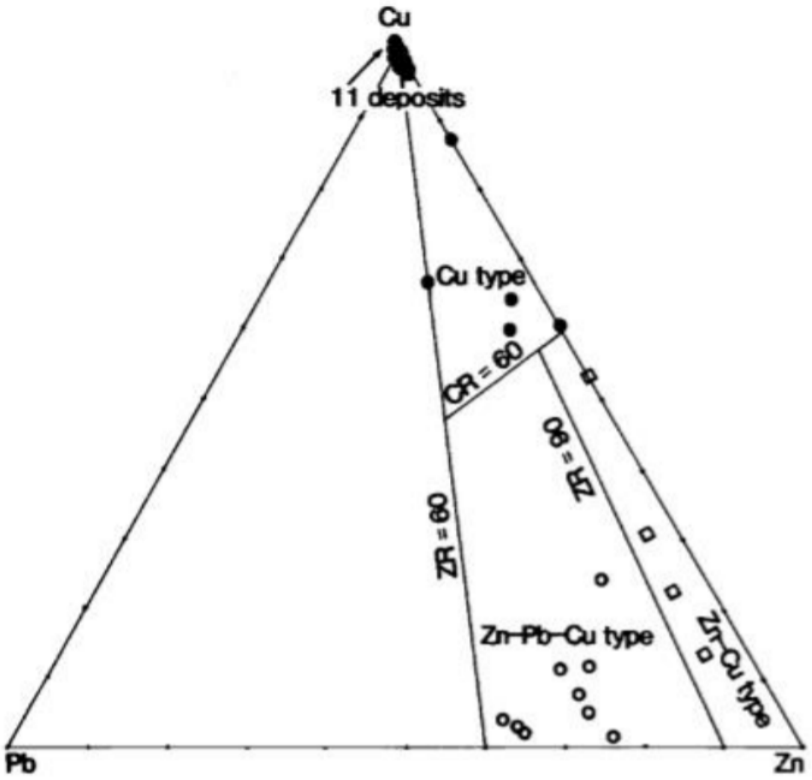


**Figure 3.5:** Figure from Large (1992) showing the base metal ratios from different deposits.

The scheme is also easier to apply because it requires less data from the deposit and from the host rock lithology surrounding the deposit. The classification scheme was first designed by Franklin et al. 1990, but later modified by Large (1992) and Franklin et al. (2005). The shceme divides the deposits into three groups according to the copper- and zinc- ratio defined below (CR and ZR)(Large (1992)).:
were:

CR$= 100 * \frac{Cu}{Cu+Zn}$
ZR$= 100 * \frac{Zn}{Zn+Pb}$

The groups are defined as follows:

1. Cu-deposit: CR>60 and ZR>60)
2. Zn-Cu deposit: CR$< 60$ and ZR>90
3. Zn-Pb-Cu deposit: CR<60 and ZR=[60-90]

These criteria are drawn into figure 3.5 and makes it evident which category a deposit belong to when plotted. There is an additional category which some authors add to the scheme, called Pb-deposits. This category is found to the left of the line ZR=60.

Another method commonly used when studying VMS deposits is to compare the relative base metal content (Cu+Pb+Zn) with the precious metals gold and silver. This scheme was developed in order to separate Au-rich deposits from the ”normal” Cu-Pb-Zn deposits (Galley et al. (2007)), and is illustrated in figure 3.6. Here the combined concentration of the base metals Cu, Pb and Zn is plotted along with Au and Ag in ppm. To better clarify the association between the base metals and the precious metals, the base metal concentrations can also be plotted against the gold and silver grades separately as shown in figure 3.7 (Large (1992)). Here the base metal grade of 30 major Australian VMS deposits is plotted against their respective gold and silver contents. Large (1992) found there to be a correlation between the deposits types illustrated in figure 3.5, and the precious metal grades. As seen in figure 3.7 a) and b) there is a positive correlation between base metal content and precious metal grades. However the trend is clearer for silver than for gold. Figure 3.7 also demonstrate how the different deposit types shown in figure 3.5 correlates with precious metal content for these deposits and clarifies the correlations from figure 3.4

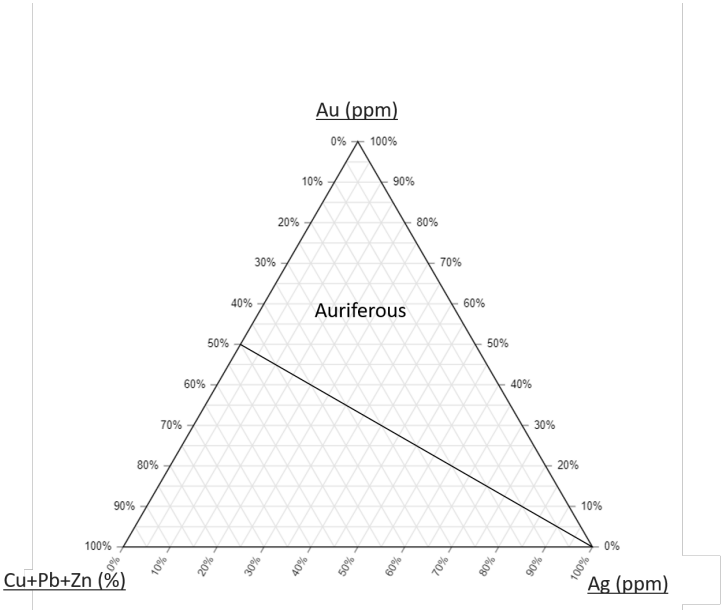


**Figure 3.6:** The ternary plot distinguishing between gold-rich (auriferous) and normal sulfide deposits. Drawn from Galley et al. (2007)

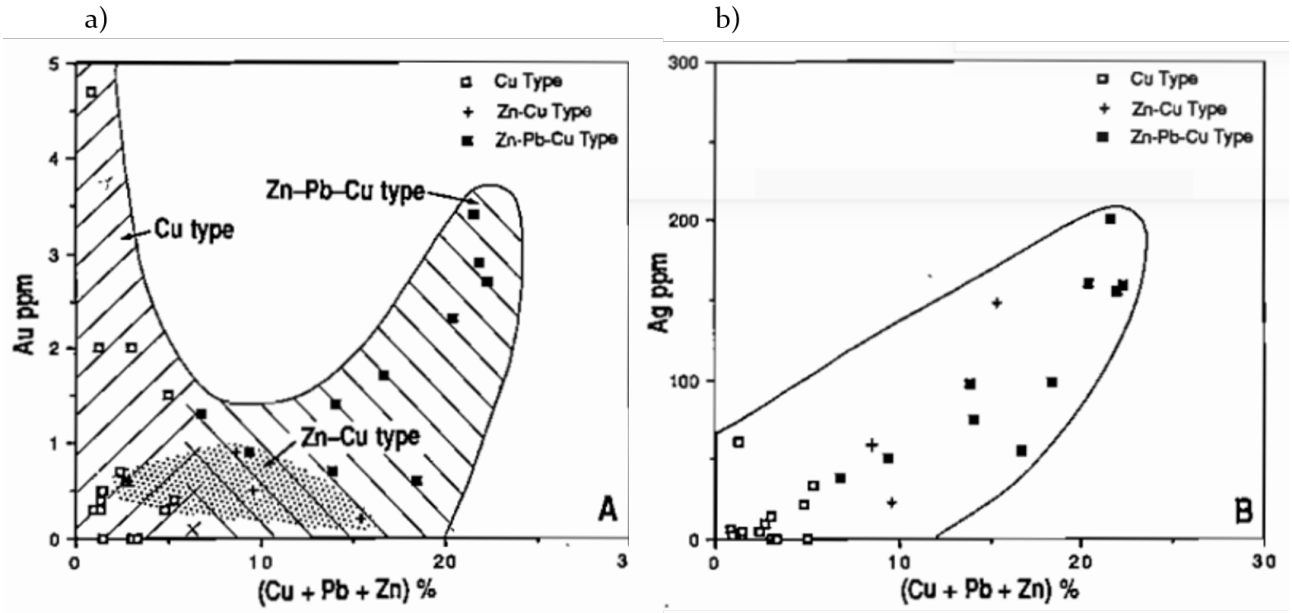


**Figure 3.7:** Figure showing how the base metal concentration correlates with gold and silver grades. a)Mean Base metal content vs mean gold concentration from 30 major Australian VMS deposits.b) Mean base metal content vs. mean silver concentrations from 30 major Australian VMS deposits. (Figure and data is from Large (1992))

To show the relationship between the two schemes (host rock lithology and base metal content) the base metal grades from figure 3.4 is plotted similarly to figure 3.7. Figure 3.8 show the same trends as figure 3.7 making a connection between the base metal grades and the host rock lithology of a deposit.

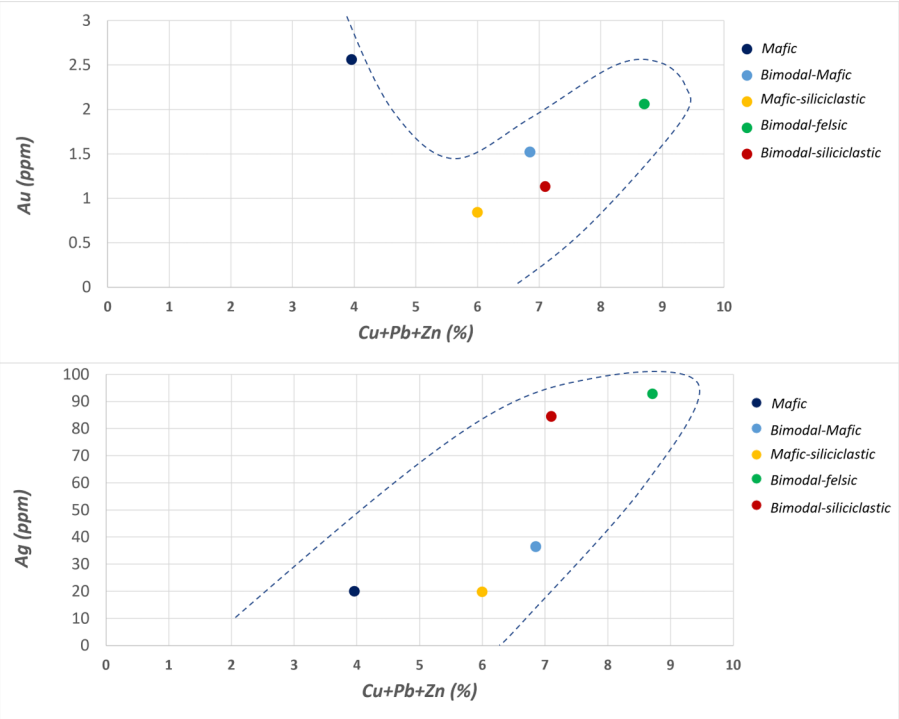


**Figure 3.8:** Figure comparing the base metal trends from figure 3.4 with the with the respective gold and silver trends. The typical base metal grades related to host rock lithology (from figure 3.4) correlates with their respective precious metal content.The plots show that same trend as shown in figure 3.7 is also present in the characterisation scheme that is based on host rock lithology.

Figure 3.9 show how the average base metal grades plot according to the scheme presented in figure 3.5.

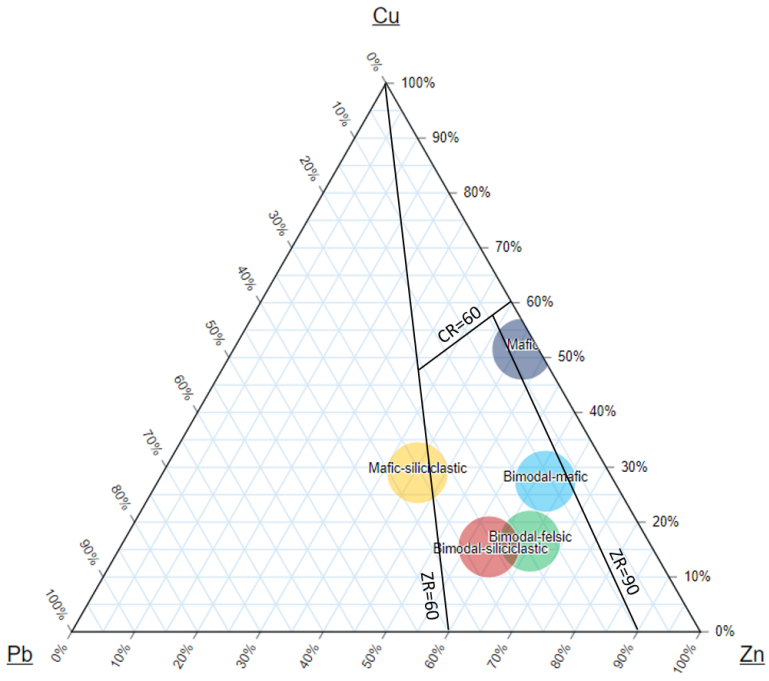


**Figure 3.9:** Figure showing the average base metal ratios from the different lithology types.

The schemes presented in this section can be used to easier characterise the deposits studied through this thesis. By combining the base metal grades with the characterisation shceme based on host rock lithlogy, the small sample collection available for this study will give more detailed information about the possible precious metals (indications of gold and silver grades) and also valuable information about the host rock lithology (e.g sedimental influence). Using schemes that are based on base metal ratios rather than base metal grades might be more suitable for these samples, as the samples might be diluted by other types of sediment.

### 3.3.2 Rare Earth Elements

The composition of rare earth elements (REE) in igneous rocks plays an important role when interpreting the petrogenesis of a rock (Winter (2009)). These elements are a special group of trace elements that show equal physical and chemical properties making them behave consistent respectively to each other. The elements have equal oxidation states (3+) but their ionic radius vary according to their atomic number, hence they have varying compatibility (respective to liquid phase) (Winter (2009)). Heavy REE's have a smaller ionic radius due to an effect known as *lanthanide contraction*[3], which causes the heavier atoms to contract leading to a smaller atomic radius. The smaller the ionic radius, the more compatible are the elements, i.e the heavier REE's are more compatible than the lighter ones(Winter (2009)).
One of the most common ways to visualize the REE trends in a rock sample, is by plotting the REE series with gradually increasing compatibility on the horizontal axis and respective concentrations on the vertical axis. Usually, the concentrations are normalized to chondritic or primitive mantle compositions, to better clarify/illustrate the trends within the samples (e.g figure 3.11). This makes the plot unitless and makes it easily to compare with other samples.

When the normalized REE values are plotted, different patterns in the plot will appear. The pattern created largely depend on the composition of the source rock as well as degree of partial melting and/or fractionation history. In an evolved setting the melt will contain higher concentrations of the more incompatible elements as they want to remain in the liquid phase for as long as possible. Vica verca, a rock that have crystallized from a less evolved source, will be depleted in the incompatible elements.

Another characteristic feature of REE-diagram is the presence of an Eu-anomaly. This anomaly appear either as an abnormal enrichment or depletion of Eu compared to the other elements, i.e the anomaly may occur either as positive or negative. The anomaly of Eu form as a result of different valence states of the element. Under reducing conditions, were the oxygen fugacity ($fO_2$) is low, Eu may have a 2+ valence state. In this state Eu can substitute for Ca into plagioclase, making plagioclase enriched in divalent Eu. (Winter (2009)). If a melt crystallizes during such conditions it is likely that the plagioclase will be rich in Eu, creating a positive Eu-anomaly. A negative anomaly can occur if the degree of partial melting is low and plagioclase, and Eu, is retained in the solid state.

[3]Lanthanide contraction: the elements in the lanthanide series shows a greater decrease in atomic radii than what is expected according to their atomic weight.

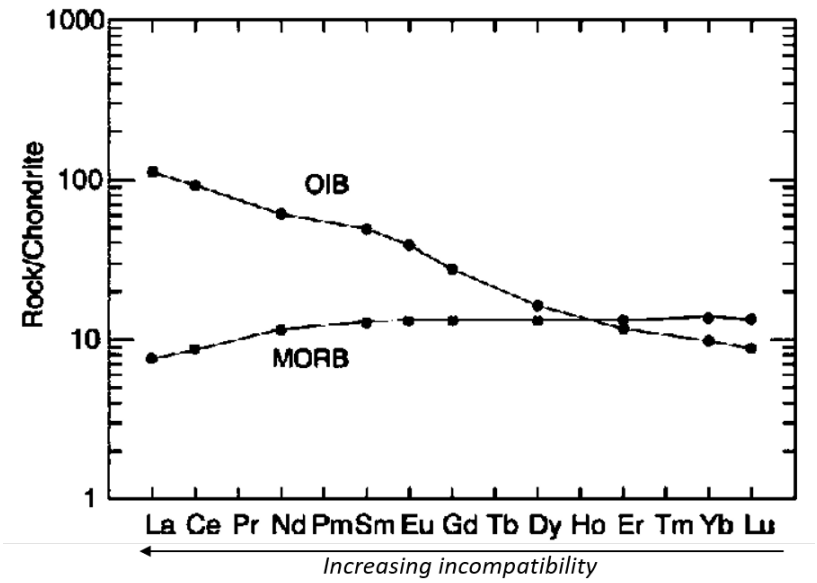


**Figure 3.10:** Typical REE patterns for Osean Icland basalt and Mid Ocean Ridge Basalt. Increasing *incompatibility* towards the left. Figure from Winter (2009)

REE patterns gathered from SMS deposits generally show depletion of REE's, with values between 0.1 and 10 for most elements (Yıldırım et al. (2016), Krasnov et al. (1994)), which likely reflects the composition of their host rock. Positive Europium anomalies may also be present from such sites (ie. Krasnov et al. (1994), Snook et al. (2018). This is generally explained by the leaching of Eu-rich plagioclase, by the hydrothermal fluids circulating through the rock (albitisation).

When Snook et al. (2018) characterised chimney fragments from Loki's castle, REE data was gathered by ICP-MS. Their results are shown in figure 3.11. As seen on the figure, the sample material was divided into 4 groups based on where they were collected and what they consisted of. Mudstone and basalt was collected from the flanks of Loki's Castle and was analysed to give a better understanding of the regional geology. The vent material is a collective name for all of the chimney material collected by grab sampling.

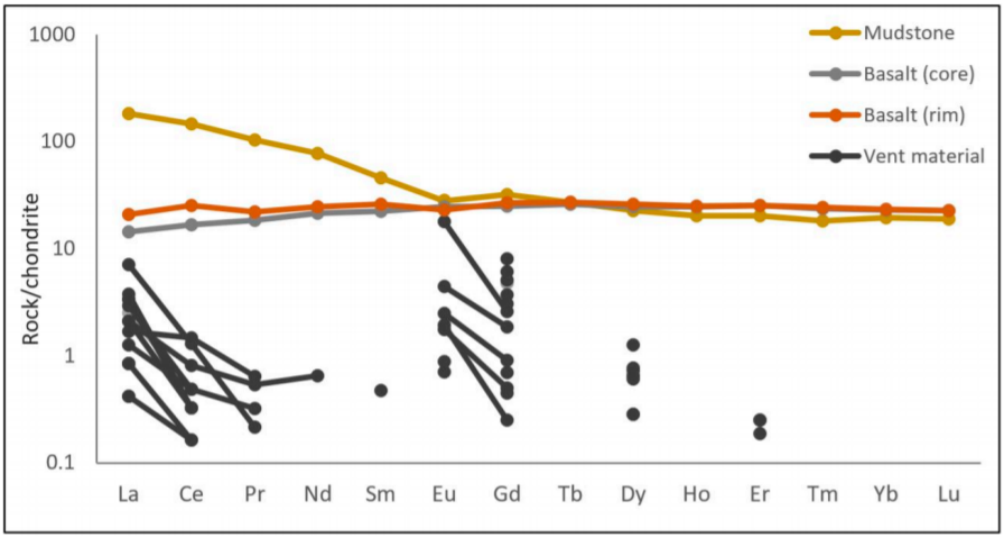


**Figure 3.11:** Figure from Snook et al. (2018) showing chondrite normalised values from the Loki's castle area. The elements without a datapoint was measured below the detection limit.

The vent material collected from Loki's Castle showed clear positive Eu-anomalies which is expected from such sites (Krasnov et al. (1994)).

Dekov et al. (2008) found weak negative europium anomalies from sediment samples collected in close proximity to hydrothermal fields. These observations are explained by the fact that previous precipitations have worked as sinks for Eu, causing a negative Eu-anomaly in the remaining fluids which then precipitate in distal locations of the main discharge zone. These observations makes it evident that REE-patterns will vary within a single hydrothermal field, depending on where the samples are taken from (Dekov et al. (2008)).

Chapter 4

# Materials and Methods

The following chapter will give a description of the laboratory methods used through this project. The sample collection procedure was done prior to this study and is described in chapter 2.

## 4.1 Materials

The material studied in this thesis was all collected as part of the MarMine project, an the cruise/expedition that took place in 2016 ( described in chapter 2). Sediment ”scoop samples” and push-cores was collected by ROV’s from Mohn’s treasure and Loki’s Castle. Sediments from Loki’s Castle was collected by an ROV grab, which initially was supposed to collect fragments from the mound. When the ROVs emerged, the grabs also contained considerable amounts of sediment that had covered the mound. These sediments was kept for future analyses (Ludvigsen et al. (2016)).

When the samples were brought to surface, they were filtered, nitrogen-flushed and vacuum-packed. They were stored at -20°Cuntil they were analysed through the work described in this thesis. The material consist of in total 19 sediment samples; 6 ”scoop samples” from Loki’s castle, and 13 push-cores from Mohn’s treasure.
Because the material is of limited quantity and collecting new material is resource-demanding, some time was spent to decide on how to best preserve the samples during the analyses.

In order to prevent oxidation of the samples, a similar procedure to the one executed during the MarMine cruise was performed. The samples were first split and the material needed for the laboratory work was secured, while the remaining material was nitrogen flushed, vacuum packed and stored at -20°C. The splitting methods used are explained in section 4.2.

The samples consisted of mostly fine-grained sediments (sand-clay sized particles) with some larger fragments (diameter between 1-10cm). Fragments with a diameter above 1.0 cm were removed early in the splitting process, so the differences between the two size fractions could be evaluated. In total, 5 samples contained fragments that were separated from the sediments:

- LC-SAMLE-10007:
- LC-SS-10008-1
- LC-SS-10008-2
- MT-PC-10023-1
- MT-PC-10036>1/2

Initially the fragments were to be analysed only by XRD and XRF. However, further studies revealed that some of the fragments would be suitable for thin sections and would be interesting to analyse by automated mineralogy. The fine-grained sediment consisted of various size-fractions, from fine-grained clay to fine gravel-sized particles. The Mohn's treasure samples had more variations when it came to particle sizes while sediments from Loki's castle were more uniform.

Table 4.1 show and overview of all the samples collected. The table show that there is 2 different samples from 2 different locations at Loki's Castle; 10007 and 10008. The 10007 was collected from the flank of the mound, while 10008 was collected closer to the center and the black smokers. Table 4.1 show the the sampling method used, and a short description of the fragments.

**Table 4.1:** Table showing all the samples analysed and which ones contained fragments. LC=Loki's Castle, MT=Mohn's Treasure, SS=Scoop Sample, PC=Push Core.

| Location | Sampling method | Sample | nr. | ID | Fragments | Comment |
|---|---|---|---|---|---|---|
| LC | SS | 10007 | 1 | LC-SS-10007-1 | | |
| LC | SS | 10007 | 2 | LC-SS-10007-2 | | |
| LC | SS | 10007 | 3 | LC-SS-10007-3 | | |
| LC | SS | 10007 | Samle | LC-Samle-10007 | x | Large whtie and porous fragments. |
| LC | SS | 10008 | 1 | LC-SS-10008-1 | x | Dark grey and porous fragments, looking like hydrothermal chimney debris. |
| LC | SS | 10008 | 2 | LC-SS-10008-2 | x | Dark grey, green fragments looking like chimney debris. |
| MT | PC | 10023 | 1 | MT-PC-10023-1 | x | Two types of fragments. One group of fragments with a shale-like apperance, and one large rock with granitic scomposition which was analysed separately. |
| MT | PC | 10028 | 1 | MT-PC-10028-1 | | |
| MT | PC | 10029 | <5 | MT-PC-10029<5 | | |
| MT | PC | 10029 | >5 | MT-PC-10029>5 | | |
| MT | PC | 10031 | <5 | MT-PC-10031<5 | | |
| MT | PC | 10031 | >5 | MT-PC-10031>5 | | |
| MT | PC | 10033 | <1/2 | MT-PC-10033<1/2 | | |
| MT | PC | 10033 | >1/2 | MT-PC-10033>1/2 | | |
| MT | PC | 10035 | <1/2 | MT-PC-10035<1/2 | | |
| MT | PC | 10035 | >1/2 | MT-PC-10035>1/2 | | |
| MT | PC | 10036 | | MT-PC-10036>1/2 | x | Shale-like fragments with some larger grains of pyrite visible. |
| MT | PC | 10037 | <1/2 | MT-PC-10037<1/2 | | |
| MT | PC | 10037 | >1/2 | MT-PC-10037>1/2 | | |

## 4.2 Laboratory Methods

1. XRD
    - Sediments
    - Fragments
2. XRF
    - Sediments
    - Fragments
3. Automated Mineralogy
    - Selected sediment samples
    - Selected Fragments
4. External analysis performed at ALS
    - Selected sediment samples
5. Optical microscopy:
    - Thin sections of fragments.
    - Polished blocks of selected sediment samples.

### 4.2.1 Splitting

Sample preparation began with splitting into smaller representative sample sizes. The samples had an initial mass of approximately 1.5-2.0kg and an accurately executed splitting process was important in order to produce representative samples for all the laboratory methods planned. The sample sizes needed for each laboratory method varied, but between $10 - 20g$ was sufficient for each method. The laboratory methods are as follows:

After the samples had been defrosted they contained a considerable amount of water( figure 4.1 a and b). This led to the decision to first split the samples with a wet splitting step so the smaller samples could be dried efficiently. Splitting was done in two main steps. The first step was executed by a wet rotary splitter from ERIEZ (MACSALAB 12 way slurry splitter, figure 4.1c ), splitting each sample into 12. One of these 12 samples was then collected and dried in a heating cabinet for 24 hours at 60°C. The remaining 11 parts was then filtered, nitrogen-flushed, vacuum-packed before they were stored at -20°C. The dried sample was split using a dry rotary splitter (Retcsch minisplitter, figure 4.1f ), which split the sample into 8 parts, which all were collected for future analyses. Each of these samples contained between 10-30g depending on the inital sample weight.

The splitting process is illustrated in Figure 4.1 below.


**Figure 4.1:** Figure showing the splitting and drying process. a) show the inital sample sizes, b) defrosted samples, c) wet rotary splitter from ERIEZ, d) device for dewatering, e) samples after being dried in heating cabinet, f) dry rotary splitter (Retcsch)

After splitting, preparation for the laboratory analyses was executed:

### 4.2.2 XRD

Preparation for XRD and required two preceding grinding steps.The purpose of the first step was to reduce the particle size to $<50\mu m$, which was done using a Retch RS 200 vibratory disc mill. A tungsten-carbide grinding chamber along with a tungsten-carbide grinding element was utilized. 20-30g sample was put inside the grinding chamber and the speed was set to 1200rpm for 1.5 minutes. For some of the samples, 1.5 minutes grinding time was insufficient. For these samples the grinding time was increased to 2.5 minutes which was sufficient for most of the samples. However, some samples from Mohn's Treasure required up to three minutes. Preparation for XRF also require a grain size $< 50\mu m$, and the same powder as prepared for XRD was used for XRF (detailed discription of preparation for XRF is described in the next section). Figure 4.2 show the first grinding step. The fragments had to be crushed prior to the grinding in order to obtain the correct feeding size. This was done by using a fly press rock crusher.

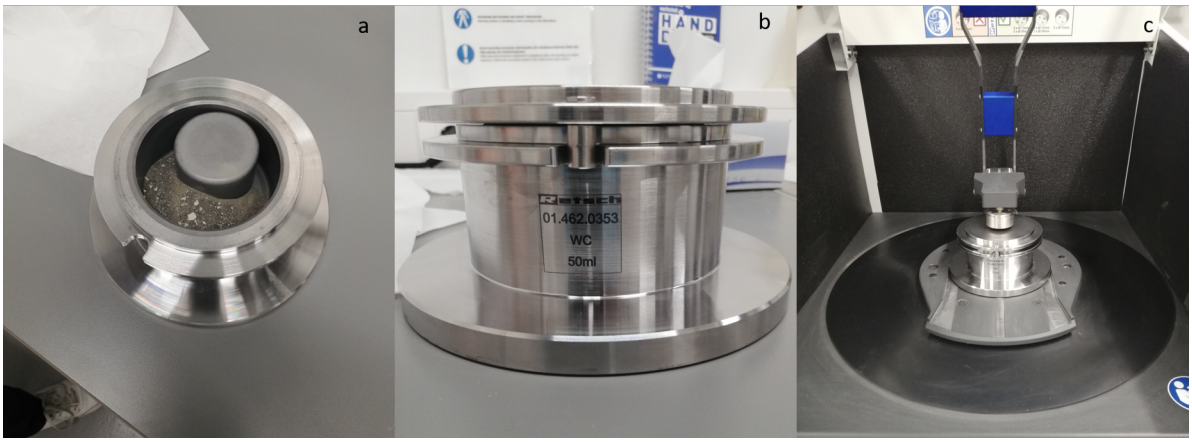


**Figure 4.2:** a) wolfram-carbide grinding chamber with sample powder inside, b) closed wolfram-carbide chamber,c) the vibratory disc mill.

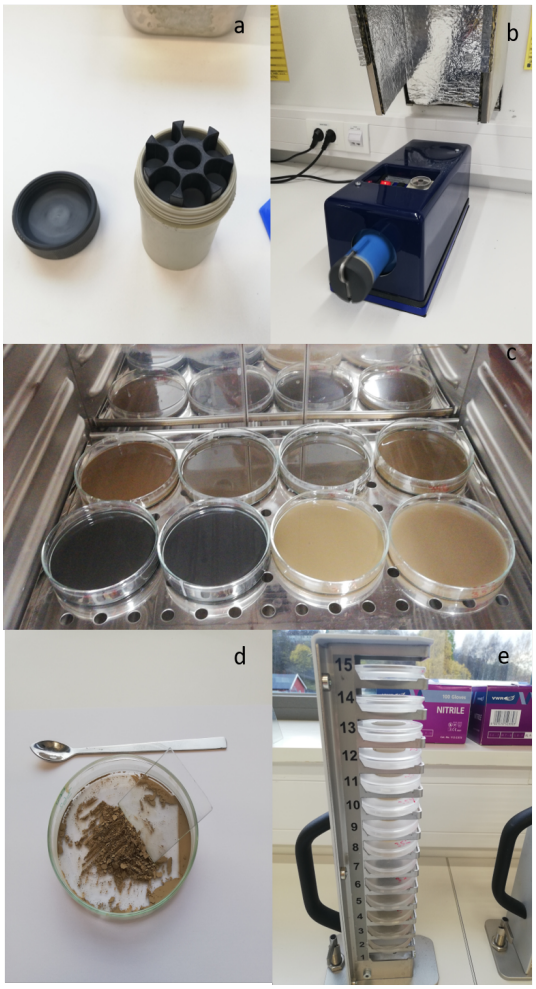


**Figure 4.3:** Figure showing the micronisation procedure. a) the grinding chamber with agate grinding sylinders, b) McCrone micronising mill, c) Samples put in the drying cabinet, d) dried sample, e) samples put in plastic containers, ready for XRD analysis.

The second grinding step is illustrated in figure 4.3 and the purpose of this step is to grind the particles to a round shape with size $<1\mu m$. $\sim$2g sample was put in the grinding chamber along with cylindrical agate grinding elements and $10mL$ ethanol, illustrated in figure 4.3 a. The grinding chamber was then put inside a McCrone micronising mill and was shaken for 1.5 minutes (figure 4.3 b). The samples were then dried in a heating cabinet at 60°C over night (figure 4.3 c and 4.3d), before they were put in the plastic containers shown in figure 4.3 e. The containers were then put in the XRD analyzer, a D8 advance from BRUKER were a cobalt anode was used as a source.

#### 4.2.2.1 Sulfur Estimations from XRD

The main goal from the XRD-analysis is to quantify the crystalline phases present in the samples. However the element concentrations can also be calculated based on the elements relative weight-proportions within each mineral phase. Due to uncertainties regarding sulfur-estimations by XRF (see discussion in section 6.1.1), such an estimation was done for this element. The relative proportions used are from webmineral.com and are shown in the table below:

**Table 4.2:** Relative proportions in weight.% from webmineral.com.

| | | Relative wt. Proportions | | | | | |
|---|---|---|---|---|---|---|---|
| Relevant Mineral Phases | Formula | S | Fe | Cu | Zn | Ba | O |
| pyrite | FeS2 | 0.5345 | 0.4655 | | | | |
| pyrrhotite | Fe(1-x)S | 0.3767 | 0.6233 | | | | |
| sphalerite | ZnS | 0.3290 | | | 0.6710 | | |
| isocubanite | CuFe2S3 | 0.3544 | 0.4115 | 0.2341 | | | |
| Barite | BaSO4 | 0.1374 | | | | 0.5884 | 0.2742 |

### 4.2.3 XRF

XRF was one of the methods used to identify trace- and main-elements in the samples. This method required the same primary grinding step as XRD (grain size $< 50\mu m$, and the same powder was used. XRF was executed on all of the samples and three different methods were performed:

- WROXI : Quantitaive main element analysis which require a melted glass pill.
- ProTrace: Quantitative trace element analysis which require a pressed powder pill.
- Omnian 37: Semi-quantitative main element analysis which require a pressed powder pill.

The main reason to perform two methods quantifying main elements, is due to uncertainties regarding the quantitative method. Specifically, the quantitative method was not designed/calibrated to quantify large concentrations of sulfur or Barium. Both of which had elevated concentrations in the samples (see discussion in section 6.1.1). The semi-quantitative method was performed in order to compare these results. The preparation of pressed powder pills and melted glass pills is explained below:

#### 4.2.3.1 Pressed powder pills

The preparation for pressed powder pills began with the mixing of 9.6g sample and 2.4g licowax. Sample and wax was then mixed in a fluxana vortex mixer(figure 4.4) for approximately 2 minutes to homogenize the mixture (Figure 4.4B). Then a hydraulic press($\sim 200kN$) was used to compress the sample to compact powder pills as seen on Figure 4.4C and D. The pressed pills were used for a quantitative trace-element analysis (ProTrace) as well as a semi-quantitative main element analysis(Omnian 37). The process is illustrated in Figure 4.4.


**Figure 4.4:** The preparation of pressed powder pills which were used for Omnian37 and ProTrace. a) powder sample, b) fluxana vortex mixer, c) hydraulic press, d) finished pressed pills.

#### 4.2.3.2 Melted glass pills

Quantification of main elements in a sample requires a melted glass pill. The preparation procedure starts with ignition of 2.5g sample at 1000°C for 4 hours. When the samples are exposed to this high temperatures, there will be a Loss Of Ignition(LOI) due to evaporation of some of the phases. The samples were weighed before and after ignition so that LOI could be calculated. After ignition, 0.500g of the powder sample is mixed with 5.000g of a flux agent consisting of 34% lithium-meta-borate and 66% lithium-tetra-borate. The flux agent is added to homogenize the sample and to facilitate the melting process. The combined flux and sample powder is then put into platinum crucibles as seen on figure 4.5c. $60\mu L$ of lithium-iodine is then added as a non-wetting agent (NWA). This is done in order to strengthen the surface tension in the melt, making it easier to remove the glass from the crucible as well as decreasing the probability of cracking.
The platinum crucibles containing the samples are then placed in the furnace, a Theox advanced fluxer from Claisse shown in Figure 4.5d. Some of the samples had to be remelted due to cracking as they cooled. These were added additional lithium-iodine($60\mu L$) to increase the surface tension further. This applies for sample LC-SS-10007-1, LC-SS-10007-2, LC-SS-10007-3, LC-SS-10008-1, LC-SS-10008-2, and the fragment from samples LC-SS-10008-1 and LC-SS-10008-2. The fragment from samples LC-SS-10008-1 was not successfully melted and was analysed only by Omnian 37 and ProTrace.

Elevated concentrations of sulfides were detected in sample LC-samle-10007-4, LC-SS-10008-1 and LC-SS-10008-2 by the previously executed XRD analysis.High concentrations of sulfur can cause damage to the platinum crucibles during melting. In attempt to avoid this, 2.5g of lithium-nitrate was added to sample LC-samle-10007-4, LC-SS-10008-1 and LC-SS-10008-2. Willis (2010)


**Figure 4.5:** The preparation for main element analysis by XRF. A) Samples after ingition, B) & C) Powder mixed with the flux-agent in platinum crucibles, D) The Theox advanced fluxer furnace from Claisse, E) Solidified glass pill in platinum container.

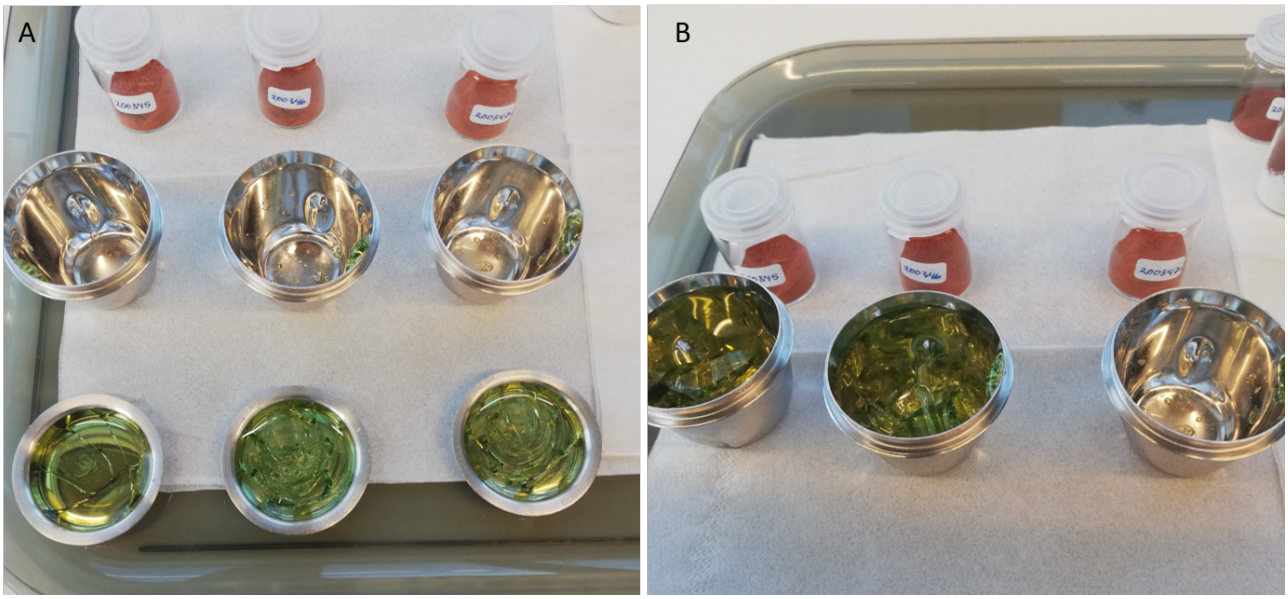


**Figure 4.6:** Showing some if the failed melting attempts were the glass cracked during crystallization. A) Cracked glass pills, B) The glass was put back in the platinum cups and remelted. In attempts to avoid cracking $120\mu L$ of Lithium-iodine was added before remelting in order to increase the surface tension of the melt to avoid cracking.

### 4.2.4 Particle Size Distribution

For particle size determination a Malvern Mastersizer 3000, illustrated in figure B.2, was used. Sediment sample is dispersed in water using a HYDRO EV disperser (figure B.2). The disperser is equipped with an Ultrasound setting in order to break part any agglomerated particles. The HYDRO EV disperser is directly connected to the mastersizer by a plastic tube, which goes through the mastersizer and back into the water disperser. The mastersizer consist of a laser, and detectors to register the diffraction angles.


**Figure 4.7:** The set-up for particle size determination showing the malvern Mastersizer 3000 with the HYDRO EV disperser in the front

### 4.2.5 Optical microscopy

Microscopy was performed on polished blocks of sediments as well as on thin sections made from the fragments. The same blocks and thin sections were also used for the Automated mineralogy, described further below (section4.2.6).

#### 4.2.5.1 Polished Blocks of Sediment samples

5 of the sediment samples was decided as being of interest to study through SEM and optical microscopy. These samples are the ones that have shown higher contents of base metals, and metal-bearing sulfides through the previously executed analyses.


**Figure 4.8:** Quantachrome micro riffler used to split the sediment samples in order to make plished blocks.

The preparation for polished blocks requires 2-3g sample for each block. In order to achieve this sample size the samples had to be split further. A micro rotary riffler from Quantachrome was used for this splitting step. The sediment samples split were:

- MT-PC-10036
- MT-PC-10037
- LC-SS-10007-2
- LC-SAMLE-10007
- LC-SS-10008-2

After splitting, on of the parts from each sample was made into a polished block. The blocks were then examined optically before they were carbon-coated and analysed by AMS.

#### 4.2.5.2 Polished Thin-sections and Blocks of Fragments

Some of the fragments separated from the sediments were large enough to make polished thin sections. Some of fragments were to fragile to be made into thin-sections and were made into polished blocks in stead. In total, 5 larger fragments from 4 of the sediment samples was assumed as being suitable, due to their size and hardness. Only sample LC-SAMLE-10007 did not contain large enough fragments to produce a thin section nor a block. These fragments was only analysed by XRF and XRD. The fragments made into thin sections were taken from samples:

- LC-SS-10008-1: Polished block. One chimney-fragment consisting mostly of sulfides. The fragment had an apparent hydrothermal vein going through the center.

- LC-SS-10008-2: This Section. These samples contained fragments similar to sample LC-SS-10008-1, containing black chimney fragments. One large fragment stood out with a different mineralogy. This fragment appeared lighter grey and also contained some mushy green phases. The fragment was chosen for thin section in order to examine these phases.
- MT-PC-10036>1/2: Thin section. Fragment containing visible grains of sulfides assumed to be pyrite, in what is thought to be a shale.
- MT-PC-10023-1: These samples contained two groups of fragments:
  - MT-PC-10023-1-1: Thin section. One large fragment with what looks like granitic composition and texture.
  - MT-PC-10023-1-2: Thin section. One group consisting of several fragments which all looked like a type of shale.

The fragments were photographed and are shown in the figure below. After the thin sections were described optically they were carbon-coated and analysed by AMS.


**Figure 4.9:** The fragments that were suitable for thin sections from samples a) LC-SS-10008-1, b) LC-SS-10008-2, c) MT-PC-10036>1/2, d) MT-PC-10023-1-1 and e) MT-PC-10023-1-2. Fragment d) and e) were both picked from sample MT-PC-10023-1.

### 4.2.6 Automated Mineralogy

The AMS used for this project is a Zeiss Sigma 300VP Scanning electron microscope (SEM). The software used for this project is ZeissMineralogic. Due the samples containing complex particles consisting of several phases that were intergrown, it was concluded that mapping would be the best method, rather than spot centroid. An Energy dispersive spectrometer (EDS) of the type Xflash 6-60 from BRUKER was used as collector, and the working distance was set to 8.5mm. Mapping was first executed with a step-size of 20$\mu m$, before some of the interesting areas were mapped more detailed

with $2\mu m$ step size.

Due to time-limitations, not all of the sediment blocks were mapped by AMS. The blocks that contained most sulfides and/or oxides after optical microscopy were prioritised. The sediment blocks analysed were:

- LC-SS-10008-2
- MT-PC-10036>1/2

### 4.2.7 ALS

Eight of the sediment samples were sent to ALS laboratory for further chemical analysis. The method ordered was Aqua Regia With ICP-MS Finish ME-MS41™, and REE quantification was also added to the method. One of the reasons to perform this external analysis was to get an accredited result so that the methods performed at NTNU could be quality controlled. The samples selected for accredited analysis are those who contained considerable amounts of metals, sulfur and barium, since these elements were the ones that did not fit the methods performed at NTNU. The samples sent to ALS were:

- MT-PC-10036
- MT-PC-10037
- LC-SS-10007-1
- LC-SS-10007-2
- LC-SS-10007-3
- LC-SAMLE-10007
- LC-SS-10008-1
- LC-SS-10008-2

After the results from ALS was received, some of the samples contained Ba- and Cu-concentrations above the Limit Of Detection (LOD). This was the case for sample LC-SAMLE-10007 which contained Ba above LOD, and samples LC-SS-10008-1 and LC-SS-10008-2 which contained Cu above LOD. For these samples, two methods fit for analysing only the Ba- and Cu-contents were requested. These were the methods; Cu-OG46 for Cu-contents and ME-XRF15b for Ba-concentrations.

**Table 4.3:** Overview of the laboratory methods performed on each sample and fragment.PB=Polished Block, PTS=Polished Thin Section, PSD=Particle Size Distribution.

| Sample | Fragments Separated? | | | | XRD | XRF | Polished Blocks | | ALS | PSD |
|---|---|---|---|---|---|---|---|---|---|---|
| | XRF | XRD | Microscopy | AMS | | | Microscopy | AMS | | |
| LC-SS-10007-1 | | | | | x | x | | | x | x |
| LC-SS-10007-2 | | | | | x | x | x | | x | x |
| LC-SS-10007-3 | | | | | x | x | | | x | x |
| LC-Samle-10007 | x | x | | | x | x | x | | x | x |
| LC-SS-10008-1 | x | x | PB | x | x | x | | | x | x |
| LC-SS-10008-2 | x | x | PTS | x | x | x | x | x | x | x |
| MT-PC-10023-1 | x | x | 2 PTS | x | x | x | | | | x |
| MT-PC-10028-1 | | | | | x | x | | | | x |
| MT-PC-10029<5 | | | | | x | x | | | | x |
| MT-PC-10029>5 | | | | | x | x | | | | x |
| MT-PC-10031<5 | | | | | x | x | | | | x |
| MT-PC-10031>5 | | | | | x | x | | | | x |
| MT-PC-10033<1/2 | | | | | x | x | | | | x |
| MT-PC-10033>1/2 | | | | | x | x | | | | x |
| MT-PC-10035<1/2 | | | | | x | x | | | | x |
| MT-PC-10035>1/2 | | | | | x | x | | | | x |
| MT-PC-10036>1/2 | x | x | PTS | x | x | x | x | x | x | x |
| MT-PC-10037<1/2 | | | | | x | x | | | | x |
| MT-PC-10037>1/2 | | | | | x | x | | | x | x |

Chapter 5

# Results

The following chapter presents the results gathered from the previously described methods. The results are split in two main sections were the first section presents the results from the sediments, and the second section presents the results from the fragments.

## 5.1 Sediments

### 5.1.1 XRD

XRD was the first analytical method performed on the samples and gave the initial interpretation of the mineralogy of the samples. Figure 5.1 presents the XRD results from the sediments. The results are semi-quantitative due to a large amount of amorphous phases, which made the quantification as well as identification complicated. All the XRD plots can be found in appendix B.

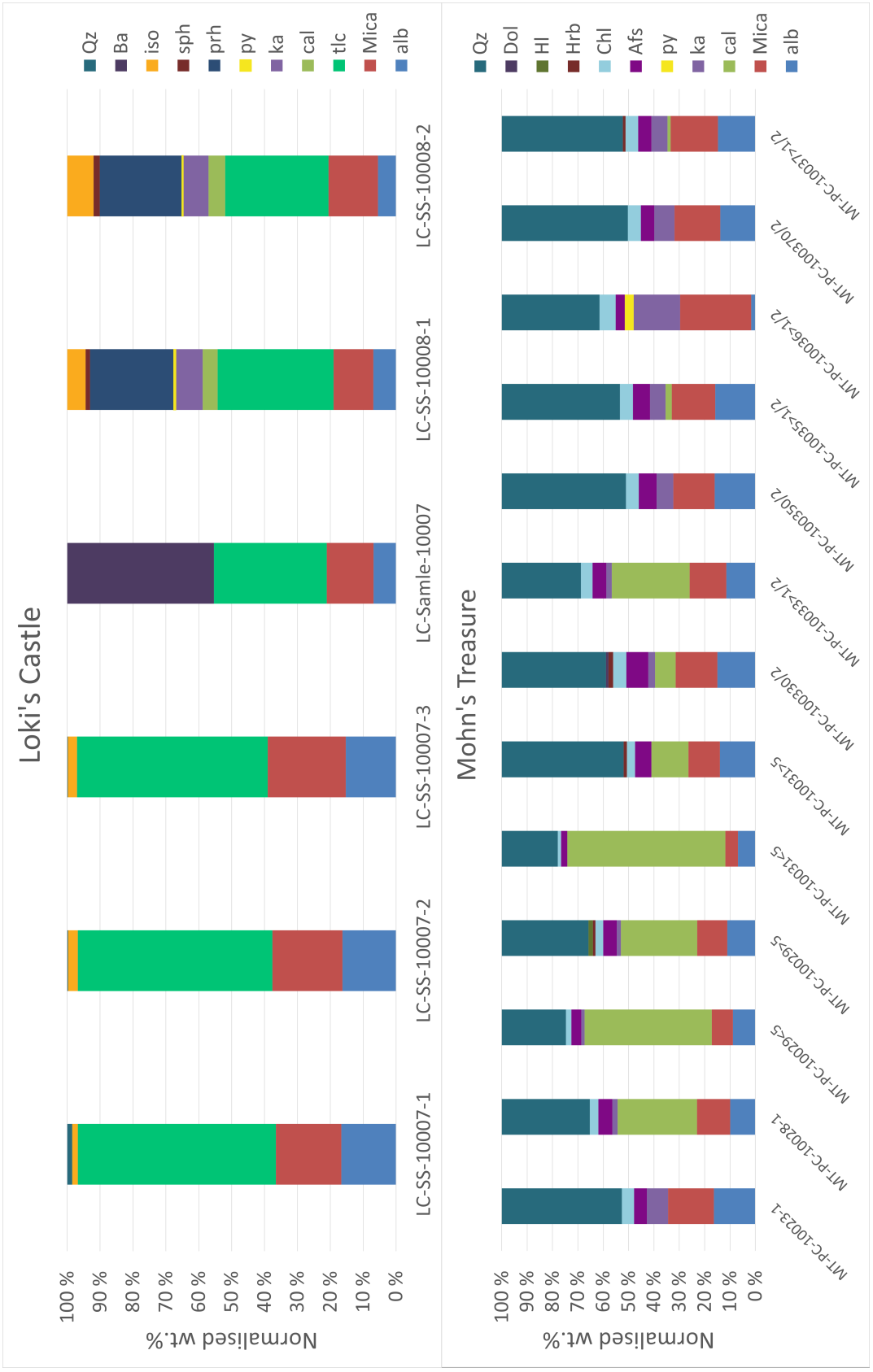


**Figure 5.1:** XRD results for the sediment samples. All results should be considered as semi-quantitative due to large amounts of amorphous phases, especially in the samples from Loki's Castle.

As explained in chapter 4.2.3 there are some uncertainties regarding the quantification of sulfur by

XRF. Because of these uncertainties, the sulfur concentrations were also calculated from the XRD-results based on the quantified sulfide phases. The purpose of these calculations is to compare them with the semi-quantitative, the quantitative and the ALS methods. The purpose is to verify the quality of the XRD analysis as well as the XRF method.

**Table 5.1:** Sulfur concentration calculated by using reltaive weight proportions of sulfur for each sulfide-bearing phase.

| | Sulfur Estimated from XRD | | | | | | | |
|---|---|---|---|---|---|---|---|---|
| | LC-SS-10007-1 | LC-SS-10007-2 | LC-SS-10007-3 | LC-Samle-10007 | LC-SS-10008-1 | LC-SS-10008-2 | MT-PC-10036>1/2 | MT-PC-10037>1/2 |
| Pyrite | | | | | 0.42 | 0.30 | 1.75 | |
| Pyrrhotite | | | | | 9.55 | 9.34 | | |
| Sphalerite | | | | | 0.44 | 0.61 | | |
| Isocubanite | 0.61 | 1.05 | 0.99 | 0.71 | 1.98 | 2.83 | | |
| Barite | | | | 6.01 | | | | |
| Total S (wt.%) | 0.61 | 1.05 | 0.99 | 6.72 | 12.39 | 13.08 | 1.75 | 0 |

The total sulfur concentrated calculated from each sample is plotted below:

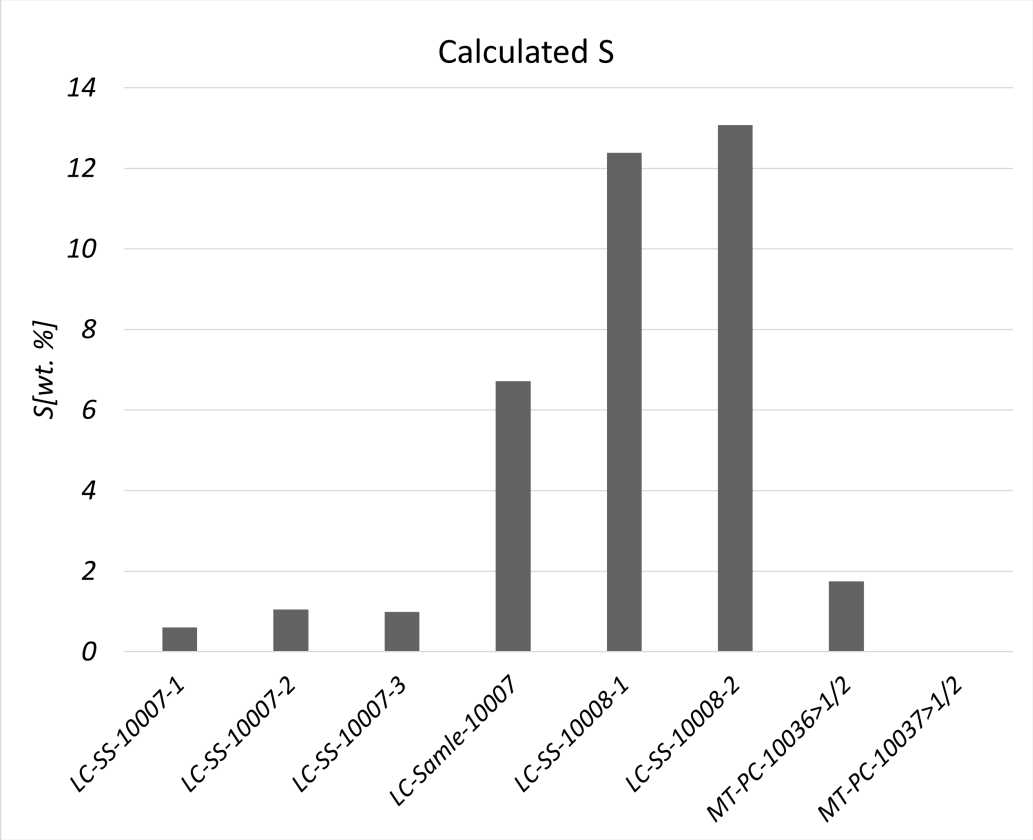


**Figure 5.2:** Calculated total sulfur-concentrations, for the sediment samples sent to ALS.

### 5.1.2 Optical microscopy and Stub Images

Microscopy of the sediment samples was done on polished blocks, hence only reflected light was used. The microscopy was executed in order to get an initial idea of the sulfide phases. Another important part of the reflected light microscopy was to look for chalcopyrite-isocubanite inter-growths, as was shown in Snook et al. (2018). Optical microscopy was also thought to be important to do prior to the automated mineralogy in order to easier classify the phases.

**LC-SS-10008-2:**

This block consist of a fine-grained matrix containing larger euhedral to subhedral particles. Small grains of sulfides are present in the matrix, but are hard to identify due to their small size ($<10\mu m$). Most likely the small sulfides are pyrite, pyrrhotite or chalcopyrite/isocubanite. In the larger particles both chalcopyrite, pyrrhotite and sphalerite is likely the main sulfide phases.
Pyrrhotite occur both flaky and as euhedral round or square grains with varying sizes (from 1-250 $\mu m$). This phase is recognized due to the characteristic anisotropy of the grains. Chalcopyrite also appear in the sample, both both as small inclusions within talc and as larger grains (figure 5.3). Small chalcopyrite and sphalerite inclusions occur in larger dark grey particles as seen in figure 5.3, which were proven by automated mineralogy to be talc.

**LC-SS-10007-2:**

The sample consist of fine-grained powder with some larger particles. Sulfides is not as present as was expected from the XRF and XRD analyses. However, due to the high concentration of amorphous phases the results from the XRD is semi-quantitative and might not be comparable. Some small inclusion of chalcopyrite is present within some of the larger particles. The inclusions are between 1-10 $\mu m$ and usually occur in the center of a darker gray phase similar to sample LC-SS-10008-2, which is likely talc. Pyrite occur as larger grains of between 10-100 $\mu m$. Some of the pyrite grains are also elongated and appear flaky.

**LC-SAMLE-10007:**

The sample consist of a fine-grained matrix with larger euhedral particles and grains. Most of the sulfides are present occur as inclusions in the larger particles and or occur as individual small grains in the matrix. The sulfide phases observed are pyrite, pyrrhotite and chalcopyrite. Pyrite sometimes occur covered with a darker grey rim. This is interpreted as being an iron oxide which have formed as the sulfides have been exposed to more oxidising conditions. In this sample chalcopyrite is also present as small inclusions in talc as seen in the previous samples.
Pyrite occur in varying sizes usually as euhedral grains. Unlike chalcopyrite, pyrite mostly occur as single grains consisting only of pyrite.

**MT-PC-10036 >1/2:**

The polished block consist of a very fine-grained matrix with larger particles and grins evenly distributed throughout the sample.

The main ore minerals present is pyrite of varying grain size. Pyrite occur both as large individual grains and as small inclusions within other particles. The largest pyrite grains has diameters between 1-2.5 mm, while the smallest inclusions are only a couple of $\mu m$ wide (figure 5.4. In the sample two large pyrite grains are present, one of them are shown in figure 5.4 A, B and C. The pyrite typically show an alteration rim surrounding it, as well as within cracks of the particle. As shown in figure 5.4 B and C the alteration product is a type of iron oxide, likely formed as result of oxidation.

**MT-PC-10037 >1/2:**

This sample did not contain reflective phases of considerable amount, and consisted of a fine-grained matrix with some larger particles similar to the background of sample MT-PC-10036 $> 1/2$.

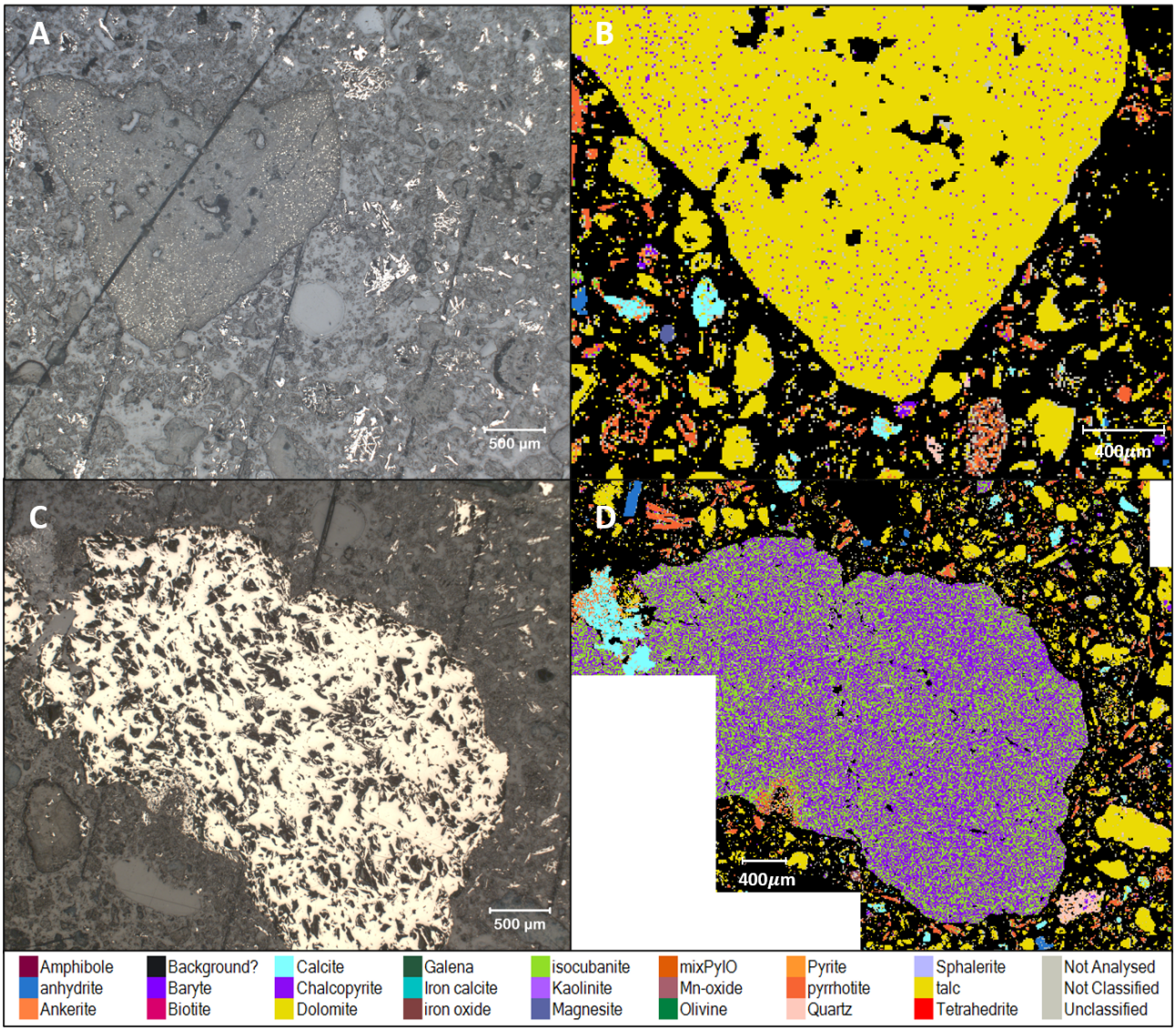


**Figure 5.3:** Collage showing the most interesting observation from Sediment sample LC-SS-10008-2. A) Showing chalcopyrite intergrowths in talc. B) Shows the AMS stub image of the same area as A. C) chalcopyrite grain. C) The same chalcopyrite grain from the AMS analysis. The green areas within the grain are parts that are richer in Cu, and was included to attempt to search for isocubanite intergrowths. However, the intergrowths were not visible by microscope, and is likely a Cu-richer chalcopyrite.

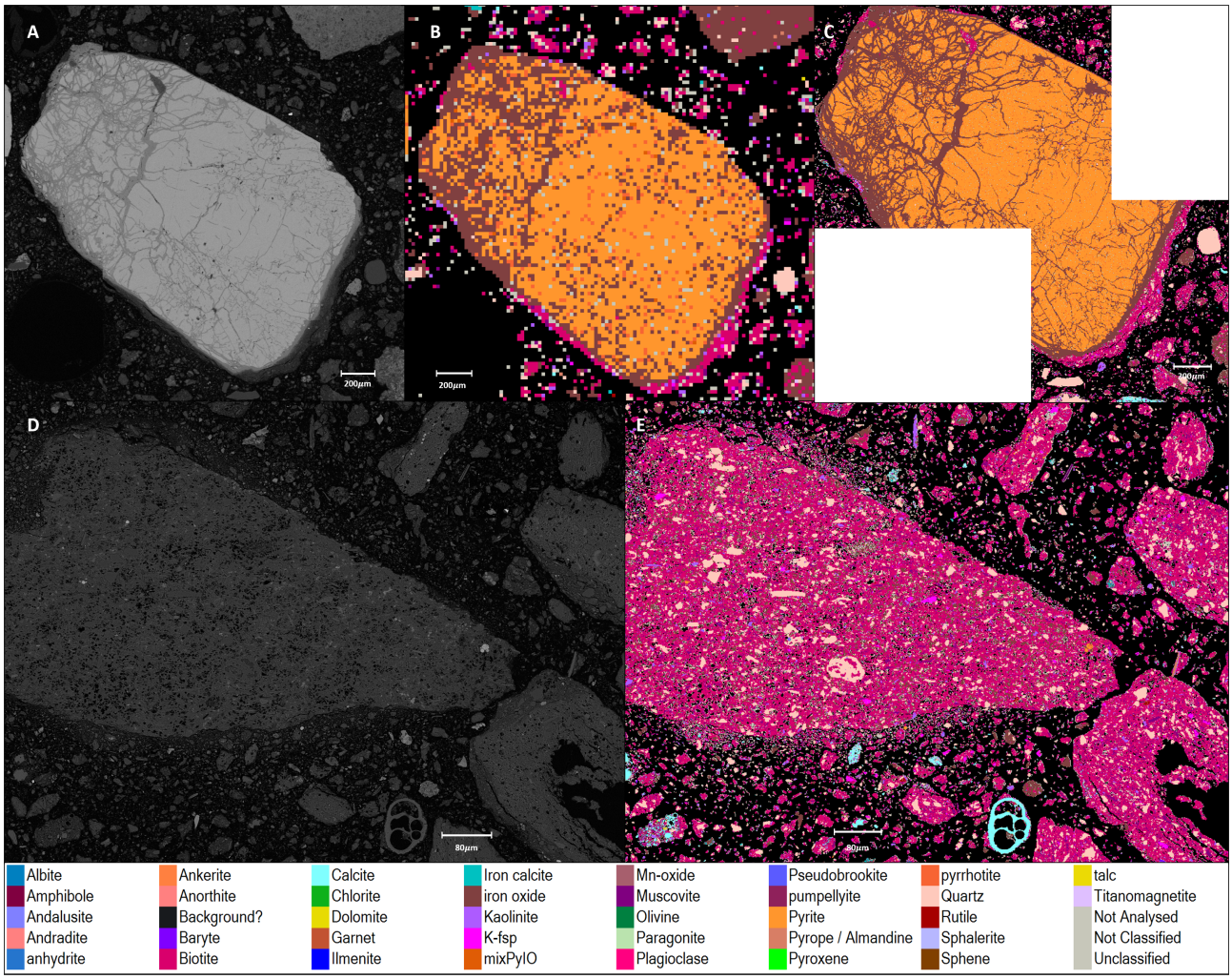


**Figure 5.4:** Collage showing the most interesting observation from Sediment sample MT-PC-10036$> 1/2$. A) Showing EDS of the pyrite grain. B) The grain mapped with $20\mu m$ step size, and C) $2\mu m$ step size. D) EDS of a typical particle from the Mohn's Treasure sample. E) $2\mu m$ mapping of the same grain. The particle consist of several mineral phases including quartz, bitotie, kaolinite, feldspar and pyrite.

### 5.1.3 AMS

Table 5.2 show the modal mineralogy obtained from the $20\mu m$ mapping of the two sediment blocks. Due to time-limitations only two of the blocks were mapped by automated mineralogy. The two blocks were MT-PC-10036$> 1/2$ and LC-SS-10008-2. It was a priority to map one block from each site, and the ones who showed the most interesting features by optical microscopy were chosen.

**Table 5.2:** Table showing the modal mineralogy by AMS

| | **MT-PC-10036** | **LC-SS-10008-2** |
|---|---|---|
| | **wt.%** | **wt.%** |
| *anhydrite* | 0.01 | 0.90 |
| *pyrrhotite* | 0.21 | 12.37 |
| *isocubanite* | 0.00 | 9.42 |
| *Chalcopyrite* | 0.00 | 42.92 |
| *Pyrite* | 2.96 | 2.73 |
| *Magnesite* | *n.i* | 0.04 |
| *Galena* | *n.i* | 0.00 |
| *Biotite* | 37.42 | 0.00 |
| *mixPyIO* | 0.02 | 0.35 |
| *talc* | 0.01 | 22.51 |
| *Baryte* | 0.09 | 0.55 |
| *Dolomite* | 0.00 | 0.18 |
| *Anorthite* | 0.03 | *n.i* |
| *Amphibole* | 0.00 | 0.01 |
| *Sphalerite* | 0.00 | 0.15 |
| *Chlorite* | 0.0002 | *n.i* |
| *Rutile* | 0.06 | *n.i* |
| *Albite* | 0.02 | *n.i* |
| *K-fsp* | 0.48 | *n.i* |
| *Muscovite* | 5.38 | *n.i* |
| *Pseudobrookite* | 0.02 | *n.i* |
| *Kaolinite* | 2.61 | *n.i* |
| *Pyrope / Almandine* | 0.63 | *n.i* |
| *Quartz* | 7.88 | 0.79 |
| *iron oxide* | 40.37 | 2.61 |
| *Olivine* | 0.00 | 0.01 |
| *Calcite* | 0.82 | 4.40 |
| *pumpellyite* | 0.71 | *n.i* |
| *Titanomagnetite* | 0.07 | *n.i* |
| *Iron calcite* | 0.07 | 0.04 |
| *Unclassified area%* | 4.96 | 3.04 |
| **Sum:** | 100 | 100 |

### 5.1.4 XRF

The following section gives a presentation of the chemical analysis performed by XRF through a series of diagrams based on the theory presented in chapter 3.1. Full XRF results from the quantitative main element analysis, WROXI, is attached in appendix B, figure B.3 and B.4.

#### 5.1.4.1 Aluminium and Iron Concentrations

Below, the criteria presented in section 3.2 are illustrated together with the results for Al, Fe and Mn concentrations obtained by XRF. The estimated concentrations are from the WROXI method. Detailed discussion as to why this method has been chosen for these plots are described in chapter 6.1.1. Samples that plot below y= 0.3 and above x= 0.5 are the ones that fulfill the criteria to qualify as metalliferous. The third criteria is added as a a colour bar on the right side of the diagram. The appointed color of the data point illustrate the calculated ratio. The ratios below 2.5 falls outside the criteria for metalliferous sediments, and is marked by a change in colours.

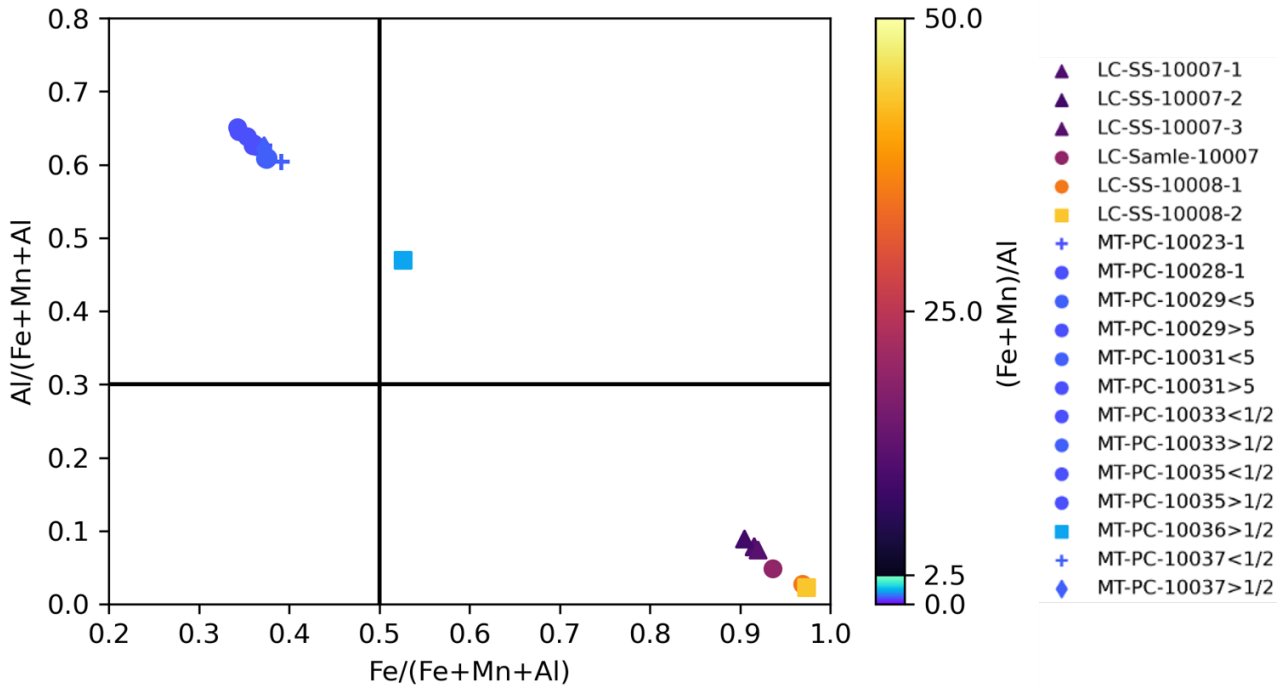


**Figure 5.5:** Figure showing the criteria to characterise sediments as metalliferous. The lines represent the criteria presented in section 3.2. The bar to the right illustrate the values from the third criteria, and the color of the plotted points illustrate the calculated ratio. Colors below 2.5 are the ones that did not fulfill the criteria.

It is noticeable how the data set plot in a negative linear pattern. This behaviour is created due to the lack of Manganese(Mn) present in the samples. I.e the ratios are practically independent of the Mn concentration for these sediments.

The samples from Mohn's treasure are the ones plotting in the upper left quadrant, while the samples plotting in the lower right, are from Loki's Castle. The square shaped point plotting in the upper right quadrant is from Mohn's Treasure and is the only sample from this location that fulfill one of the three criteria (Fe/(Fe+Mn+Al)>0.5), sample MT-PC-10036>1/2.

### 5.1.4.2 Metal Grades

Base metal grades obtained from the WROXI method are presented in figure 5.6. The samples from Mohn's treasure are not included due to their low grades.

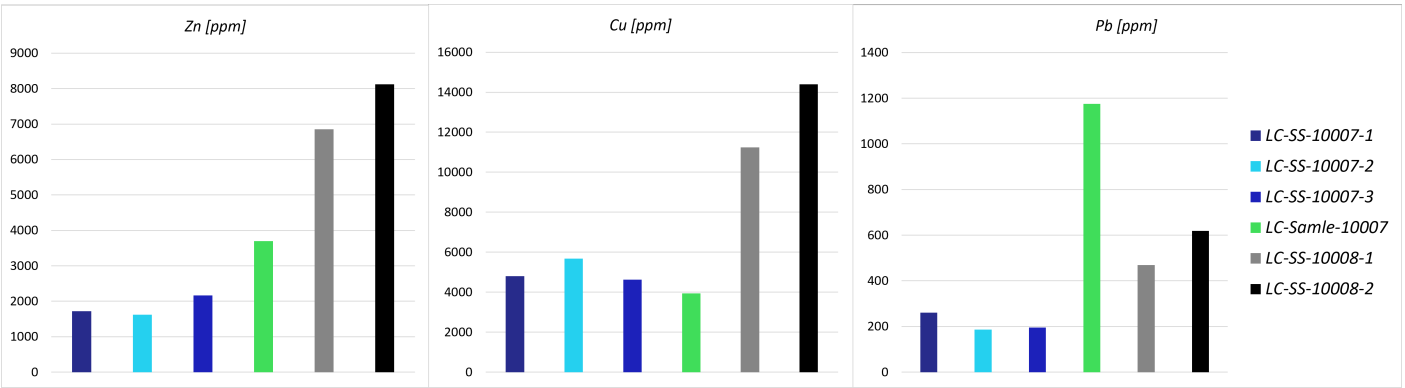


**Figure 5.6:** Base metal grades in sediments from Loki's Castle. Estimated by the WROXI method.

Figure 5.7 show the Fe-concentrations estimated by the WROXI method. The samples from Mohn's Treasure that are coloured red and orange are the ones that were sent to ALS for accredited analyses.

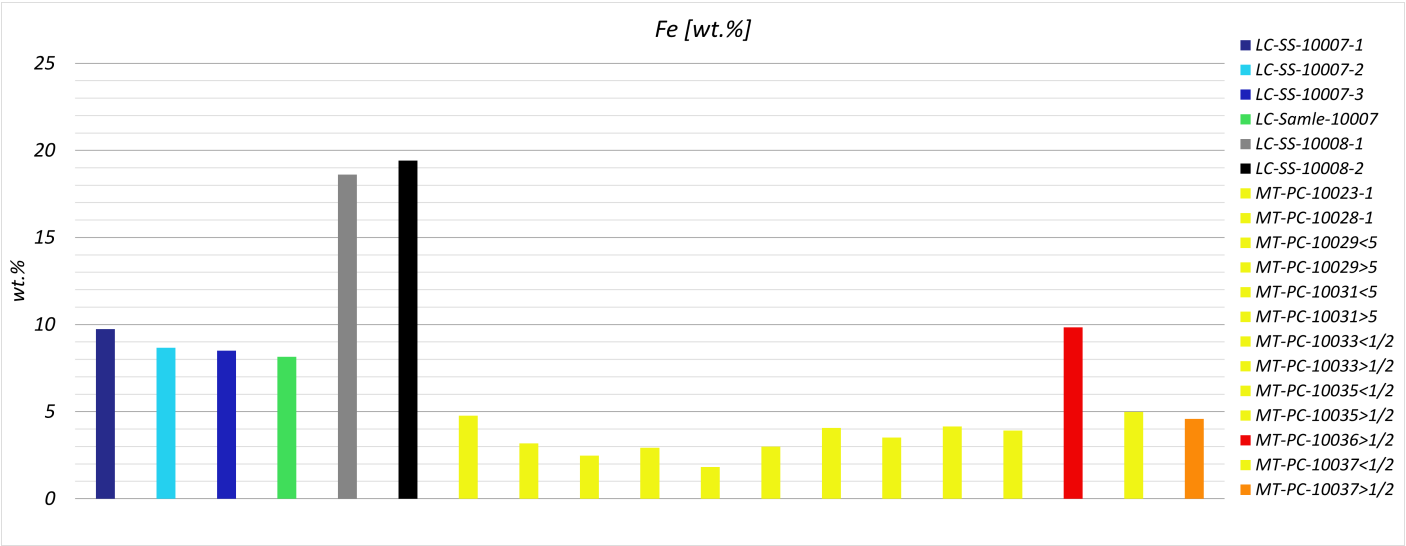


**Figure 5.7:** Iron concentrations in the samples collected from Loki's castle and Mohn's treasure.

The following figures show the precious metal grades and their correlation with total base metal grades. Figure 5.8 show the correlations for silver while figure 5.9 show the correaltions with gold.

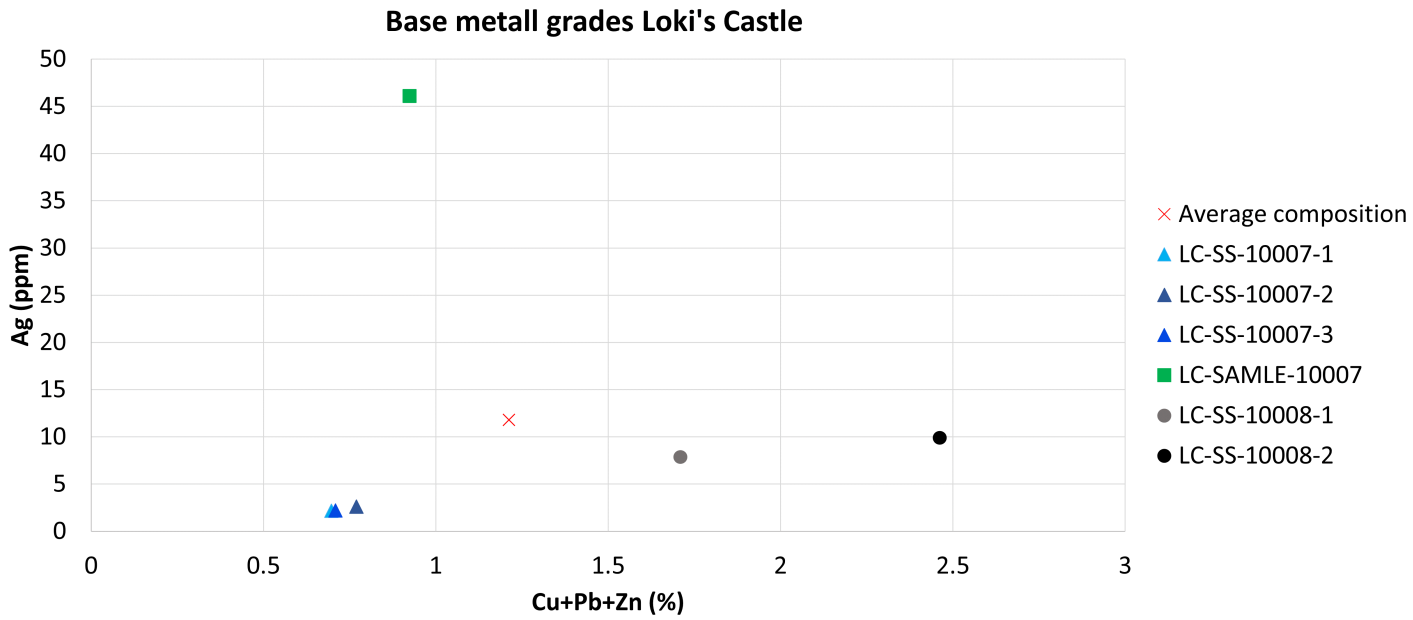


**Figure 5.8:** Figure showing correlation between Ag and total base metal concentration.

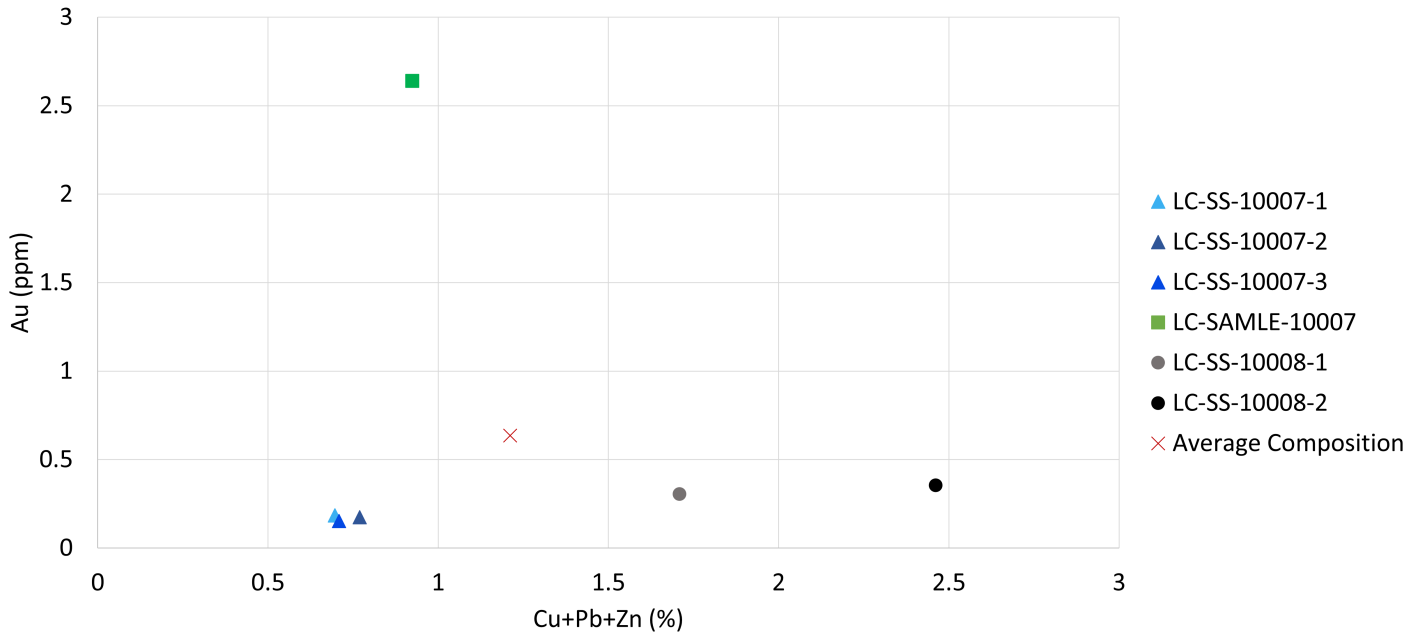


**Figure 5.9:** Figure showing correlation between Au and total base metal concentration. Au grades are from ALS, while base metals are from the WROXI method.

As seen in figure 5.8 and 5.9 there is no linear correlation between base metal concentrations and precious metal concentrations.

Figure 5.10 shows the Base metal grades plotted in the ternary phase diagram proposed by Large (1992) and Franklin et al. (2005) along with CR=60, and ZR= 60 and 90.

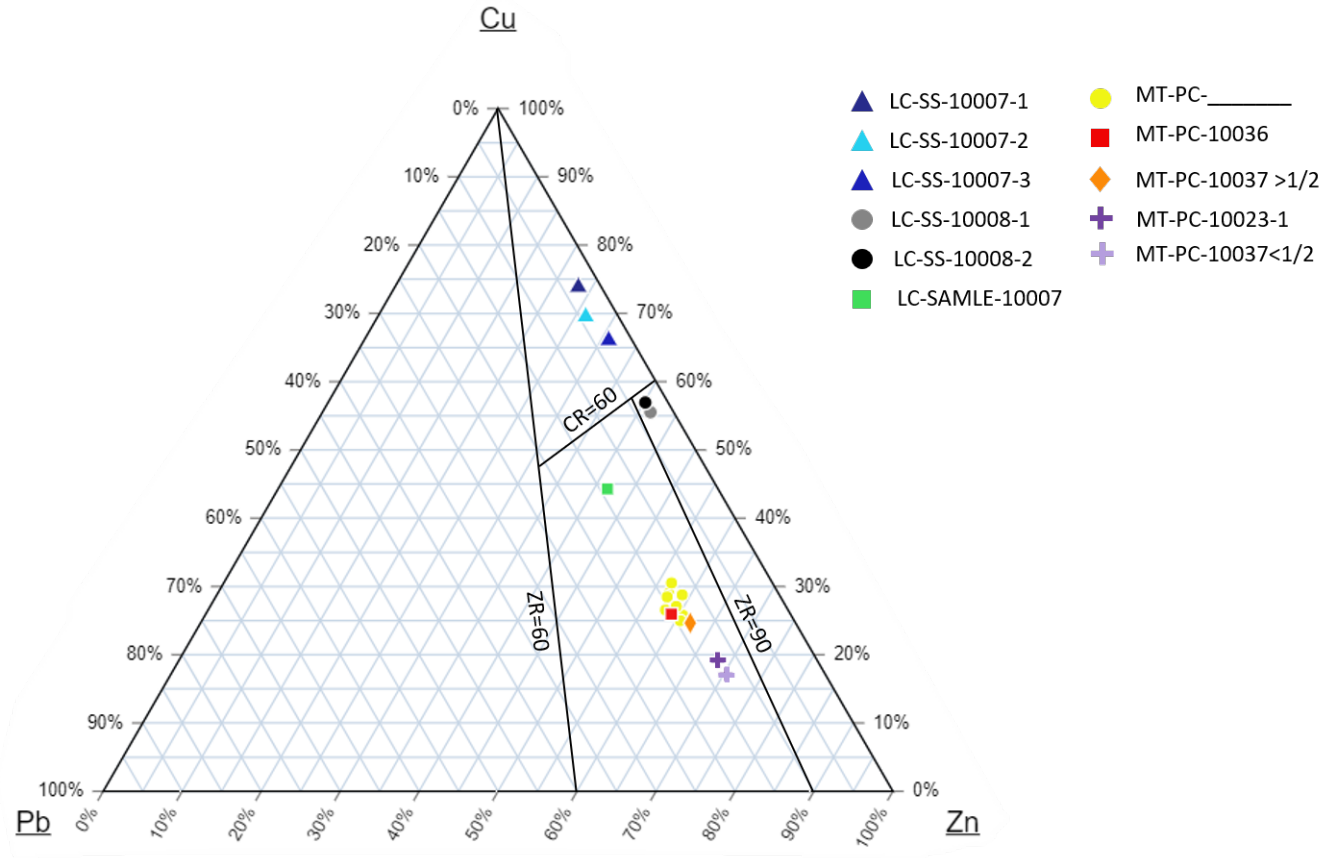


**Figure 5.10:** Cu-Pb-Zn diagram using the base metal grades obtained using the WROXI method.

### 5.1.5 Determination of the Hydrothermal Component

The scheme proposed by Metz et al. (1988), presented in section 3.2.2 was performed on the sediment samples. Calculated hydrothermal components are showed in table 5.3, which show the calculated hydrothermal components as well as the corresponding Fe-concentrations. Figure 5.11 show the hydrothermal component and iron concentrations from Mohn's Treasure plotted together. The method is thought to be applicable for the sediments found at Mohn's Treasure because of the similarities between the Mid-Atlantic ridge and the Arctic Mid-ocean ridge.

The results from Loki's castle were also plotted in a similar way (figure B.1, appendix B, but the method was not applicable for the sediments from this site. Hydrothermal components from Loki's castle were calculated between 90-100%. The high hydrothermal component together makes the results from Loki's castle plot in a vertical pattern rather than a linear correlation. The high hydrothermal component is caused by low concentrations of Al-rich phases and biogenous material.

**Table 5.3:** Calculated hydrothermal components from Loki's Castle and Mohn's Treasure. These data are calculated based on the WROXI method and carbonates are estimated by XRD.

| Sample | Hydrothermal component wt.% | Fe wt.% |
|---|---|---|
| LC-SS-10007-1 | 91.6 | 9.7 |
| LC-SS-10007-2 | 91.5 | 8.7 |
| LC-SS-10007-3 | 93.2 | 8.5 |
| LC-Samle-10007 | 95.8 | 8.1 |
| LC-SS-10008-1 | 90.1 | 18.6 |
| LC-SS-10008-2 | 90.4 | 19.4 |
| MT-PC-10023-1 | 19.7 | 4.8 |
| MT-PC-10028-1 | 14.3 | 3.2 |
| MT-PC-10029<5 | 10.1 | 2.5 |
| MT-PC-10029>5 | 19.0 | 2.9 |
| MT-PC-10031<5 | 8.9 | 1.8 |
| MT-PC-10031>5 | 29.3 | 3.0 |
| MT-PC-10033<1/2 | 20.1 | 4.1 |
| MT-PC-10033>1/2 | 12.7 | 3.5 |
| MT-PC-10035<1/2 | 25.2 | 4.1 |
| MT-PC-10035>1/2 | 23.5 | 3.9 |
| MT-PC-10037<1/2 | 23.2 | 5.0 |
| MT-PC-10036>1/2 | 12.1 | 9.8 |
| MT-PC-10037>1/2 | 22.2 | 4.6 |

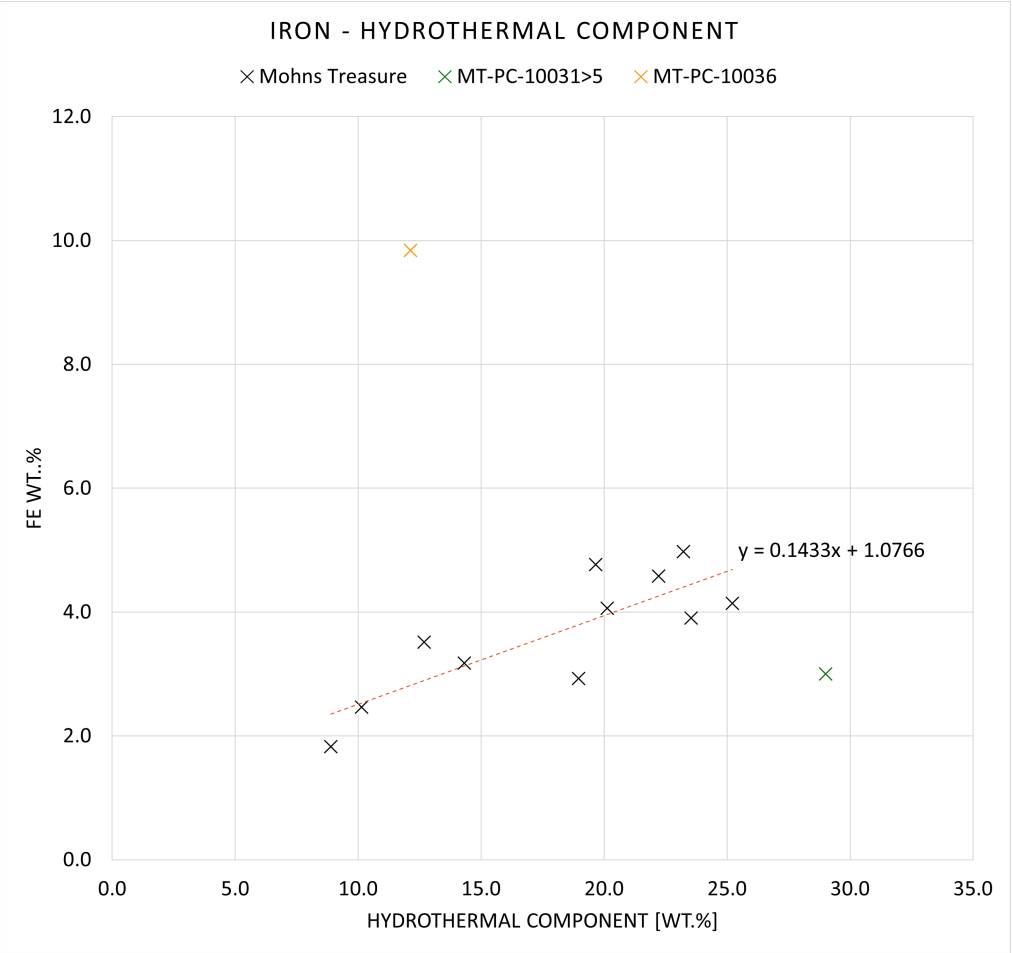


**Figure 5.11:** Estimation of hydrothermal component vs total iron content. The hydrothermal component is calculated using the WROXI data and the calcite estimations from XRD. The Fe-concentrations are also from WROXI. The linear regression were performed only on the black points and has a gradient of $0.14$ and $R^2 = 0.67$.

The calculated hydrothermal component was also plotted against the chlorite content estimated by XRD. This was done in order to evaluate if the chlorite formed at Mohn'sTreasure might be the result of low temperature alteration as a consequence of diffuse venting in the area:

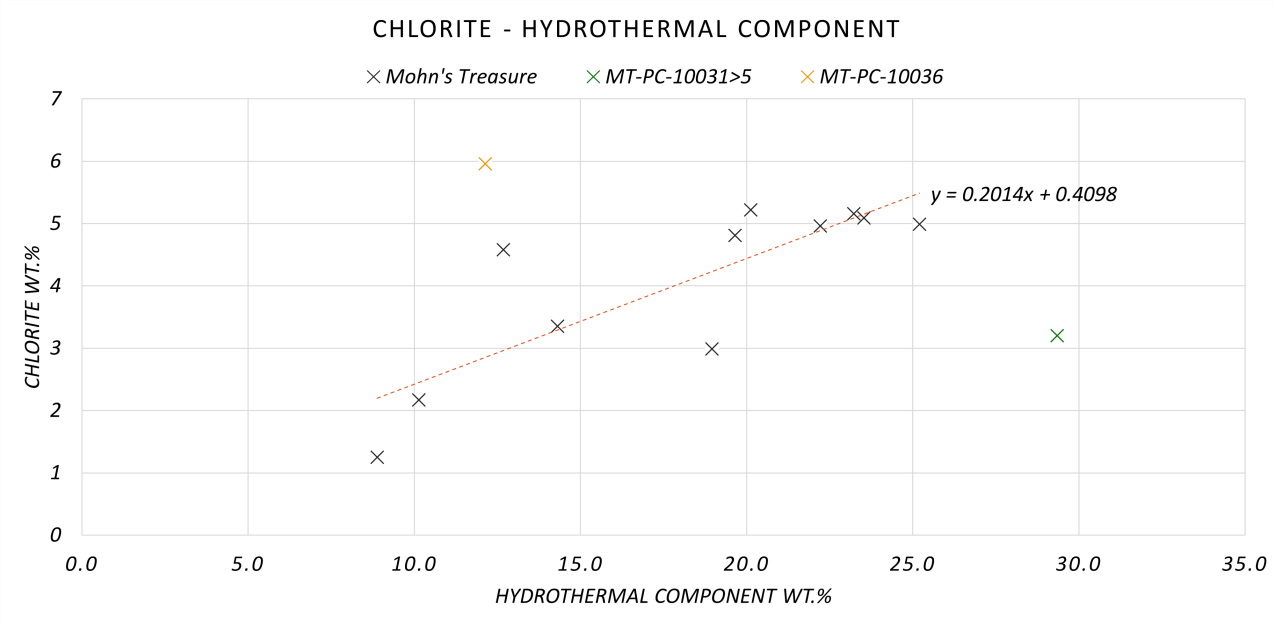


**Figure 5.12:** Chlorite concentrations from XRD plotted against the calculated hydrothermal component. Chlorite estimations are from the XRD-analysis, while the hydrothermal component was calculated based on the data from the WROXI method as well as the calcite-concentrations estimated from XRD. The linear regression is performed using the black points and has a gradient of 0.20 and $R^2 = 0.68$

### 5.1.6 ALS

Table below show selected element concentrations from the accredited analysis. The full ALS analysis results recieved is attached in appendix B.3

**Table 5.4:** Selected element concentrations from ALS.

| | Cu | Zn | Pb | Fe | S | Au | Ag | Mo | Ni | Co | Mn | As | Cd | Sb | Ba |
|---|---|---|---|---|---|---|---|---|---|---|---|---|---|---|---|
| | (ppm) | (ppm) | (ppm) | (%) | (%) | (ppm) | (ppm) | (ppm) | (ppm) | (ppm) | (ppm) | (ppm) | (ppm) | (ppm) | (ppm) |
| *LC-SS-10007-1* | 4960 | 1735 | 271 | 9.52 | 0.9 | 0.184 | 2.19 | 11.35 | 1.82 | 9.83 | 513 | 85.8 | 2.15 | 1.46 | 573 |
| *LC-SS-10007-2* | 5860 | 1635 | 201 | 8.43 | 1.44 | 0.174 | 2.61 | 6.29 | 2.13 | 11.8 | 485 | 74.7 | 3.06 | 1.235 | 164.5 |
| *LC-SS-10007-3* | 4750 | 2150 | 189.5 | 8.09 | 1.75 | 0.153 | 2.2 | 6.01 | 3.13 | 8.66 | 498 | 59.8 | 5.53 | 1.125 | 138.5 |
| *LC-Samle-10007* | 4250 | 3710 | 1280 | 8.73 | 2.44 | 2.64 | 46.1 | 21.7 | 25.5 | 15.6 | 1450 | 505 | 8.89 | 17.2 | 174500 |
| *LC-SS-10008-1* | 9870 | 6690 | 533 | 17.3 | 10 | 0.305 | 7.85 | 6.96 | 1.52 | 27.6 | 522 | 117 | 23 | 2.91 | 33.3 |
| *LC-SS-10008-2* | 15950 | 8030 | 637 | 19.6 | >10 | 0.355 | 9.88 | 4.59 | 0.97 | 40.2 | 652 | 131.5 | 27.8 | 3.68 | 40.4 |
| *MT-PC-10036 >1/2* | 50.1 | 103 | 24.6 | 9.14 | 1.12 | 0.0014 | 0.117 | 15.45 | 99.1 | 22.8 | 809 | 36.9 | 0.105 | 0.898 | 363 |
| *MT-PC-10037>1/2* | 39.5 | 91.3 | 17.15 | 3.89 | 0.05 | 0.0014 | 0.009 | 2.22 | 39.1 | 17.35 | 632 | 26.1 | 0.046 | 0.428 | 101.5 |

The data received from ALS included a REE-package. Chondrite-normalised REE patterns for the samples are shown in figure 5.13.

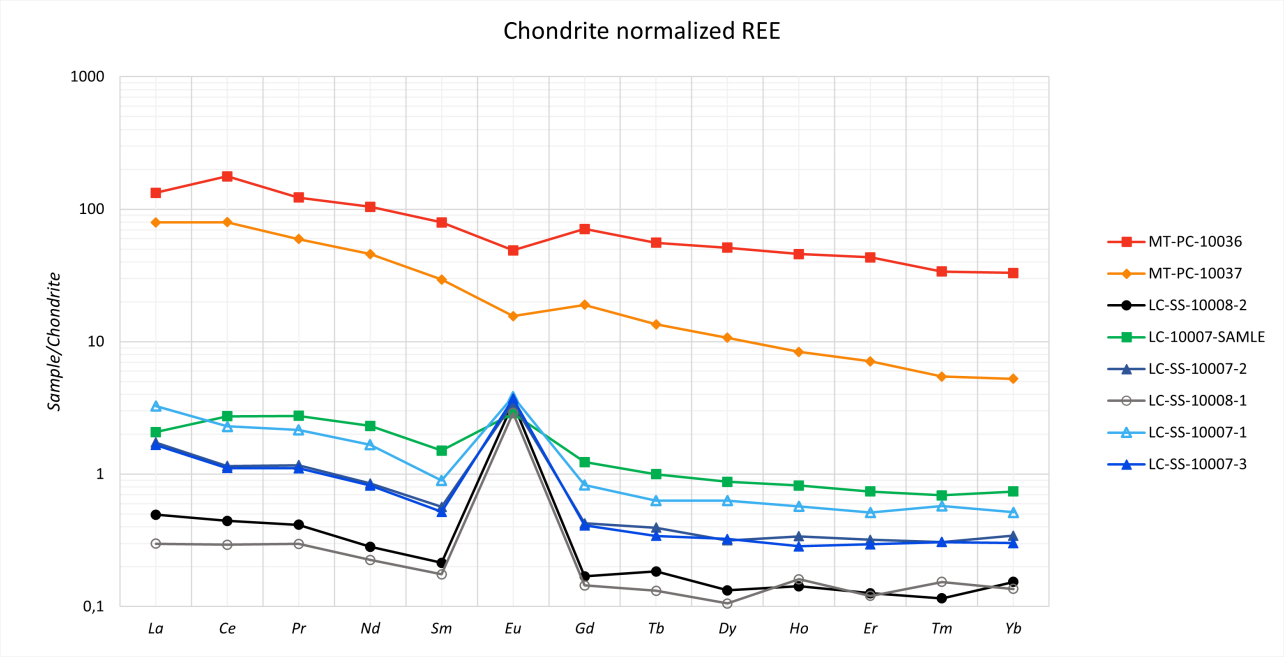


**Figure 5.13:** Chondrite normalized REE patterns for the samples sent to ALS.

### 5.1.6.1 Correlation Plots

The results obtained from ALS is compared to the XRF analysis performed at NTNU by the correlation plots presented in figure 5.14 Base metal, iron, sulfur and precious metal concentrations are of particular interest. The figure below show how well the performed XRF methods correlate with the ICP-MS method performed at ALS. The blue line presents y=x, were the correlation is 1.

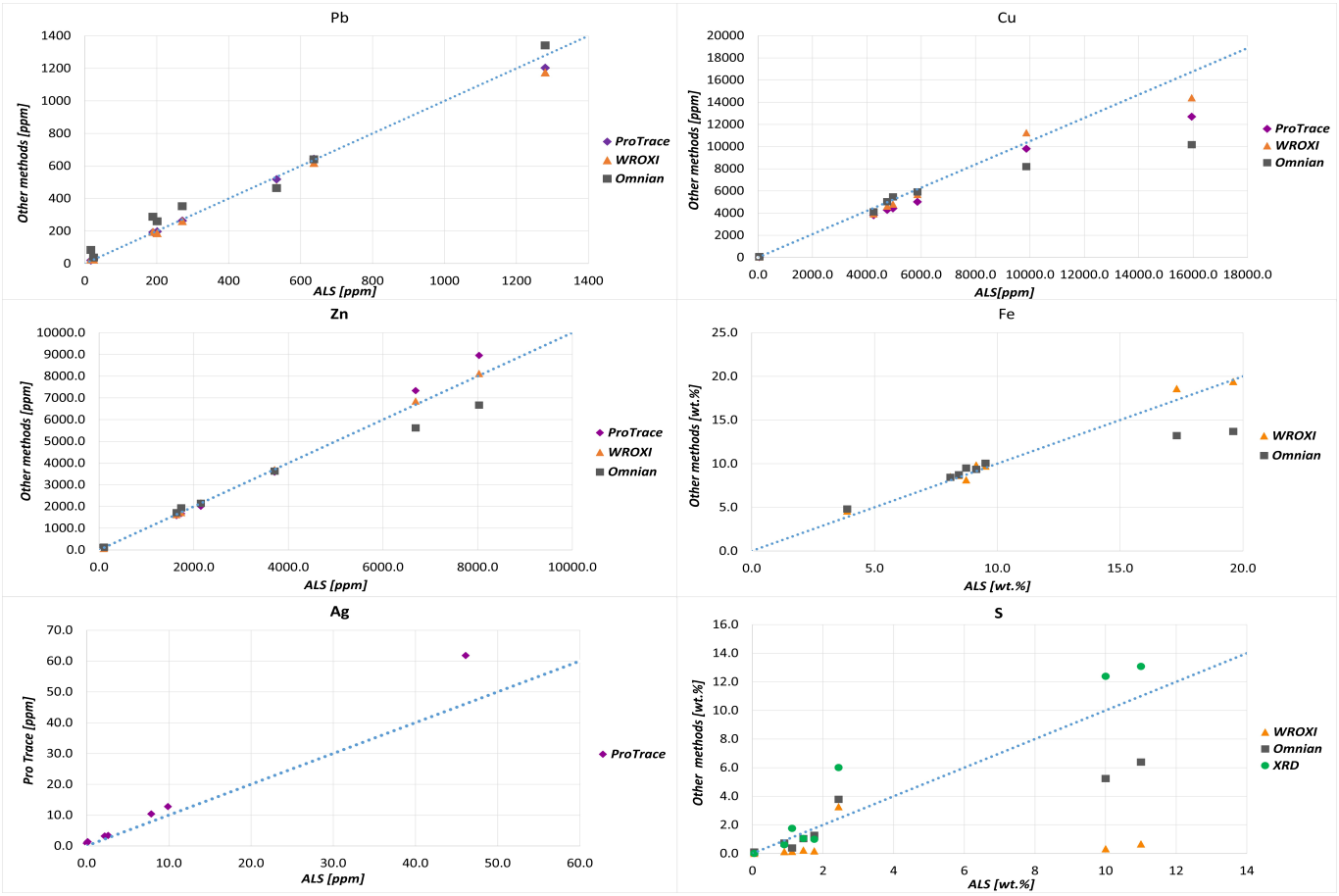


**Figure 5.14:** Correlation plots comparing the results from ALS, Omnian, WROXI and ProTrace.

## 5.2 Fragments

### 5.2.1 XRD

Figure 5.15 presents the XRD analysis of the fragments from Loki's Castle and Mohn's Treasure.

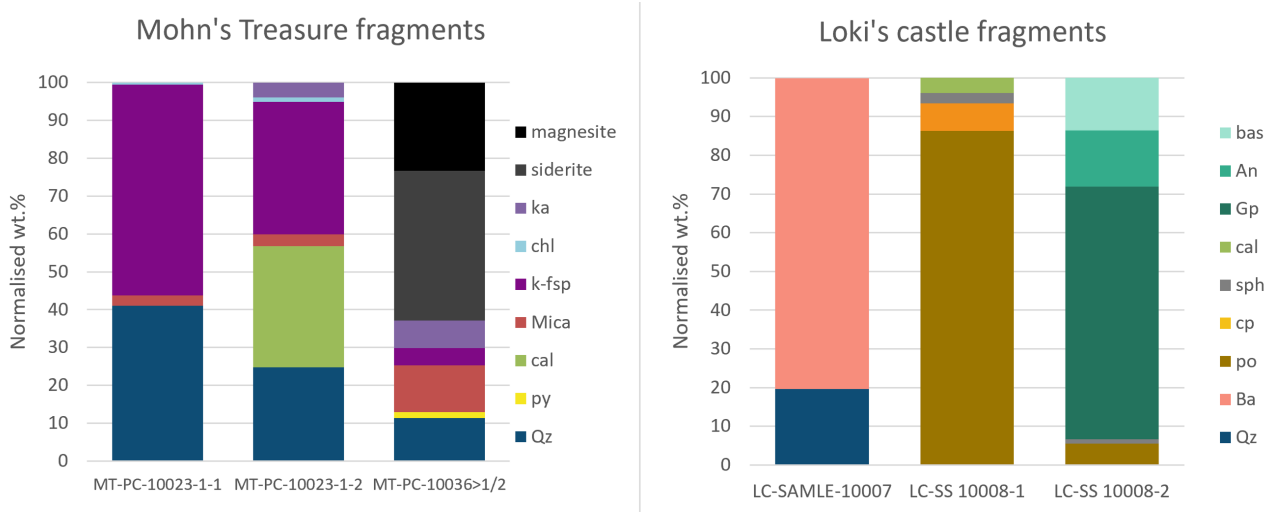


**Figure 5.15:** Results from the XRD analysis performed on the fragments.

### 5.2.2 Optical Microscopy and AMS Stub Images

All the fragments apart from LC-SAMLE-10007 were made into polished thin sections and observations from optical microscopy as well as stub images from the automated mineralogy is presented below. Full montages of the automated mineralogy maps are attached in appendix B.

**LC-SS-10008-1:**

Sample LC-SS-10008-1 contained several fragments. Most of them was black, porous with some visible sulfides as well some oxidised material. These fragments were all thought to be chimney fragments. One of these fragments was chosen to be made into a polished block, while the rest of the fragments were analysed by XRF and XRD.

By microscopy it was confirmed that the fragment consisted approximately 80% sulfides, in which 90-95% occur as pyrrhotite. The pyrrhotite have grown outwards from a vein propagating the center of the fragment. This gives the pyrrhotite an elongated shape. The size of the pyrite grains vary across the block, with the smallest grains closest to the vein and an increasingly larger grain size outwards from the vein.

Isocubanite is also present but as smaller grains shown in figure B.5 B and C. Isocubanite is often associated with a grey phase proven to be sphalerite by AMS(figure B.5 C. The isocubanite is not as elongated as the pyrite, but occur as cubic and circular grains. Some of the isocubanite is also found as intergrowths inside the pyrrhotite. A zonation of from the inner wall of the vein was observed by AMS, and isocubanite is more frequent towards the center of the vein (figure B.5 D). This correspond to the highest temperatures occuring closest to the vein. Automated mineralogy also showed that talc has formed towards the edge of the fragment along with iron-oxides. These phases have likely formed due to the surface of the fragment being directly exposed to seawater and more oxidising conditions.

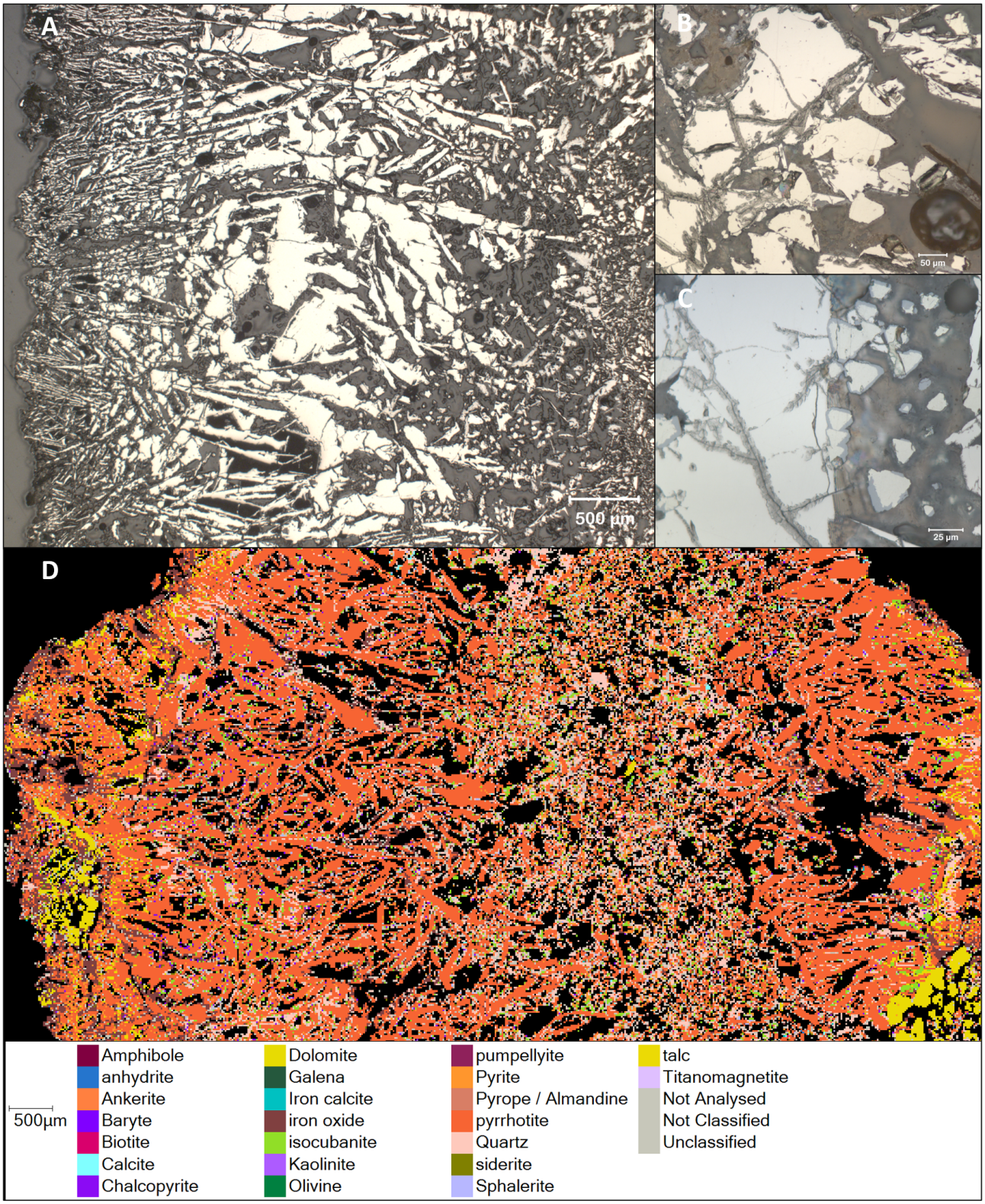


**Figure 5.16:** Collage showing the most interesting observation from the chimney fragment from LC-SS-10008-1. A) Cross section of the vein, B) Isocubanite showing a slightly darker yellow to the brighter pyrrhotite, C) Triangular grains of isocubanite with sphalerite rims, D) automated mineralogy of the polished block.

**LC-SS-10008-2:**

This sample also contained several fragments, made of the same material as the fragments found in LC-10008-1. However, one of the fragments contained white and green/gray mushy phases as well. This fragment was found to be of interest to analyse separately and was chosen to be made into a polished thin section and to be analysed by XRD and XRF.

The sample contains fibrous bassanite, gypsum and anhydrite. Bassanite occur as long fibrous grains with an aspect ration of approximately 45, with a length of 1-2.5$mm$, and a width of 10-50$\mu m$. Anhydrite has a more square shape with an aspect ratio of 1.5-2.0, and lengths of approximately 100-300$\mu m$ . Gypsum occur in larger concentrations and likely make up between 50-60% of the sample. The gypsum occur as subhedral grains and both the anhydrite and bassanite exist as euhedral fibres cutting through the gypsum matrix.

Sulfides are not present in any large extent, but there are some very small elongated grains of pyrite in some parts of the sample which are shown in figure B.6 A.

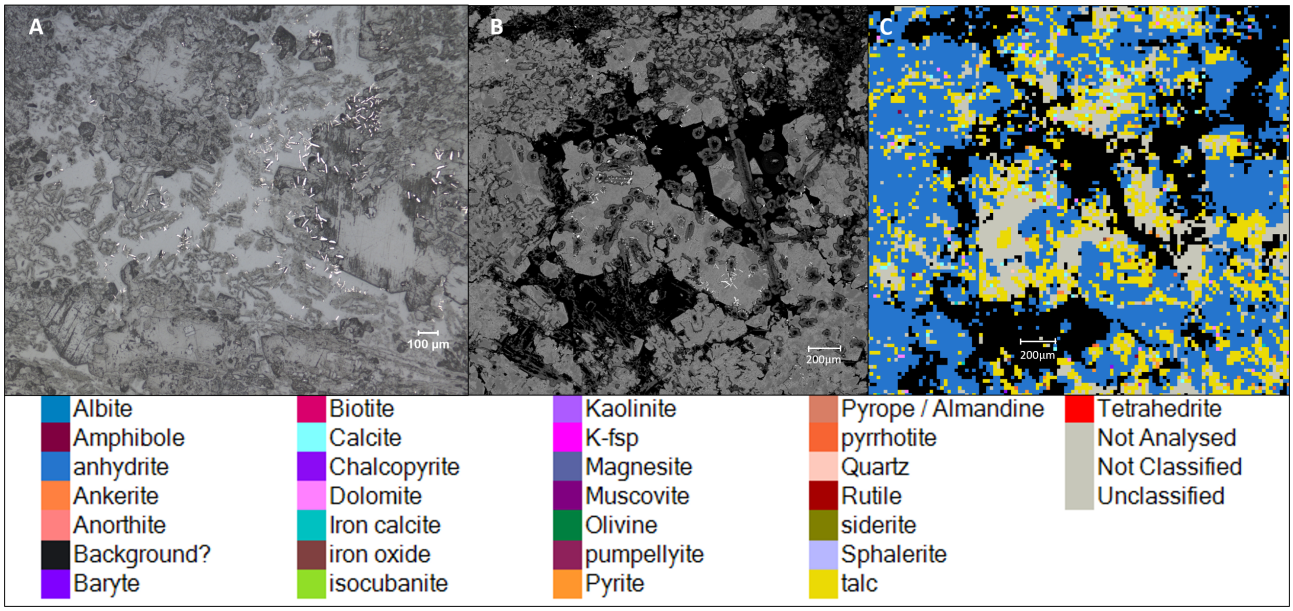


**Figure 5.17:** Picture from the fragment collected from sample LC-SS-10008-2 A) Small sulfide grains in Reflected light , B) EDS image of similar sulfide grains from the same sample, C) The same area mapped by AMS.

**LC-SAMLE-10007:**

The fragments were too small to make into thin sections, and the fragments from this sample were only analysed by XRF and XRD.

**MT-PC-10023-1-1:**

The fragment consist mainly of quartz( 50%), feldspar( 40%) and biotite ( 5%) (figure 5.18). Based on the composition of the sample as well as the texture of the sample, the fragment can be described as granitic. Pyrite is not present in a significant amount.

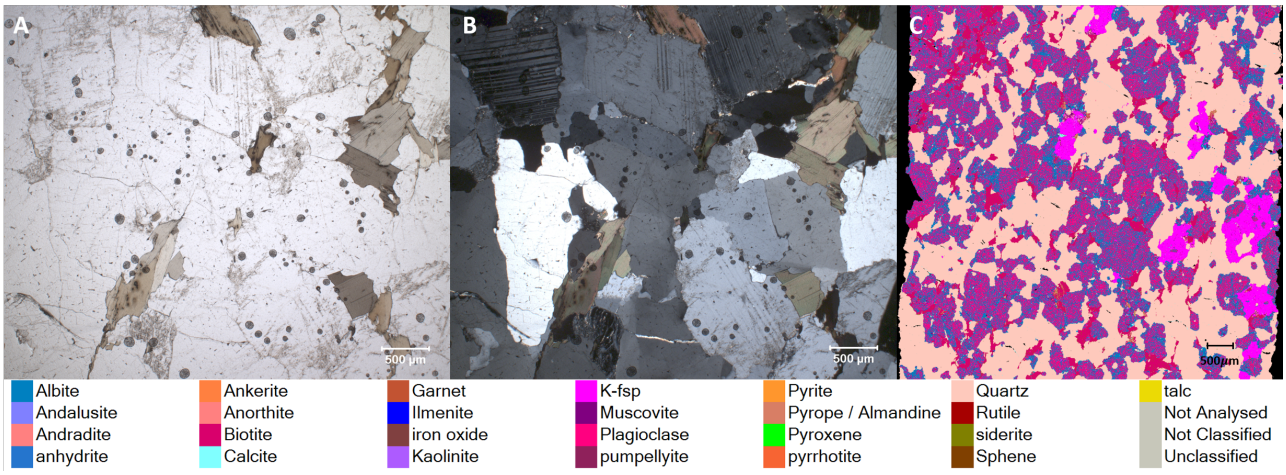


**Figure 5.18:** The granitic fragment in A) plane polarised light, B) cross polarised light and C) the fragment as analysed by automated mineralogy.

**MT-PC-10023-1-2:**

The main rock forming phases present in this sample is quartz, feldspar and calcite, which occur as individual grains with sizes varying between 20-100$\mu m$ (figure 5.19). The sample contain some layers which also contain some darker brown and opaque phases which were difficult to identify through microscopy. In reflected light the grains showed a gray color and a clear anisotropy. Automated mineralogy confirmed these phases to be iron-rich oxides. Some of the grains also have a distinct red internal reflection and identified as rutile.

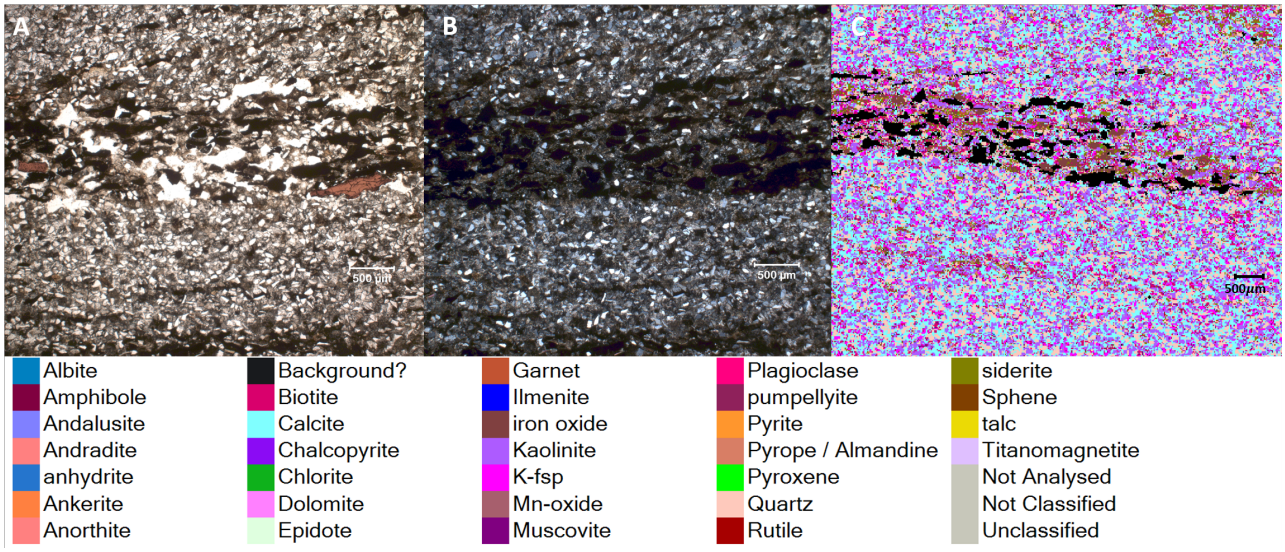


**Figure 5.19:** Pictures of the polished thin section of the fragment MT-PC-10023-1-2. A) PPL, B) XPL, C) automated mineralogy mapping.

**MT-PC-10036 >1/2:**

The thin section consist of a fine-grained brown (ppl and xpl) matrix with some layering. Most of the sample consist of this matrix, but there are a few larger quartz and pyrite grains. In order to decide the mineralogy of the matrix, the results from XRD and AMS is used. These results show that the

fine-grained matrix consists of siderite, mica, kaolinite, quartz and iron oxides. However, the fine-grained texture of the matrix makes the results from the AMS mapping less accurate, due to the grain size being smaller than the step size.

Pyrite is the only ore-forming phase present in the fragment. The pyrite occur as framboidal pyrite shown in figure 5.20 C and D, and as larger euhedral grains within the fine-grained matrix, shown in figure 5.20 A and B.

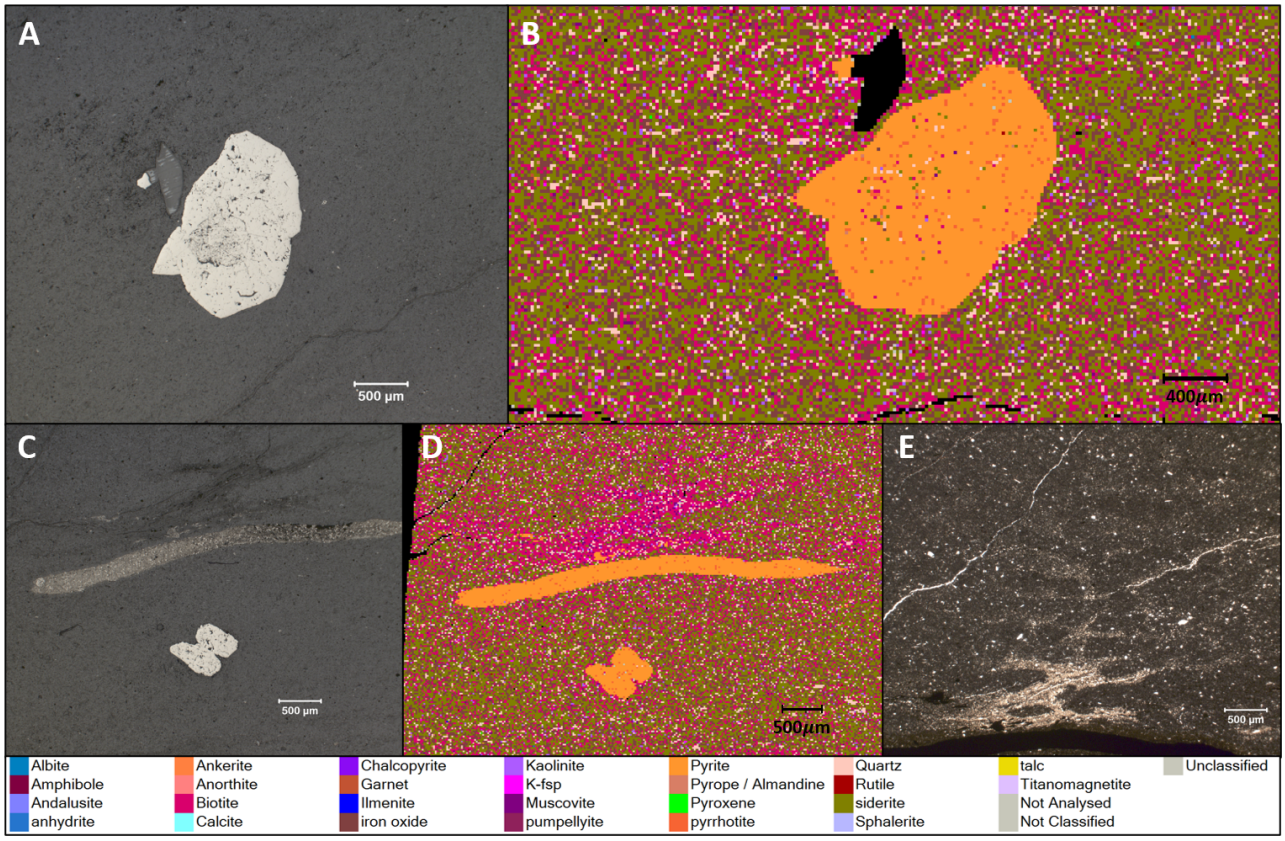


**Figure 5.20:** Picture showing the most interesting features of the thin section from the fragment collected from MT-PC-10036>1/2. A) Reflected light microscopy of pyrite in the fine-grained matrix, B) AMS 20$\mu m$ mapping of the same grain, C) pyrite occuring as framboidal as well as one large euhedral pyrite grain, D) The same image as mapped by AMS, E) The same area in crossed polarised light.

### 5.2.3 AMS

Some of the stub images from the AMS mapping have already been presented in the previous section. The following section presents the modal mineralogy as described by automated mineralogy. The first table, table 5.5, show the modal mineralogy of the two polished blocks from sample LC-SS-10008-1 and LC-SS-10008-2. Table 5.6 show the modal mineralogy of the three polished thin sections from Mohn's Treasure. The mineralogy is presented as weight percents.

**Table 5.5:** Table showing the modal mineralogy from AM analysis of the fragments from Loki's Castle. n.i=not identified

| | **LC-SS-10008-1** | **LC-SS-10008-2** |
|---|---|---|
| | **Wt.%** | **wt.%** |
| *Pyrite* | 7.02 | 0.12 |
| *anhydrite* | 0.01 | 93.62 |
| *Sphalerite* | 0.62 | 0.00 |
| *Amphibole* | 0.00 | 0.05 |
| *Olivine* | 0.02 | 0.00 |
| *Baryte* | 0.02 | 0 |
| *Galena* | 0.00 | n.i |
| *Dolomite* | 0.00 | 0.79 |
| *siderite* | 1.08 | n.i |
| *Quartz* | 5.96 | 0.03 |
| *Iron calcite* | 0.02 | 0.01 |
| *iron oxide* | 16.99 | 0.06 |
| *pyrrhotite* | 64.91 | 0.08 |
| *isocubanite* | 0.93 | 0 |
| *Biotite* | 0.03 | 0 |
| *Chalcopyrite* | 0.91 | 0.02 |
| *talc* | 0.98 | 4.59 |
| *Calcite* | 0.49 | 0.58 |
| *Unclassified area %* | 3.10 | 2.05 |
| *Sum* | 100 | 100 |

**Table 5.6:** Table showing the modal mineralogy from AM analysis of the fragments from Mohn's Treasure

| | **MT-PC-10023-1-2** | **MT-PC-10023-1-1** | **MT-PC-10036>1/2** |
|---|---|---|---|
| | **Wt.%** | **Wt.%** | **Wt.%** |
| *Quartz* | 19.51 | 41.71 | 4.26 |
| *Talc* | 0.01 | 0 | 0.00 |
| *Iron oxide* | 1.73 | 0.01 | 29.79 |
| *Ilmenite* | 0.03 | 0.01 | 0.00 |
| *Pyroxene* | 0.02 | 0 | 0.02 |
| *Chlorite* | 0.0 | n.i | n.i |
| *Pyrrhotite* | n.i | n.i | 0.13 |
| *Pyrite* | 0.00 | 0 | 2.08 |
| *Garnet* | 0.12 | 0 | 0.06 |
| *K-fsp* | 6.71 | 4.57 | 0.19 |
| *Pumpellyite* | 1.28 | 0.02 | 0.01 |
| *Siderite* | 2.95 | 0.73 | 42.28 |
| *Biotite* | 7.72 | 8.38 | 17.72 |
| *Calcite* | 34.16 | 0.39 | 0.00 |
| *Kaolinite* | 20.98 | 1.35 | 1.10 |
| *Muscovite* | 2.05 | 0.75 | 0.63 |
| *Plagioclase* | 0.86 | 22.22 | n.i |
| *Rutile* | 0.18 | 0.04 | 0.10 |
| *Pyrope / Almandine* | 1.16 | 0.31 | 1.61 |
| *Albite* | 0.32 | 19.38 | 0.01 |
| *Anorthite* | 0.13 | 0.11 | 0.00 |
| *Andradite* | 0.02 | 0 | 0 |
| *Unclassified area%* | 2.37 | 0.29 | 0.37 |
| *Sum* | 100 | 100 | 100 |

### 5.2.4 XRF

Full XRF results of the fragments is attached in appendix B. Table 5.7 show the base metal and iron concentrations of the fragments.

**Table 5.7:** Figure showing iron and base metal grades from XRF for the fragment from Loki's castle and Mohn's Treasure.

| | **Cu** | **Pb** | **Zn** | **Fe** |
|---|---|---|---|---|
| | **ppm** | **ppm** | **ppm** | **wt.%** |
| *LC-SAMLE-10007* | 201.1 | 133.7 | 126.2 | 0.30 |
| *LC-SS-10008-1* | 22309.3 | 560.6 | 13939.2 | 23.1 |
| *LC-SS-10008-2* | 1145.6 | 420.3 | 3264.9 | 3.64 |
| *MT-PC-10023-1-1* | -0.1 | 23.5 | 44.3 | 1.34 |
| *MT-PC-10023-1-2* | 12.8 | 11.4 | 37.7 | 2.05 |
| *MT-PC-100361/2* | 32.6 | 12.7 | 72 | 22.80 |

Figure 5.21 show how the base metal grades of the fragments plot in the ternary phase diagram.

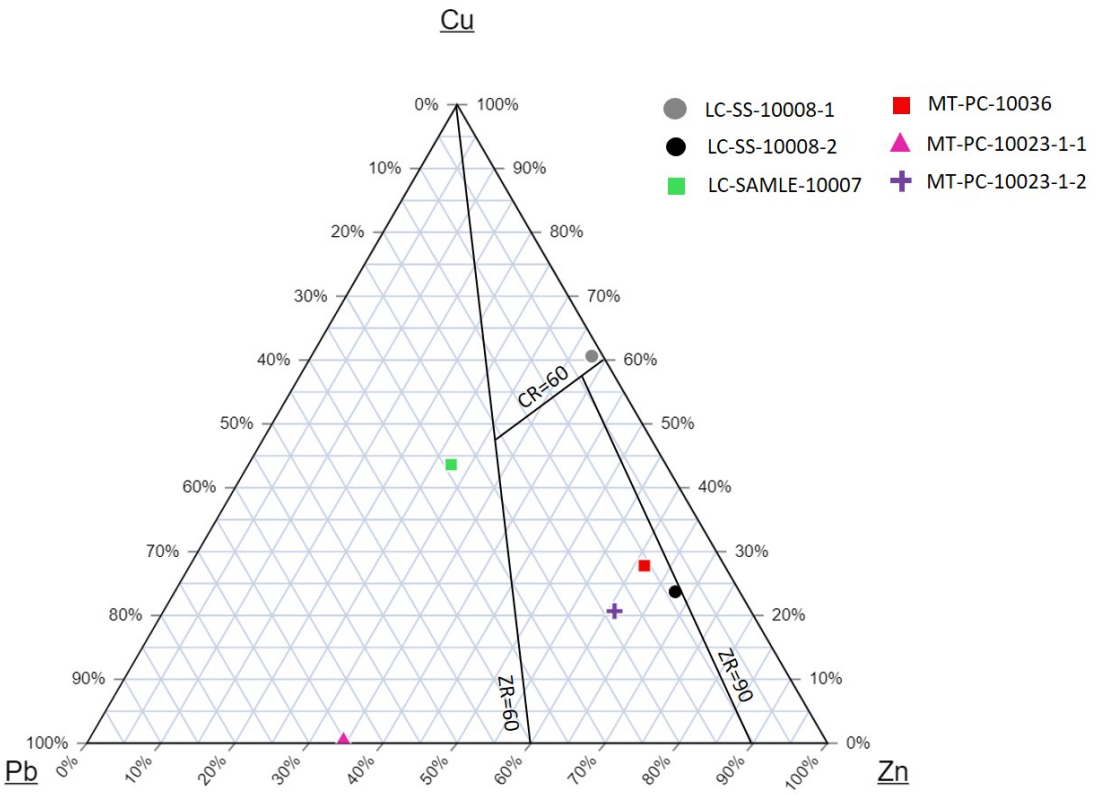


**Figure 5.21:** Base metal ternary plots for Fragments. The granitic sample (MT-PC-10023-1-1) plots along Cu=O.

Chapter 6

# Discussion

The following discussion is based on the results presented in the previous chapter as well as the theory presented in chapter 2 and 3).

The discussion will attempt to answer the objectives described in the project description by determine the origin of the sediments. This will include degree of mixing with lithogenous and biogenous sediment, and estimated hydrothermal component of the sediment samples. By comparing the metal grades with typical grades from VMS deposits a characterisation of the host rock lithology at Loki's Castle can be given. The characterisation will emphasize on the economically valuable elements present, such as Cu, Fe, Zn, Ag and Au, as well as sulphur and iron.

The discussion is split into three parts where the first part discusses the applicability of the XRF methods performed at NTNU, compared to the external accredited analyses. As marine mineral exploration is an emerging industry, these observations will be beneficial for future studies of sediments/samples from similar sites, even though it is not part of the project description.

The second part discusses the results from Loki's Castle. These sediments showed elevated concentrations of base metals and iron, and the focus for the discussion will be on these phases as well as degree of mixing with terrestrial and biogenous material. The classification schemes presented in chapter 3 will also be included and the deposit will be characterised, with respect to sediment and deposit type. A discussion concerning the host rock lithology will also be included, which is based on the metal ratios.

The third part studies the more complex results from Mohn's Treasure. These sediments were thought to include traces of sulfides similar to the dredge brought up by Pedersen et al. (2010b). This was assumed as being an evidence of hydrothermal activity or a mass wasting incidence at Mohn's Treasure. In this study, there were less sulfides than what was expected. However, other hydrothermal alteration products were detected, which might indicate that hydrothermal fluids have played a role in the formation of the sediments at Mohn's Treasure.

## 6.1 Applicability and Quality of the XRF Methods

The following discussion is performed in order to evaluate the quality of the results from the XRF analysis. Some time was spent deciding if the quantitative and semi-quantitative XRF method was applicable for this type of material.

One of the main challenges conerning the XRF analysis occured during melting of the samples in to glass pills. When the melt was poured into the platinum the crucibles, they tend to crack as

they cooled and was in addition extremely difficult to successfully release from the crucibles. As a result, larger parts of the sample was stuck inside the platinum crucible and had to be removed either by remelting or an ultrasonic bath. The cracked samples was unfit for the analysis and had to be remelted. Additional lithium-iodine was added in attempts to avoid cracking. This was successful, however some samples had to be melted up to four times to successfully melt the sample. It is uncertain how this approach has affected the results, but the results have a decreased accuracy due to this treatment.

The challenges concerning cracking and cooling of samples was only was present in the samples from Loki's Castle, and was not the case for the Mohn's Treasure samples. This is probably due to the considerably large differences in composition between the two locations as shown in the XRD analysis presented in figure 5.1. The phases most likely to cause the preparation difficulties for the samples from Loki's Castle are talc, which contain high concentrations of magnesium and iron, and sulfides. If similar samples are to be analysed again, some considerations as to what melting procedure is best suited for the material should be performed. Even though the challenges were solved by adding lithium-iodine, the affect this had on the quality of the results were uncertain. Below follows a discussion concerning the quality of each of the performed XRF methods is presented.

### 6.1.1 Choosing a method

The following discussion is included in order to clarify the challenges concerning the quality of the laboratory analyses performed. Three different methods were used to estimate the chemical content by XRF. The reasons for performing three different methods was done due to uncertainties regarding the preparation procedure explained in section 6.1, above. All three methods were performed both on the fragments as well as the sediment. The methods performed were:

- WROXI: The quantitative method used to estimate the main element concentrations in the samples. This method required ignition of the samples as well as melting into glass pills. Due to uncertainties to how the sample chemistry would react to the ignition and melting, it was decided to perform a semi-quantitative method as well:

- Omnian 37: A semi-quantitative method used to estimate the main elements present in the samples. This method is performed on pressed powder pills and the samples have not been exposed to melting or ignition in advance of the analysis.

- ProTrace: This method quantifies the trace-elements in the samples and uses pressed powder pills for the analysis. This method quantify the base metal concentrations as well as the silver content. Some of the rare earth elements are also quantified by this method.

The best case scenario for the quantification of element concentration, would be to use the quantitative method (WROXI). Due to this method not being calibrated to estimate high concentrations of sulfur, iron, barium and magnesium, there were large uncertainties with the quality of the results. If the concentrations of these elements are too high, new methods should be developed in order to quantify the elements properly. This is another project which is beyond the project description and time-span assigned for this thesis.

Due to the uncertainties described above, it was decided to compare the results from the quantitative method with to ProTrace, Omnian as well as the accredited results from ALS, in order to evaluate the applicability of the methods.

#### 6.1.1.1 Sediment samples

XRF was performed after the XRD and the sediment samples were the first samples to be analysed. From the beginning it was clear that the samples from Loki's castle would be more challenging than the Mohn's Treasure samples, because they were expected to contain higher concentrations of sulfides, copper, baryte and magnesium (as shown by XRD) and generally had a more complex mineralogy. This also lead to some concern regarding the preparation for methods and especially the melting of the glass pills for the quantitative analysis. Sulfide samples are generally challenging to analyse by standard XRF methods that requires melting due to its effect on the melts viscosity and surface tension. Low viscosity and high surface tension lead to the pills easily cracking and some of the samples had to be remelted several times in order to successfully create a glass pill. It is not certain how this treatment of the pills have affected the quality of the results.

One way to initially quality check the results from the XRF analysis was to look at the total sum of the estimated elements. For the main elements the sum should summarise to roughly 100%. The WROXI analysis summarised to approximately 100% for all samples, while the omnian results did not. Here most of the samples summarised to values far below 100, between 70-75%. The exception was sample LC-SAMLE-10007 which summarised to 133.6. In order to compare the omnian method, normalised values will be used for that sample.

The comparison between the different methods is shown in figure 5.14. The figure show the correlation between the WROXI, Omnian with respect to the accredited analyses performed at ALS.The accredited results are thought to be the most accurate estimates, and were used to quality control the results from NTNU.

The figure clearly show how the WROXI method failed to estimate the sulfur concentrations in the samples which was the main concern prior to the analysis. Omnian 37 show better results, especially for sulfur concentrations below 4 wt.%, while for higher concentrations the method underestimates the sulfur concentrations. Sulfur is the only element were the XRD was added to the correlation plots. The XRD show surprisingly good results compared to the WROXI and omnian method. Especially for higher concentrations of sulfur, XRD is more accurate than XRF. However none of the methods are precise enough to be considered quantitaive.

The iron and base metal contents were also evaluated in a similar way as the sulfur concentrations. These correlations are also shown in figure 5.14. The base metal concentrations were also estimated by the ProTrace method, in addition to Omnian, WROXI and ALS, which ere all added to the correlation plots.

For the base metals, WROXI and pro-trace show the best correlation with ALS. Omnian is not a good estimator for base metal concentrations in these samples. The methods are most accurate for lower concentrations of base metals and as the grades increase, the correlations becomes weaker for all of the methods. Copper concentrations are particularly inaccurate for higher grades, and all the methods underestimates the highest concentrations of copper. The base metal estimations generally show relatively good correlation with ALS, and the WROXI method is considered the most accurate as this method show the best correlation for higher concentrations.

Silver concentrations were quite accurately estimated using the pro trace method. For higher concentrations of silver however, the method seem to overestimate the grade.

The observations from the plots in figure **??** as well as the discussion presented above lead to the conclusion that WROXI is the most suitable method to estimate base metal and iron concentrations. Sulfur concentrations are best determined using XRD or omnian 37. However the existing methods should be calibrated or new methods should be developed in order to quantify the elements from such

deposits properly.

#### 6.1.1.2 Fragments

None of the fragment samples were sent to ALS for an accredited analysis. However the observations from the sediments give an indication of what methods is likely the most accurate for these samples as well. I.e WROXI is unreliable for sulfur concentrations, but favorable for estimation of base metals and iron.

## 6.2 Loki's Castle

### 6.2.1 Origin of the Sediments

The origin of the sediments at Loki's Castle can be evaluated through figure 5.1, 5.3, 5.4, 5.5, 5.10, 5.11, 5.12, 5.13 and table 5.2 and, which all present different aspect of the samples geochemical signatures.
Figure 5.1 show the main mineralogy obtain by XRD. Sample LC-SS-10007-1, -2 and -3 all show high concentrations of talc, mica and albite. Sulfides is identified as mostly isocubanite but have a low concentrations in this group. This is likely due to this group being collected at the flank of Loki's Castle (see figure 2.3). Talc is a high-temperature alteration product and is typical for sediments collected from such sites. The high concentrations of talc reflect the high temperature that is present in the fluids circulating at Loki's Castle. Talc has likely formed as hydrothermal fluids react with Mg in the seawater and has precipitated as a result of the sudden temperature change as they reach the surface. Results from AMS suggest that talc has precipitated as a Fe-rich variety due to high Fe concentrations in the fluids. The stub images seen in figure 5.3 A and B show that the talc may contain small inclusions of chalcopyrite and sphalerite, which further strengthens the theory.

The albite present in group 10007 might be a hydrothermal albite formed as an alteration product of primary feldspar. Mica is presumably a Fe-rich mica and have might also has formed as result of high-temperature alteration. However, the albite and mica might also be part of background lithogenic sediment surrounding the area. This theory is substantiated by the XRD results from Mohn's Treasure as they show similar concentrations of these composits. The sediments from Mohn's Treasure are concluded on consisting largely of lithogenic sediment (see discussion in section 6.3.1.1, ) and show similar albite and mica concentrations as the Loki's Castle sediments.

Sample LC-SAMLE-10007 is collected from the same area as the other 10007 samples but show contrast in chemical composition compared to 10007-1, -2 and -3. XRD showed approximately 40% of baryte,which was confirmed by the accredited analysis showing Ba-concentrations of 17% (figure 5.4). Baryte is a common composite of white smokers and the high baryte concentrations are believed to have formed by collapsing white chimneys or as fine-grained particles forming as the white smoke have settled. The fact that baryte-bearing fragments were found in the sample, suggest proximity to a collapsed chimney. It is still likely that precipitation from the white smoke has occurred, and baryte is probably present both as chimney fragments and as plume fall-out. As white smokers usually form at the flanks of hydrothermal mound, the high baryte concentrations in this sample group is consistent with the presented theory.

Sample LC-SS-10008-1 and -2 contain considerably more metallic sulfides which is expected as these samples were collected closer to the centre of the mound and the hydrothermal source. Both pyrrhotite, isocubanite, pyrite and sphalerite are identified by XRD. Pyrrhotite is the most dominating sulfide phase which is estimated to approximately 25 wt.%. Pyrite and sphalerite are both quantified to around 1 wt.%, while isocubanite lie between 6-8 wt.%. The other phases present in these samples are talc, mica, kaolinite, albite and calcite. Mica and albite might represent secondary alteration products of lithogenic sediments by propylitic alteration, or they might be of terrestrial origin (as for the first group). Kaolinite and calcite are most likely litoghenic and biogenous sediment.

The reason for the contrasting compositions in sediments from Loki's Castle is probably a consequence of distance to the hydrothermal source. LC-10008-1,-2 are collected close to the black

smoker chimneys and chimney fragments are likely more frequent. Plume precipitation will also be more dense, as the plume are not as diluted as above the flanks of the mound. The amount of lithogenic and biogenous sediment should thus be negative proportional to the distance from the hydrothermal source. However, calcite is only observed in the samples collected closest to the source. An explanation might be the increased biological activity surrounding hydrothermal chimneys. The sediments are also rich in talc which have not often been described from similar hydrothermal fields. Hodgkinson et al. (2015) described talc dominated hydrothermal systems in 2015 as a new class of hydrothermal fields. Loki's castle is thus one of few sites that have, to this point, been described as talc-dominated.

#### 6.2.1.1 Metalliferous and/or Ore Sediments

Figure 5.5 illustrate the three criteria from section 3.2.1 from Boström et al. (1973a). The plot show all the sediment samples and the Loki's Castle and Mohn's Treasure samples plotted together. In this section only the results from Loki's castle will be discussed, while the results from Mohn's Treasure will be considered in the next part of the discussion. All the samples from Loki's Castle fulfil all three criteria and can with high certainty be characterised as metalliferous. There are however individual differences between the samples and groups within all criteria. The group LC-SS-10007 show lower ratios for all the criteria, which is due to their low Fe-concentrations, and elevated Aluminium content. Manganese is not present in significant amounts in either of the groups, and the ratios are practically independent of this element. Assuming the Mn-concentrations are 0, the (Fe+Mn)/Al-ratio approximately represent the Fe/Al-ratio. As expected, the samples collected closest to the hydrothermal source show the highest Fe/Al-ratios which lie between 30-40. The samples collected from the flank show lower ratios, between 10-20, but still fulfil the criteria. Sample LC-SAMLE-10007 show slightly higher Fe/Al-ratios than the other samples from this group, which likely is due to closer proximity to the white smoker. Generally, the higher Al- and associated lower Fe-grades further away from the hydrothermal source can be explained by fewer chimney fragments and diluted hydrothermal plumes.

Based on these observations the sediments from Loki's Castle can with high certainty be classified as metalliferous. However, in order to characterise the sediments as ore sediments the Fe-concentrations have to be above 30% None of the samples fulfil this criteria, as seen on figure 5.7. This is likely not because of limited access to Fe-rich precipitates, but due to mixing with lithogenic sediment. Loki's castle is significantly closer to the continental shelf than other well know similar hydrothermal deposits, which have caused higher concentrations of terrestrial material.

#### 6.2.1.2 Hydrothermal Component

The findings discussed above all agree with the sediments from Loki's Castle consisting of partly hydrogenous sediment. However, what percentage of the material that should be considered hydrothermal was uncertain. If the hydrothermal component of the sediment was decided, then the degree of mixing between hydrothermal precipitates and lithogenic and biogenous material could be presumed. Table 5.2 show the calculated hydrothermal component, which was based on the scheme presented by Metz et al. (1988). The samples from Loki's castle all show hydrothermal components between 90-96%. Sample LC-SS-10007-1, - 2 and -3 show higher hydrothermal component than LC-SS-10008-1, and -2. This is counter-intuitive as LC-SS-10008-1 and -2 are collected closer to the hydrothermal source and should have been exposed to high density precipitation and plume fall-out as discussed in section 6.2.1 and 6.2.1.1 . The explanation is that these samples contain elevated concentration of calcite (as seen on XRD, figure 5.1) compared to the samples collected from the flank. As discussed earlier, the elevated calcite concentrations might be caused by increased

biological activity near the hydrothermal source, but this theory is uncertain as it is outside the field of study for this thesis.

The Fe-concentrations are still higher towards the centre of the mound, as shown in table 5.3. Since most of the iron is assumed as having a hydrothermal source, this indicates that the calculation of hydrothermal might not be accurate. (As seen in appendix B, figure B.6, the results from Loki's Castle does not plot in a linear pattern.) However, the model presented by Metz et al. (1988) also show the same trend. That for high concentrations of hydrothermal material, the data-set plot as a cluster and create a vertical trend in the plot, rather than a linear correlation. This indicates that for high hydrothermal components the method might not be applicable. Still, the conclusion is that sediments from Loki's Castle have a hydrothermal component between 80-95%, which is also confirmed by the high concentration of hydrothermal phases identified by XRD, and AMS, i.e talc, metallic sulfides and biotite.

#### 6.2.1.3 REE-patterns

The REE-patterns observed within the sediments from Loki's Castle are typical for SMS deposits, and in agreement with the values reported by Snook et al. (2018). All the REE-patterns are shown in figure 5.13 which show that the samples from Loki's castle are extremely depleted, apart from Eu which show a strong positive anomaly. As discussed in chapter 3, a positive Eu-anomaly imply that there has been leaching of Eu from the host rock. In this case the leaching has presumably taken place, as the hydrothermal fluids have been circulating the host rock. The europium likely started to enter the fluids as albitisation commenced and were precipitated along with the other hydrothermal phases as fluids were discharges and temperatures decreased.

There are some differences in REE-patterns between the sample groups as seen on figure 5.9. They generally show the same depleted trend, however the samples furthest away from the hydrothermal source show increased concentrations of all of the elements compared to closer to the source. This likely represent the increasing concentration of terrestrial sediments further away from the source. The REE's might also precipitate closer to the heat source due to decreasing temperatures towards the flanks. Europeum concentrations are however similar in all of the samples, i.e there is a stronger positive anomaly closer to the hydrothermal source. A possible explanation might be that the early precipitates has worked as sinks for europium, causing weaker anomalies further away from the hydrothermal source (as discussed in Dekov et al. (2008)).

### 6.2.2 Base Metal Grades

Base metal grades are presented through figure 5.5, 5.6, 5.7 and 5.8. The base metal grades reported in this study are from the sediments overlying the deposit and does not represent the grades of the actual deposits. Thus the results are not directly comparable to grades of other SMS deposits. However the ratios between the different metals should be similar, which is why the ternary plot is a better way to characterise the deposits, based on the sediments.

The samples show surprisingly high Cu grades, and are in agreements with the grades reported from Loke by Snook et al. (2018). This confirms the fact that degree of mixing with terrestrial sediment is low at this cite. Samples collected close to the hydrothermal chimneys show the highest grades for Cu and Zn and are within the ranges shown in figure 3.4.

Figure 5.8 show that the sediment samples from Loke plot within three different categories as described by Large (1992). Sample LC-SS-10008-1 and -2 have ZR above 90 and CR slightly below 60, which classify them as Zn-Cu type. The sediments collected from the flank plot within the Cu-type and have CR above 60. Sample LC-SAMLE 10007 is different and plots within the class of Zn-Pb-Cu type. This is due to the elevated Pb-grades in this sample, shifting the point towards the centre of the diagram. All the samples plot within different type of deposit which makes it difficult to place the sediments within one category. However, the LC-SS-10008 samples are concluded on being the ones that best represent the deposit, as these samples are the ones with the lowest degree of mixing with terrestrial sediment (as concluded on in the previous section).

Pb grades were expected to be higher in the samples. As mentioned in Baumberger et al. (2016) Loki's castle is assumed as being a sediment influenced hydrothermal system. Since Pb is precipitated at lower temperatures, it is unlikely that the interior of the mound is richer in lead that the samples collected from the flanks. Conclusively, the sediment layers affecting the hydrothermal fluids emitting the black smokers, have not affected the Pb grades in the deposit to a large degree. Pb grades are still somewhat elevated in sample LC-SAMLE-10007 , compared to the other samples (figure 5.10). This is an expected zonation caused by the temperature gradient in an active hydrothermal system.

Au and Ag has lower grades in the sediments than what was reported by Snook et al. (2018), and are more comparable to other SMS deposits. However, Snook et al. (2018) studied fragments collected by grab samples which reflect the hard rock mineralogy of the mound and are most likely a better indicator of the composition of the average grades of the deposit. Au and Ag might have precipitated to early to be part of the hydrothermal plume precipitate which make out large parts of the hydrothermal material in the sediments.

### 6.2.3 Fragments from Loki's Castle

The three fragments collected from Loki's Castle each represent different parts of the hydrothermal system. The fragment from LC-SS-10008-2 represent the anhydrite-rich chimney wall of the black smokers which precipitate as the hot hydrothermal fluids rapidly cool and react with the seawater.
Fragment LC-SS-10008-1 is a metal rich chimney fragment and show a hydrothermal vein which have precipitated metallic sulfides as the fluids have moved through the chimney. The outer parts of the fragment consist of talc and pyrrhotite. Talc is likely the first phase that formed as the hot fluids met the seawater, obtaining Mg as the fluids mixed. Precipitated talc then forms a solid circular surface surrounding the emitting fluids, which allowed for precipitation of metallic sulfides on the surface. Pyrrhotite is the most common sulfide through the fragment, but closer to the center, isocubanite and quartz is more common.

The fragment from LC-SAMLE-10007 consist mostly of baryte similar to the sediment material it was collected with, consisting of mostly white smoker chimney fragments.

The base metal grades from the fragments were also all plotted in the ternary phase diagram, shown in figure 5.21. LC-SS-10008-1 plots within Zn-Pb-Cu field, which is different from the corresponding sediment sample. LC-SS-10008-2 plots at approximate same spot as the corresponding sediment sample, while the LC-SAMLE-10007 is shifted further towards Pb.

### 6.2.4 Classification of the Deposit Based on Sediment Characterisation

To characterise the deposit after the categories presented in section 3.3, figure 3.9 and 5.10 can be compared. Since the samples does not represent the host rock lithology, the base metal grades can only give an indication of what type the deposit belongs within.

As previously discussed, lead was expected to be more enriched in the sediments as consequence of buried sediment layers beneath the mound (Baumberger et al. (2016)). Elevated Pb grades could thus indicate that the deposit might fall within the mafic-siliciclastic group rather than purely mafic. However, the sediments did not show particular enrichment in lead as seen on figure 5.10. It is therefore unlikely that buried sediment layers have impacted the grades of the deposit. The plotted points in the ternary phase diagram plot close to the typical mafic type deposits, and can base on this comparison be characterised as a mafic Zn-Cu deposit.

## 6.3 Mohn's Treasure

### 6.3.1 Origin of the Sediments

As shown by XRD (figure 5.1), the sediments from Mohn's treasure are a typical mix of lithogenous and biogenous sediment. The sediments consist of quartz, calcite, mica, kaolinite, plagioclase and alkali feldspar. This was expected as the site is in relatively close proximity to the continental shelf and thicker layers of terrestrial sediments are expected. Since the site has been concluded on being an extinct field (Lim et al. (2019), Pedersen et al. (2010b)), the deposits have likely been covered gradually with these sediments as they have been eroded from the continental shelf, transported and deposited on the shelves of the ridge.

The XRD results can be compared to the modal mineralogy results from the automated mineralogy. Due to time-restrictions only one of the sediment samples from Mohn's Treasure was mapped by AMS. The sample chosen for mapping was the one that showed the highest concentration of sulfides after XRD and optical microscopy. This was sample MT-PC-100036>1/2 which showed 2.9% pyrite by XRD and also showed anomalous high iron-concentrations by XRF (Figure 5.5 and 5.7). The estimated pyrite by XRD is in good agreement with the modal mineralogy from the automated mineralogy which measured 3.28%. However, there is less agreement between AMS and XRD for the other mineral phases. It was quickly discovered that there was an additional iron oxide phase present which was not identified by XRD. This might indicate that this iron phase is amorphous and perhaps an alteration product.

As seen on the stub images of the $2\mu m$ mapped zone from this sample, the pyrite grain is altered to an iron-oxide phase which appear in the cracks of the particle. As mentioned in chapter 3.1 initially precipitated iron-sulfides may be replaced by iron-hydroxides when the conditions become more oxidising. This agrees with the theory of iron oxides present as an alteration product in the sediments. The high Fe concentrations recorded by XRF is also substantiated with the presence of biotite-mica which elevate the iron-concentration of the sample, which is recognized both by XRD and AMS.

Something which might make the automated mineralogy results less accurate is that grain sizes are too small to be recognised by the $20\mu m$ mapping. As mentioned, higher resolution mapping was performed on parts of the block. This showed more consistent results of the modal mineralogy, but can not be used to describe the mineralogy of the whole sample as the high resolution mapped areas are unrepresentative to the whole block.

XRD showed that chlorite was present in most of the samples collected at Mohn's Treasure. This might be an indicator of hydrothermal activity at the cite, since chlorite is a low temperature hydrothermal alteration product and is commonly associated with sediments related to hydrothermal systems. Chlorite was however not identified in the sediment block investigated by the automated mineralogy. This makes the observation of chlorite by XRD more uncertain. As discussed above the chlorite phase might be too fine-grained and was failed to be identified by the coarse $20\mu m$ AM mapping. The chlorite concentrations are elevated in the samples collected closest to the magnetic anomaly (figure 2.2), which strengthens the possibility that it has formed as result of diffuse or low temperature venting at Mohn's Treasure. One of the fragments collected from Mohn's treasure during the cruise also showed indications of diffuse seapage as explained in Ludvigsen et al. (2016). This sample was also collected from the close to the magnetic anomaly and the push cores, which also strengthens the theory.

#### 6.3.1.1 Metalliferous and/or Ore Sediments

The sediments from Mohn's Treasure were also plotted in figure 5.5, illustrating the criteria for them to be calssified as metalliferous. None of the samples from Mohn's treasure fulfill all three of the criteria illustrated. However, the iron rich sample MT-PC-10036>1/2 show Fe/(Fe+Mn+Al) $> 0.5$ which is one of the criteria described by Boström et al. (1973a). This is due to the elevated iron concentrations in this sample. By definition, the sediments from Mohn's Treasure can not be described as metalliferous.
As illustrated in figure 5.7 none of the Mohn's Treasure samples classify as ore sediments either. Both of these observations were expected due to the degree of mixing with other sediments at this location.

#### 6.3.1.2 Hydrothermal Component

Even though the sediments from Mohn's Treasure does not fulfill the criteria to be characterised as metalliferous, the sediment may still have a smaller hydrothermal component. The hydrothermal components was calculated by the same method as with Loki's Castle and are presented in table 5.3. The hydrothermal component lie between 9 and 28%. In general the samples collected furthest away from the magnetic anomaly (Figure 2.2) show a lower theoretical hydrothermal component than the ones closest to the anomaly. This is in good agreement with the theory of hydrothermal activity close to the northern magnetic anomaly.

Figure 5.11 and 5.12 show the calculated hydrothermal components correlation with iron and chlorite. The correlation between hydrothermal component and iron should be positively linear and without large variations if the iron at Mohn's Treasure are of hydrothermal origin. There is a weak positive correlation between calculated hydrothermal component and iron concentrations in the samples collected at Mohn's Treasure. This is an indication of hydrothermal activity at the site. The correlation is however not as strong as for the data gathered by Metz et al. (1988). This might be due to the sediments at Mohn's Treasure being more diluted compared to the sediments related to the TAG, which might also be the reason for the larger variations Deposition of terrestrial sediments should also be more frequent at Mohn's Treasure than at TAG, due to closer proximity to the continental shelf. It should also be noted that the TAG is an active hydrothermal field, while Mohn's Treasure is considered extinct. The overlying sediments of Mohn's Treasure has thus been diluted over time after the hydrothermal activity decreased. One of the most noticeable observations from figure 5.11 is that the iron rich sample (MT-PC-100036>1/2) plot as an outlier in the data series. I.e the sample contain considerably higher concentrations of iron than what is expected based on the calculated hydrothermal component. There are several possible explanations for this anomaly. It could indicate that the iron observed in the sample is not of hydrothermal origin. However, as observed in the studied block of the sample (figure B.4), the iron-rich phases occur as larger grains compared to the surrounding sediment. It is therefore possible that elevated iron concentration is due to a nugget effect, which have created noise in the data. As observed in figure 5.4 the sulfide grains show larger grains size than their surrounding media, which is what might be the cause of this effect.

The fact that chlorite is present in all of the samples from Mohn's Treasure might suggest that there is some hydrothermal alteration occuring at the site. This might be a result of low-temperature venting as this is a low-temperature alteration product, often observed at flanks of mounds or in association with diffuse venting. The chlorite is thought to have formed either as a consequence of diffuse venting, or as part of late stage hydrothermal activity as the hydrothermal system was cooling. It is difficult to confirm that the chlorite did not form as part of the weathering processes of the sediments prior to deposition on the ridge shelf. In order to consider this, the chlorite concentrations were plotted against the calculated hydrothermal component in order clarify their correlation (Figure 5.12). The

correlation plot show a positive correlation with a gradient of 0.2 and a $R^2$ of 0.68. Because iron is a common constituent in chlorite, the correlation in figure 5.11 and 5.12 show similar trends. The positive correlation gives good indication that chlorite indeed has formed by hydrothermal activity at the site. As discussed later (section 6.3.2), some of the fragments studied also confirms this.

Calcite is only present in the samples collected from the north-eastern site. Initially it was thought that the carbonate compensation depth could have influenced on the calcite concentrations. However none of the sites are below the CCD for the northern Atlantic ocean (approximately 5000m). The differences in calcite concentrations might be due to better conditions for biological activity at the north-eastern site as it is located at shallower depth.

The positive trend in figure 5.11 and 5.12 along with the presence of the hydrothermal alteration products, leads to the conclusion that parts of the sediments at Mohn's Treasure can be considered hydrogenous. However, there is a large degree of mixing with lithogenous and biogenous sediment

#### 6.3.1.3 REE-pattern

The REE signatures from Mohn's Treasure are quit flat, but with a slight enrichment towards the light-REE's. They show similarities with the REE-pattern of the mud-stone surrounding Loki's Castle which was analysed by Snook et al. (2018). They have a small negative europeum anomaly. Even though t is condluded that the sediments at Mohn's treasure have a hydrothermal component, the REE patterns suggest that the alteration products have retained the pattern of the primary sediment.

### 6.3.2 Fragments from Mohn's Treasure

The fragments from Mohn's Treasure showed quite different compositions from each other, and can be evaluated from figure 5.15, 5.16, 5.17, 5.19 5.18, 5.20. Modal mineralogy results from AMS are also presented in table 5.6. Full montages of the thin sections can be found in appendix B, figure B.7, B.8, B.9.

One of the fragments, MT-PC-100023-1-1, show a granitic compositon and texture. This was obvious from the XRD as well as the observations from microscopy and AMS. The section contains approximately 42% quartz, 5% alkali-feldspar, 40% plagioclase feldspar 10% mica (mainly biotite) an d 1% kaolinite. The texture is also crystalline with large grain sizes, which lead to the conclusion of this being a granitic fragment. The most likely origin for this fragment is either from glacial deposition or from a transport ship.

Fragment MT-PC-10023-1-2 show a different composition. The fragment contain fine-grained particles consisting of quartz, calcite, kaolinite, mica and alkali-feldspar. This fragment does not contain any sulfides or elevated iron-concentrations. There are no phases indicating hydrothermal activity neither. This fragment is collected from the North-eastern side of the magnetic anomaly and the lack of indication of hydrothermal activity is expected from this location.

In fragment MT-PC-10036>1/2 there is a quite different mineralogy than the two previously described fragments from Mohn's Treasure. The fragment is collected from push core MT-PC-10036>1/2 which is located close to the magnetic anomaly. Hydrothermal phases were thus expected to be present in this fragment

This fragment consist of siderite, mica, quartz and pyrite. There is also another iron oxide or hydroxide present. The high iron contents in the fragment is confirmed by XRF which reported 23% iron. Larger grains of pyrite is also present in the fragment. The pyrite occur as framobidal pyrite and as large euhedral grains. Framboidal pyrite indicates that there has been an alteration of organic matter during reducing conditions at the site (Lin et al. (2020)). The large quantity of pyrite and siderite makes it likely that the rock has been exposed to iron rich fluids, giving the fragment its distinct mineralogy.

The fragment collected from sample MT-PC-10036>1/2 showed *framboidal pyrite* when analysed by automated mineralogy and optical microscopy (illustrated in figure 5.20 C and D). This indicates an alteration of organic matter during reducing conditions. The sample also showed euhedral pyrite. Pyrite occurring in such ways indicates a formation in open space, rather than an alteration of other phases. One of these euhedral pyrite grains is also directly correlated with a narrow quartz vein which might imply formation by hydrothermal fluids propagating the rock.

Chapter 7

# Conclusion

The aim of this thesis have been to characterise the sediments collected at two possible marine mineral deposits located on the extended Norwegian continental shelf. One active hydrothermal field, Loki's Castle, and one extinct field, Mohn's Treasure.

The characterisation has focused on the origin of the sediments, traces of hydrothermal activity and on mixing with other types of marine sediment. By describing the physical and chemical properties of the sediments they could be characterised and their origin could be conclusively proven.

The conclusion below summarises the main findings from the presented results and discussion, as well as suggestions for future work.

Based on previous research from the two sites, considerable differences in composition between the sediments were expected (e.g. Snook et al. (2018), Ludvigsen et al. (2016), Lim et al. (2019), Bruvoll et al. (2009), Pedersen et al. (2010a), Pedersen et al. (2010b), Ellefmo et al. (2019)). This hypothesis was confirmed through the different laboratory methods executed as part of this thesis (i.e. XRD, XRF, optical microscopy, AMS and the accredited analysis performed at ALS). The different laboratory methods generally agreed with each other which strengthened the credibility of the results.

While the sediments from Loki's Castle showed high abundance of hydrothermal phases, including Fe-rich talc and metallic-sulfides, sediments from Mohn's Treasure did not show the presence of such compounds. Furthermore, the sediments from Loki's Castle contained considerably more iron than the samples from Mohn's Treasure. This is due to the field still being hydrothermally active. Both the sediments from Loki's Castle and Mohn's Treasure was concluded on consisting of a mix between hydrogenous sediment and lithogenous/biogenous sediment. This lead to the need for a method which could estimate the amount of hydrothermal material in the samples, in order to define the degree of mixing with other sediments. The method proposed by Metz et al. (1988) was used for this purpose.

The calculated hydrothermal component agreed with the assumptions based on the initial observations. Sediment from Loki's Castle showed hydrothermal components close to 100%, while the Mohn's Treasure sediments were between 9-28%. The method is concluded on being inconclusive for Loki's castle as it did not show a positive correlation with the iron-concentrations. This is likely due to the hydrothermal components being too high. At Mohn's Treasure the results were promising as there was a positive linear correlation between iron-concentrations and calculated hydrothermal component. There were, however, large variations in the dataset, and the results are inconclusive due to the limited number of samples.

In order to consider whether the chlorite at Mohn's treasure had formed as result of increased hydrothermal activity, the scheme proposed by Metz et al. (1988) was modified to show the correlation

between theoretical hydrothermal component and chlorite. The modified plot show similar trends to the one showing iron correlations. This indicates that the chlorite found in the samples is iron rich, and have been created as consequence of increased hydrothermal activity at the site.

The push-cores collected at Mohn's Treasure were collected from two different sites, as shown in chapter 2 figure 2.2. The samples collected closest to the magnetic anomaly are the ones with highest chlorite and iron concentrations. This supports the conclusion of chlorite being formed as result of hydrothermal activity. Fragments containing siderite and pyrite were also found at the site with magnetic anomaly. This further strengthens the theory that the sediments have been affected by hydothermal activity in the area.

Based on the description of the material collected by the dredge-track by Pedersen et al. (2010b), the amount of metallic sulfides was expected to be higher at Mohn's Treasure. The push-cores collected closest to the dredge line and the magnetic anomaly was expected to contain higher concentrations of sulfides than what was discovered. Since the sediments are collected close to a hydrothermal field, they should show metalliferous characteristics, however they fail to fulfill the criteria to be considered metalliferous (figure 5.5). This is likely due to the rapid deposition of terrestrial material above the site due to its proximity to the continental shelf. A mass wasting-event might also have occurred at the site (as suggested by Pedersen et al. (2010b), and discussed in Lim et al. (2019)), which covered the hydrothermal source and associated sediments.

The sediments from Loki's Castle consist of mostly hydrogenous material with a smaller lithogenic and biogenous input. They are of hydrothermal origin and are defined as *hydrogenous metalliferous sediments*. However, the iron concentrations are not high enough for them to be considered *ore sediments*.

The samples collected closest to the hydrothermal source show the highest concentrations of iron and of metallic sulfides, such as chalcopyrite, pyrrhotite, and pyrite.

Pb grades were expected to be elevated in the sediments due to the presence of buried sediment layers below Loki's Castle, which would allow for leaching of lead from feldspar as the hydrothermal fluids percolated the sediment layers (as discussed in Bruvoll et al. (2009)). As Pb-grades are not elevated in the sediments it is unlikely that the deposit is rich in lead as this element precipitate at low temperatures. However, the fact that pyrrhotite is one of the more common sulfides at the site, argues for the opposite as this phase may form as result of reactions with calcite (Herzig and Hannington (1995)). The conclusion is that Loki's castle likely is sediment influenced, but not strong enough to affect the Pb-grades of the deposit. Based on the base metal grades, the deposits is thus characterised as a *mafic-hosted deposit* Cu-Zn deposit.

Another characteristic feature of the sediments collected at Loki's castle is the high concentrations of talc. Loki's Castle is thus also described as *talc-dominated*. Talc has at Loki's Castle played the same role often seen by anhydrite in other similar deposits. This is illustrated in figure 5.16, were talc form the outer wall of the chimney fragment. However, more chimney fragments should be studied in order to further confirm this observation.

The findings of this thesis have contributed with knowledge and research to two of the promising deposits for marine mineral exploitation on the extended Norwegian contintental shelf. The findings gives insight into the physical properties of sediments related to hydrothermal mineral deposits forming on the ultra-slow arctic mid ocean ridge. The close proximity to the continental shelf is unique for these deposits, and the findings of this study contributes to a better understanding of sediments

related to such deposits.

## 7.1 Suggestions for Future Work

Due to time limitations, the automated mineralogy was not executed in high enough resolution to map all the mineral phases in detail. A more detailed mapping of the polished blocks from Mohn's Treasure and Loki's Castle would describe the mineralogy more accurately.
The gravity core which was collected from Mohn's Treasure on the cruise has not yet been studied. A comparison of the observations from this study with findings from the gravity core will be beneficial to evaluate the vertical differences of the sediments at Mohn's Treasure. Higher temperature alteration products might be present deeper down in the sediment, which will give an increased understanding of the history of the hydrothermal activity that has occurred at the site.

# Bibliography


Alt, J.C., 1995. Subseafloor processes in mid-ocean ridge hydrothermal systems. GEOPHYSICAL MONOGRAPH-AMERICAN GEOPHYSICAL UNION 91, 85–85.

Bach, W., Jöns, N., Klein, F., 2013. Metasomatism Within the Ocean Crust. Springer Berlin Heidelberg, Berlin, Heidelberg. URL: https://doi.org/10.1007/978-3-642-28394-9_8.

Barrie, C.T., Hannington, M.D., 1997. Classification of Volcanic-Associated Massive Sulfide Deposits Based on Host-Rock Composition, in: Volcanic Associated Massive Sulfide Deposits: Processes and Examples in Modern and Ancient Settings. Society of Economic Geologists. URL: https://doi.org/10.5382/Rev.08.01.

Baumberger, T., Früh-Green, G.L., Thorseth, I.H., Lilley, M.D., Hamelin, C., Bernasconi, S.M., Okland, I.E., Pedersen, R.B., 2016. Fluid composition of the sediment-influenced loki's castle vent field at the ultra-slow spreading arctic mid-ocean ridge. Geochimica et Cosmochimica Acta 187, 156–178.

Boström, K., Arquharson, B.F., Eyl, W., 1972. Submarine hot springs as a source of active ridge sediments. Chemical Geology 10, 189–203.

Boström, K., Joensuu, O., Moore, C., Boström, B., Dalziel, M., Horowitz, A., 1973a. Geochemistry of barium in pelagic sediments. Lithos 6, 159–174.

Boström, K., Kraemer, T., Gartner, S., 1973b. Provenance and accumulation rates of opaline silica, al, ti, fe, mn, cu, ni and co in pacific pelagic sediments. Chemical Geology 11, 123–148.

Boström, K., Peterson, M., 1969. The origin of aluminum-poor ferromanganoan sediments in areas of high heat flow on the east pacific rise. Marine Geology 7, 427–447. URL: https://www.sciencedirect.com/science/article/pii/0025322769900164, doi:https://doi.org/10.1016/0025-3227(69)90016-4.

Bruvoll, V., Breivik, A.J., Mjelde, R., Pedersen, R.B., 2009. Burial of the mohn-knipovich seafloor spreading ridge by the bear island fan: Time constraints on tectonic evolution from seismic stratigraphy. Tectonics 28. URL: https://agupubs.onlinelibrary.wiley.com/doi/abs/10.1029/2008TC002396.

Buatier, M.D., Früh-Green, G.L., Karpoff, A.M., 1995. Mechanisms of mg-phyllosilicate formation in a hydrothermal system at a sedimented ridge (middle valley, juan de fuca). Contributions to Mineralogy and Petrology 122, 134–151.

Cherkashov, G., 2017. Seafloor massive sulfide deposits: Distribution and prospecting, in: Deep-Sea Mining. Springer, pp. 143–164.

Dekov, V., Cuadros, J., Shanks, W., Koski, R., 2008. Deposition of talc — kerolite–smectite — smectite at seafloor hydrothermal vent fields: Evidence from mineralogical, geochemical and oxygen isotope studies. Chemical Geology 247, 171–194. doi:10.1016/j.chemgeo.2007.10.022.

Dissanayake, A.L., Yapa, P.D., Nakata, K., 2014. Modelling of hydrothermal vent plumes to assess the mineral particle distribution. Journal of Hydraulic Research 52, 49–66. URL: https://doi.org/10.1080/00221686.2013.854845.

Ellefmo, S.L., Søreide, F., Cherkashov, G., Juliani, C., Panthi, K.K., Petukhov, S., Poroshina, I., Sinding-Larsen, R., Snook, B., 2019. Quantifying the unknown: Marine mineral resource potential on the norwegian extended continental shelf .

Franklin, J.M., Gibson, H.L., Jonasson, I.R., Galley, A.G., 2005. Volcanogenic Massive Sulfide Deposits, in: One Hundredth Anniversary Volume. Society of Economic Geologists. URL: https://doi.org/10.5382/AV100.17, doi:10.5382/AV100.17.

Galley, A.G., Hannington, M.D., Jonasson, I., 2007. Volcanogenic massive sulphide deposits. Geological Association of Canada, Mineral Deposits Division , 141–161.

German, C., Von Damm, K., 2006. Hydrothermal processes. Treatise on geochemistry 6, 181–222.

Gurvich, E.G., 2006. Metalliferous sediments of the world ocean: fundamental theory of deep-sea hydrothermal sedimentation. Springer.

Herzig, P.M., Hannington, M.D., 1995. Polymetallic massive sulfides at the modern seafloor a review. Ore Geology Reviews 10, 95–115.

Hodgkinson, M.R., Webber, A.P., Roberts, S., Mills, R.A., Connelly, D.P., Murton, B.J., 2015. Talc-dominated seafloor deposits reveal a new class of hydrothermal system. Nature communications 6, 1–11.

Hyllseth, A., 2020. Initial identification of main mienralogical phases present in sediments associated with seafloor massive sulfide deposits on the arctic mid-ocean ridge. Chemical Geology .

Janecky, D., Seyfried, W., 1984. Formation of massive sulfide deposits on oceanic ridge crests: Incremental reaction models for mixing between hydrothermal solutions and seawater. Geochimica et Cosmochimica Acta 48, 2723–2738. URL: https://www.sciencedirect.com/science/article/pii/0016703784903193.

Krasnov, S., Stepanova, T., Stepanov, M., 1994. Chemical composition and formation of a massive sulfide deposit, middle valley, northern juan de fuca ridge (site 856), in: Proceedings of the Ocean Drilling Program, scientific results: College Station, Texas (Ocean Drilling Program), pp. 353–372.

Large, R.R., 1992. Australian volcanic-hosted massive sulfide deposits; features, styles, and genetic models. Economic Geology 87, 471–510. URL: https://doi.org/10.2113/gsecongeo.87.3.471, doi:10.2113/gsecongeo.87.3.471.

Lim, A., Brönner, M., Johansen, S.E., Dumais, M.A., 2019. Hydrothermal activity at the ultraslow-spreading mohns ridge: New insights from near-seafloor magnetics. Geochemistry, Geophysics, Geosystems 20, 5691–5709.

Lin, C.Y., Turchyn, A.V., Krylov, A., Antler, G., 2020. The microbially driven formation of siderite in salt marsh sediments. Geobiology 18, 207–224. URL: https://onlinelibrary.wiley.com/doi/abs/10.1111/gbi.12371.

Lisitizin, A., Bogdanov, Y., Mudmaa, I., Serova, W., Zverinskaya, I., Lebedev, A., Lukashin, V., Gordeev, V., 1976. Metalliferous sediments and their genesis. Geological and Geophysical Research in the Southeast Pacific , 289–379.

Ludvigsen, M., Aasly, K., Ellefmo, S.L., Hilário, A., Ramirez-Llodra, E., Søreide, F.X., Falcon-Suarez, I., Juliani, C.J., Kieswetter, A., Lim, A., et al., 2016. Marmine cruise report-arctic mid-ocean ridge 15.08. 2016-05.09. 2016 .

Lydon, J.W., 1984. Ore deposit models - 8. volcanogenic massive sulphide deposits part i: A descriptive model. Geoscience Canada 11. URL: https://journals.lib.unb.ca/index.php/GC/article/view/3396.

Metz, S., Trefry, J.H., Nelsen, T.A., 1988. History and geochemistry of a metalliferous sediment core from the mid-atlantic ridge at 26°n. Geochimica et Cosmochimica Acta 52, 2369 – 2378. URL: http://www.sciencedirect.com/science/article/pii/0016703788902943.

Pedersen, R.B., Rapp, H.T., Thorseth, I.H., Lilley, M.D., Barriga, F.J., Baumberger, T., Flesland, K., Fonseca, R., Früh-Green, G.L., Jorgensen, S.L., 2010a. Discovery of a black smoker vent field and vent fauna at the arctic mid-ocean ridge. Nature Communications 1, 1–6.

Pedersen, R.B., Thorseth, I.H., Nygård, T.E., Lilley, M.D., Kelley, D.S., 2010b. Hydrothermal Activity at the Arctic Mid-Ocean Ridges. Geophysical Monograph Series 188, 67–89.

Piercey, S.J., 2011. The setting, style, and role of magmatism in the formation of volcanogenic massive sulfide deposits. Mineralium Deposita 46, 449–471.

Rafferty, J.P., 2009. Encyclopaedia britannica; biogenic ooze. URL: https://www.britannica.com/science/biogenic-ooze.

Snook, B., Drivenes, K., Rollinson, G.K., Aasly, K., 2018. Characterisation of mineralised material from the loki's castle hydrothermal vent on the mohn's ridge. Minerals 8, 576.

Tivey, M.K., 2007. Generation of seafloor hydrothermal vent fluids and associated mineral deposits. Oceanography 20, 50–65.

Trujillo, A.P., Thurman, H.V., 2014. Essentials of Oceanography. 11 ed., Pearson Education Limited, Boston.

Whitney, D.L., Evans, B.W., 2010. Abbreviations for names of rock-forming minerals. American Mineralogist 95, 185–187. URL: https://doi.org/10.2138/am.2010.3371.

Willis, J., 2010. Xrf sample preparation. glass beads by borate fusion. Almelo, Netherlands: PANalytical BV .

Winter, J.D., 2009. Principles of igneous and metamorphic petrology.

Yıldırım, N., Dönmez, C., Kang, J., Lee, I., Pirajno, F., Yıldırım, E., Günay, K., Seo, J.H., Farquhar, J., Chang, S.W., 2016. A magnetite-rich cyprus-type vms deposit in ortaklar: A unique vms style in the tethyan metallogenic belt, gaziantep, turkey. Ore Geology Reviews 79, 425–442.

Appendix A

# Appendix

## A.1 Theory from the Specialization Project

The following section is theory copied from the literature study that was part of the specialization project. All the theory presented in the literature study was not relevant to include in the master thesis, but some of the definitions and basic theory is referred to throughout the thesis and is thus put in the appendix.

### A.1.1 Hydrothermal Deposits at Mid-Ocean Ridges

The ability for aqueous solutions to effectively scavenge and transport economically important elements through the earth's crust, is one of the most important ore-forming processes. Deposits resulting from these circulating hydrothermal fluids, are known as a hydrothermal mineral deposits (Robb(2005)). Hydrothermal aqueous solutions can be formed through a number of processes, and includes everything from magmatic-hydrothermal fluids to meteoric water infiltration and sea-water diffusion. In other words, the hydrothermal fluids can originate from inside the rock mass, and/or from outside the rock mass. The host rock in which the hydrothermal fluids circulated through also play an important role in how extensive the hydrothermal alteration will be. Different factors affecting the hydrothermal alteration in a rock mass is e.g the chemical composition (fluids and rock mass), permeability and temperature gradient. If there is a pressure or a temperature gradient within the rock mass, a convection system may develop. This convection system will continue to scavenge the host rock for soluble elements.

At Mid-Ocean Ridges there are special circumstances that allow for extensive alteration as well as convection of fluids and phase separation. This includes, high permeability due to induced fracturing as a consequence of low horizontal stress and an elevated geothermal gradient(Bach et al. (2013)). The hydrothermal vents associated with Mid-Ocean Ridges often show an acidic character, and contain higher concentrations of elements such as copper, iron and zinc. Compared to the seawater,the venting fluids have lower concentrations of sodium, chloride, calcium and magnesium as well as a lower pH (Tivey (2007)). The venting fluids at the seafloor was thought to originate from the seawater, meaning that there had been an interaction between the sea-water and the crust leading to these changes of composition.

The speed of the spreading ridge largely effect whether the metasomatic processes will have a magmatic influence or if tectonic faulting will control the processes. In a fast spreading ridge, the magmatic heat budget is large and magmatic diking control the hydrothermal circulation of the sea-

water (Alt (1995)). At slower spreading ridges the heat budget is smaller, making the deformation more brittle which makes faulting more common. The faults created at these tectonic settings are large and long-lived, making them stable passages for seawater (Bach et al. (2013)).Studies have also indicated that on slow-spreading ridges the locations of the faults may control the location of hydrothermal vents and related SMS-deposits as the up flowing fluids will be focused along the fault zones (Alt (1995)). Faulting is shown to be common also at the Mohns Ridge, which is thought to have played an important role in the alteration of the crust in this area (Lim et al. (2019)).The Mohn's ridge is considered and ultra-slow spreading ridge, and recent studies have shown that these tectonic environments are often characterized by separate volcanic segments with avolcanic sections between them (Bach et al. (2013)).

The induced convection system that may occur at mid-ocean-ridges can be separated into three zones according to Alt (1995):

1. Recharge zone: The zone where water penetrates downwards into the crust, reacting with the host rock as it gets heated and pressurised.

2. Reaction/root zone: When the fluids have reached high temperatures (approx. 350°C) the fluids acquire their final chemical signature. This usually occurs at the bottom of the sheeted dike complex, or right above the heat source.

3. Discharge/up-flow zone: The fluids experience increased buoyancy due to them being heated. This results in them rising upwards from the heat source until they reach the seafloor. Here they may be expelled through chimney vents.

The location of these zones is illustrated in figure **??**.

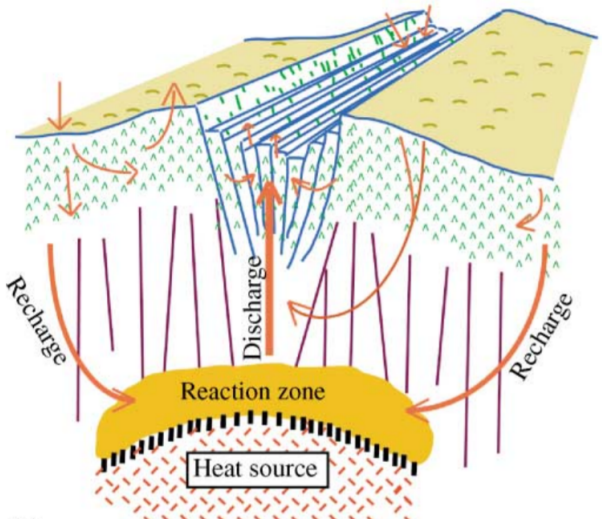


**Figure A.1:** Figure illustrating the fluid circulating system at a mid-ocean ridge, were seawater enters the crust through recharge zones, before they reach high temperature reaction zones, and are rising up through a discharge zone. Figure is from German and Von Damm (2006), which is drawn from Alt (1995)

The upper layer processes include oxidation and alkali fixation in the upper basaltic layer. These processes involves the basaltic crust, including olivine and plagioclase being altered by *oxidation* to ferric micas and smectites, Fe-rich oxyhydroxides and Mg-rich smectite. In this alteration process alkali metals, such as K, Rb and Cs, B and $H_2O$ is transferred from the sea-water and into the mineral assemblage. Elements such as Si and S is transferred from the minerals and into the fluid (Tivey

(2007)).

Oxidation of the top layer only affects the uppermost mineral assemblages. As fluids penetrate deeper, oxidation and circulation gets more restricted and the fluids become more anoxic. The seawater is rich in Mg compared to other fluids (metamorphic or meteoric, etc.) and has a high pH (around 8) (Bach et al. (2013). Because seawater is already saturated with Mg, precipitation in the ocean crust as the fluids penetrate deeper and gets heated, is common. This is observed by the abundance of clay minerals which suggest the precipitation of Mg-silicate, in form of e.g Mg-rich smectite or chlorite (Alt (1995)). The precipitaiton of these clays start at temperatures above 150°C, which usually occurs at depths of 300-450m (Alt (1995)). The removal of Mg can be shown by the reaction below were Albite-anorthite in basalt reacts with water and Mg, resulting in the formation of Mg-chlorite, and a release of $H^+$-ions resulting in a lower pH in the fluids (Tivey (2007)).

$$\underset{Albite-Anorthite}{4(NaSi)_{0.5}(CaAl)_{0.5}AlSi_2O_8} + 15Mg^{2+} + 24H_2O \Rightarrow \underset{Chlorite}{3Mg_5Al_2Si_3O_{10}(OH)_8} + SiO_2 + 2Na^+ + 2Ca^{2+} + 24H^+$$

g is not the only element that is fixated in the upper crust. Ca is also removed from the seawater as a consequence of the precipitation of anhydrite($CaSO_4$), which occurs when the temperature exceeds 150°C. If the fluids have been added Ca from albitization of the basalt, then temperatures for anhydrite precipitation may be even lower. During precipitation of Ca, about 1/3 of the sulfate is also precipitated from the water. With further penetration, Ca-contents are increased in the fluids due to increased albitization of the rock as illustrated in eq. A.1.

$$\underset{Anorthite}{CaAl_2Si_2O_8} + 2Na^+ 4SiO_2(aq) \Rightarrow \underset{Albite}{2NaAlSi_3O_8} + 2Ca^{2+} \tag{A.1}$$

When the fluids reach the upper dike system (fig**??**), temperatures range between approximately 300-450°C, leading to formation of lower greenschist facies minerals. This involves alteration of the basalt, were albite replaces plagioclase(albitization) and actinolite replaces olivine and pyroxene.

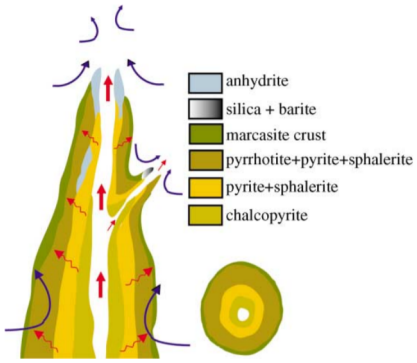


**Figure A.2:** Figure showing the mineralizations within a black-smoker chimney From German and Von Damm (2006)

A proposed structure of mineralizations occuring within a vent chimney is shown in figure A.2. When the hot upwelling hydrothermal fluids meet the cold seawater and mix, this leads to a heat transfer between the hydrothermal fluids and the seawater as well as mixing between them. This allows for $Ca^{2+}$and $SO_4^{2-}$ to precipitates as anhydrite($CaSO_4$) forming a mineralized circular wall around the channelled fluids (German and Von Damm (2006)). This ring then creates a barrier between the seawater and fluids, making extensive mixing between them more difficult and precipitation of anhydrite ceases. The mixing of seawater and cooling of hydrothermal fluids also trigger the precipitation of metal-sulfides and -oxides, which might precipitate onto the anhydrite wall surrounding

the fluid flow, or directly into the plume, giving the chimney its characteristic black smoke(German and Von Damm (2006)). These reactions leads to a build-up of mineralized material surrounding the fluid flow, resulting in the formation of chimney vents. As seen on figureA.2, there is a zonation pattern from the inner parts of the chimney and outwards, which is similar to the pattern found within the mound. This zonation pattern form as the chimney walls evolve, and generally Cu-phases tend to form towards the interior of the chimney and Zn-phases form towards the exterior of the walls, while Fe-phases form all across the chimney zonation. The causes of this zonation pattern is the large temperature gradient as well as a chemical gradient which causes mass diffusion(German and Von Damm (2006)). This results in a chimney-core consisting of chalcopyrite, and sphalerite forming in outer layers, while pyrite and pyrrhotite form in all the layers (German and Von Damm (2006)).

Appendix B

# Appendix

## B.1 Additional Results

### B.1.1 XRD

**Table B.1:** XRD analysis of the samples from Loki's Castle, showing wt.% of the main crystalline phases observed. Mineral abbreviations from Whitney and Evans (2010) and N.I=Not identified.

| | Tlc | Mica | Alb | Cal | Kln | Qz | Iso | Po | Brt | Sp | Py |
|---|---|---|---|---|---|---|---|---|---|---|---|
| Unit | % | % | % | % | % | % | % | % | % | % | % |
| LC-SS-10007-1 | 60.2 | 19.9 | 16.7 | N.I | N.I | 1.5 | 1.7 | N.I | N.I | N.I | N.I |
| LC-SS-10007-2 | 59.2 | 21.3 | 16.4 | N.I | N.I | <1 | 3.0 | N.I | N.I | N.I | N.I |
| LC-SS-10007-3 | 57.93 | 23.8 | 15.3 | N.I | N.I | <1 | 2.8 | N.I | N.I | N.I | N.I |
| LC-samle-10007 | 33.6 | 14.0 | 6.7 | N.I | N.I | N.I | 2.0 | N.I | 43.7 | N.I | N.I |
| LC-SS-10008-1 | 35.2 | 12.1 | 6.9 | 4.6 | 8.1 | <1 | 5.6 | 25.3 | N.I | 1.3 | N.I |
| LC-SS-10008-2 | 31.3 | 15.0 | 5.5 | 5.1 | 7.6 | N.I | 8.0 | 24.8 | N.I | 1.9 | <1 |

**Table B.2:** XRD result from Mohn Treasure area, showing wt.% of the main crystalline phases observed. Abbreviations after Whitney and Evans (2010), and N.I=Not identified.

| | Qz | Cal | Mica | Alb | Afs | Kln | Amp | Chl | Dol | Hl | Py | Sd |
|---|---|---|---|---|---|---|---|---|---|---|---|---|
| Unit | % | % | % | % | % | % | % | % | % | % | % | % |
| MT-SS-10023-1 | 47.3 | N.I | 18.1 | 16.3 | 5.1 | 8.4 | N.I | 4.8 | N.I | N.I | N.I | N.I |
| MT-PC-10028-1 | 34.3 | 31.0 | 13.0 | 9.8 | 5.4 | 2.0 | <1 | 3.4 | <1 | N.I | N.I | N.I |
| MT-PC-10029 <5 | 25.1 | 49.6 | 8.3 | 8.8 | 3.9 | 1.3 | <1 | 2.2 | <1 | <1 | N.I | N.I |
| MT-PC-10029 >5 | 34.1 | 30.0 | 11.8 | 11.1 | 5.4 | 1.7 | 1.1 | 3.0 | <1 | 1.7 | N.I | N.I |
| MT-PC-10031 <5 | 21.8 | 61.5 | 4.9 | 6.8 | 2.5 | <1 | <1 | 1.25 | <1 | <1 | N.I | <1 |
| MT-PC-10031 >5 | 47.8 | 14.6 | 12.3 | 13.9 | 6.4 | N.I | 1.2 | 3.2 | <1 | <1 | N.I | N.I |
| MT-PC-10033 <1/2 | 41.0 | 8.1 | 16.4 | 15.0 | 8.6 | 2.7 | 1.8 | 5.2 | 1.0 | <1 | N.I | N.I |
| MT-PC-10033 >1/2 | 30.8 | 30.3 | 14.3 | 11.3 | 5.4 | 2.1 | <1 | 4.6 | <1 | <1 | N.I | N.I |
| MT-PC-10035 <1/2 | 48.1 | N.I | 16.0 | 15.8 | 6.9 | 6.5 | <1 | 5.0 | <1 | <1 | N.I | N.I |
| MT-PC-10035 >1/2 | 46.1 | 2.4 | 17.0 | 15.7 | 6.7 | 6.0 | <1 | 5.1 | <1 | <1 | N.I | N.I |
| MT-PC-10036 >1/2 | 36.22 | <1 | 26.4 | 1.6 | 3.4 | 17.2 | N.I | 6.0 | N.I | <1 | 3.3 | N.I |
| MT-PC-10037 <1/2 | 49.7 | N.I | 18.1 | 13.8 | 5.3 | 8.0 | N.I | 5.2 | N.I | <1 | N.I | N.I |
| MT-PC-10037 >1/2 | 47.4 | 1.3 | 18.5 | 14.7 | 5.1 | 6.3 | 1.0 | 5.0 | <1 | <1 | <1 | N.I |

## B.1.2 XRF

**Table B.3:** The results from the quantitative WROXI method. Samples from Loki's Castle

| Sample nr. | | LC-SS-10007-1 | LC-SS-10007-2 | LC-SS-10007-3 | LC-Samle-10007 | LC-SS-10008-1 | LC-SS-10008-2 |
|---|---|---|---|---|---|---|---|
| *K2O* | (%) | 0.19 | 0.16 | 0.13 | 0.10 | 0.09 | 0.09 |
| *MgO* | (%) | 23.51 | 24.10 | 24.43 | 9.85 | 18.02 | 16.49 |
| *Mn3O4* | (%) | 0.09 | 0.08 | 0.08 | 0.19 | 0.09 | 0.10 |
| *Na2O* | (%) | 0.80 | 0.95 | 0.70 | 0.26 | 0.68 | 0.56 |
| *NiO* | (%) | 0.00 | 0.00 | 0.00 | 0.00 | 0.00 | 0.00 |
| *P2O5* | (%) | 0.09 | 0.05 | 0.04 | 0.05 | 0.00 | -0.01 |
| *PbO* | (%) | 0.03 | 0.02 | 0.02 | 0.13 | 0.05 | 0.07 |
| *SO3* | (%) | 0.34 | 0.59 | 0.45 | 8.17 | 0.82 | 1.66 |
| *SiO2* | (%) | 48.89 | 49.89 | 50.65 | 42.99 | 36.79 | 32.66 |
| *SrO* | (%) | 0.02 | 0.02 | 0.01 | 0.22 | 0.04 | 0.06 |
| *TiO2* | (%) | 0.02 | 0.01 | 0.01 | 0.00 | 0.00 | 0.00 |
| *V2O5* | (%) | 0.01 | 0.01 | 0.01 | 0.01 | 0.00 | 0.00 |
| *ZnO* | (%) | 0.21 | 0.20 | 0.27 | 0.46 | 0.85 | 1.01 |
| *ZrO2* | (%) | 0.00 | 0.00 | 0.00 | 0.00 | 0.00 | 0.00 |
| *Al2O3* | (%) | 1.59 | 1.61 | 1.29 | 0.79 | 1.01 | 0.85 |
| *BaO* | (%) | 0.13 | 0.14 | 0.12 | 17.66 | 0.31 | 0.34 |
| *CaO* | (%) | 0.29 | 0.34 | 0.30 | 0.63 | 1.49 | 3.35 |
| *Cr2O3* | (%) | 0.00 | 0.00 | 0.00 | 0.01 | 0.00 | 0.00 |
| *CuO* | (%) | 0.60 | 0.71 | 0.58 | 0.49 | 1.41 | 1.80 |
| *Fe2O3* | (%) | 13.91 | 12.37 | 12.15 | 11.64 | 26.58 | 27.73 |
| *HfO2* | (%) | -0.01 | 0.00 | -0.01 | 0.00 | -0.01 | 0.00 |
| *LOI* | (%) | 9.23 | 8.47 | 8.67 | 8.29 | 11.39 | 12.27 |
| **Sum** | (%) | 99.94 | 99.71 | 99.89 | 101.92 | 99.60 | 99.04 |

**Table B.4:** Results from the quantitative WROXI method. Samples from Mohn's Treasure.

| Sample nr. | | MT-PC-10023-1 | MT-PC-10028-1 | MT-PC-10029<5 | MT-PC-10029>5 | MT-PC-10031<5 | MT-PC-10031>5 | MT-PC-10033<1/2 | MT-PC-10033>1/2 | MT-PC-10035<1/2 | MT-PC-10035>1/2 | MT-PC-10036>1/2 | MT-PC-10037<1/2 | MT-PC-10037>1/2 |
|---|---|---|---|---|---|---|---|---|---|---|---|---|---|---|
| *K2O* | (%) | 2.76 | 2.21 | 0.74 | 1.51 | 0.58 | 2.11 | 3.06 | 1.66 | 2.76 | 2.88 | 3.42 | 2.66 | 2.86 |
| *MgO* | (%) | 1.55 | 1.77 | 1.35 | 1.62 | 0.98 | 1.74 | 2.47 | 1.98 | 1.76 | 1.84 | 1.57 | 1.54 | 1.90 |
| *Mn3O4* | (%) | 0.04 | 0.14 | 0.17 | 0.16 | 0.12 | 0.12 | 0.16 | 0.18 | 0.13 | 0.10 | 0.12 | 0.08 | 0.10 |
| *Na2O* | (%) | 1.75 | 1.07 | 1.34 | 1.66 | 0.96 | 1.77 | 2.09 | 1.75 | 2.17 | 2.16 | 1.06 | 1.87 | 2.04 |
| *NiO* | (%) | 0.01 | 0.00 | 0.00 | 0.00 | 0.00 | 0.00 | 0.00 | 0.00 | 0.00 | 0.00 | 0.01 | 0.00 | 0.00 |
| *P2O5* | (%) | 0.20 | 0.11 | 0.11 | 0.11 | 0.08 | 0.10 | 0.12 | 0.13 | 0.14 | 0.13 | 0.92 | 0.22 | 0.19 |
| *PbO* | (%) | 0.00 | 0.01 | 0.00 | 0.00 | 0.00 | 0.00 | 0.00 | 0.00 | 0.00 | 0.00 | 0.00 | 0.00 | 0.00 |
| *SO3* | (%) | 0.02 | 0.04 | 0.21 | 0.07 | 0.23 | 0.02 | 0.01 | 0.12 | 0.02 | 0.02 | 0.35 | 0.02 | 0.03 |
| *SiO2* | (%) | 63.23 | 46.73 | 36.13 | 47.27 | 30.06 | 58.71 | 56.44 | 45.78 | 63.89 | 62.68 | 48.72 | 63.30 | 61.03 |
| *SrO* | (%) | 0.02 | 0.05 | 0.10 | 0.06 | 0.10 | 0.04 | 0.02 | 0.05 | 0.01 | 0.02 | 0.04 | 0.02 | 0.01 |
| *TiO2* | (%) | 0.79 | 0.53 | 0.42 | 0.52 | 0.31 | 0.52 | 0.67 | 0.56 | 0.71 | 0.69 | 0.77 | 0.78 | 0.75 |
| *V2O5* | (%) | 0.03 | 0.02 | 0.02 | 0.02 | 0.01 | 0.02 | 0.02 | 0.02 | 0.03 | 0.03 | 0.04 | 0.03 | 0.03 |
| *ZnO* | (%) | 0.01 | 0.01 | 0.01 | 0.01 | 0.0043 | 0.01 | 0.00 | 0.01 | 0.01 | 0.00 | 0.01 | 0.01 | 0.01 |
| *ZrO2* | (%) | 0.03 | 0.02 | 0.02 | 0.02 | 0.01 | 0.02 | 0.02 | 0.03 | 0.04 | 0.03 | 0.02 | 0.03 | 0.03 |
| *Al2O3* | (%) | 15.16 | 10.32 | 7.59 | 9.62 | 5.59 | 10.59 | 13.36 | 10.76 | 14.11 | 13.98 | 16.58 | 14.49 | 14.44 |
| *BaO* | (%) | 0.07 | 0.05 | 0.05 | 0.06 | 0.04 | 0.05 | 0.06 | 0.05 | 0.06 | 0.06 | 0.15 | 0.06 | 0.06 |
| *CaO* | (%) | 0.64 | 15.43 | 23.33 | 15.02 | 29.82 | 8.19 | 5.19 | 13.90 | 0.88 | 2.33 | 1.86 | 0.52 | 1.98 |
| *Cr2O3* | (%) | 0.02 | 0.01 | 0.01 | 0.01 | 0.01 | 0.01 | 0.01 | 0.01 | 0.01 | 0.01 | 0.01 | 0.02 | 0.01 |
| *CuO* | (%) | 0.00 | 0.00 | 0.00 | 0.00 | 0.00 | 0.00 | 0.00 | 0.00 | 0.01 | 0.01 | 0.01 | 0.01 | 0.01 |
| *Fe2O3* | (%) | 6.81 | 4.54 | 3.52 | 4.19 | 2.61 | 4.27 | 5.80 | 5.02 | 5.92 | 5.58 | 14.06 | 7.11 | 6.54 |
| *HfO2* | (%) | 0.00 | -0.01 | 0.00 | 0.00 | 0.00 | 0.00 | 0.00 | 0.00 | 0.00 | 0.00 | 0.00 | 0.00 | -0.01 |
| *LOI* | (%) | 5.88 | 15.99 | 24.07 | 16.92 | 27.75 | 10.82 | 9.44 | 16.97 | 6.32 | 6.99 | 10.01 | 6.64 | 7.36 |
| **Sum** | (%) | 98.99 | 99.05 | 99.18 | 98.85 | 99.24 | 99.10 | 98.96 | 99.00 | 99.00 | 99.53 | 99.73 | 99.41 | 99.38 |

**Table B.5:** The XRF results for the fragments. Results from LC-SS-10008-1

| Sample nr. | | LC-SAMLE-10007 | LC-SS-10008-1 (omnian method) | LC-SS-10008-2 | MT-PC-10023-1-1 | MT-PC-10023-1-2 | MT-PC-10036>1/2 |
|---|---|---|---|---|---|---|---|
| *Mn3O4* | (%) | -0.008 | 0.037 | 0.018 | 0.028 | 0.165 | 0.406 |
| *MgO* | (%) | 0.008 | 1.579 | 2.068 | 0.540 | 0.802 | 4.747 |
| *Al2O3* | (%) | 0.104 | 0.141 | 0.090 | 13.051 | 10.591 | 8.024 |
| *SiO2* | (%) | 55.386 | 9.138 | 11.699 | 73.526 | 46.951 | 24.041 |
| *P2O5* | (%) | -0.020 | 0.000 | -0.014 | -0.003 | 0.093 | 0.090 |
| *SO3* | (%) | 13.679 | 52.600 | 32.952 | 0.003 | 0.195 | 0.055 |
| *BaO* | (%) | 25.775 | 0.162 | 0.167 | 0.064 | 0.080 | 0.060 |
| *K2O* | (%) | 0.027 | 0.000 | 0.027 | 2.628 | 1.922 | 1.561 |
| *CaO* | (%) | 0.115 | 0.779 | 26.269 | 2.083 | 16.663 | 3.173 |
| *TiO2* | (%) | -0.029 | 0.000 | -0.005 | 0.326 | 0.300 | 0.402 |
| *Na2O* | (%) | 0.110 | 0.258 | 0.166 | 3.591 | 2.269 | 0.334 |
| *Cr2O3* | (%) | 0.000 | 0.000 | 0.002 | 0.000 | 0.005 | 0.008 |
| *SrO* | (%) | 0.332 | 0.005 | 0.114 | 0.044 | 0.110 | 0.019 |
| *Fe2O3* | (%) | 0.436 | 33.097 | 5.205 | 1.913 | 2.926 | 32.586 |
| *HfO2* | (%) | -0.002 | - | 0.001 | -0.002 | -0.002 | -0.002 |
| *PbO* | (%) | 0.022 | 0.037 | 0.041 | 0.005 | 0.002 | 0.003 |
| *CuO* | (%) | 0.025 | 1.218 | 0.178 | 0.001 | 0.003 | 0.004 |
| *ZnO* | (%) | 0.016 | 0.688 | 0.475 | 0.006 | 0.005 | 0.011 |
| *NiO* | (%) | 0.003 | 0.000 | -0.002 | -0.001 | 0.003 | 0.016 |
| *V2O5* | (%) | 0.004 | 0.000 | 0.000 | 0.005 | 0.008 | 0.022 |
| *ZrO2* | (%) | 0.002 | 0.000 | -0.010 | 0.056 | 0.016 | 0.017 |
| *LOI* | (%) | 2.880 | - | 19.360 | 0.630 | 15.690 | 24.090 |
| **Sum** | (%) | 98.864 | 99.738 | 98.804 | 98.493 | 98.798 | 99.668 |

## B.1.3 XRD-results

### Loki's Castle

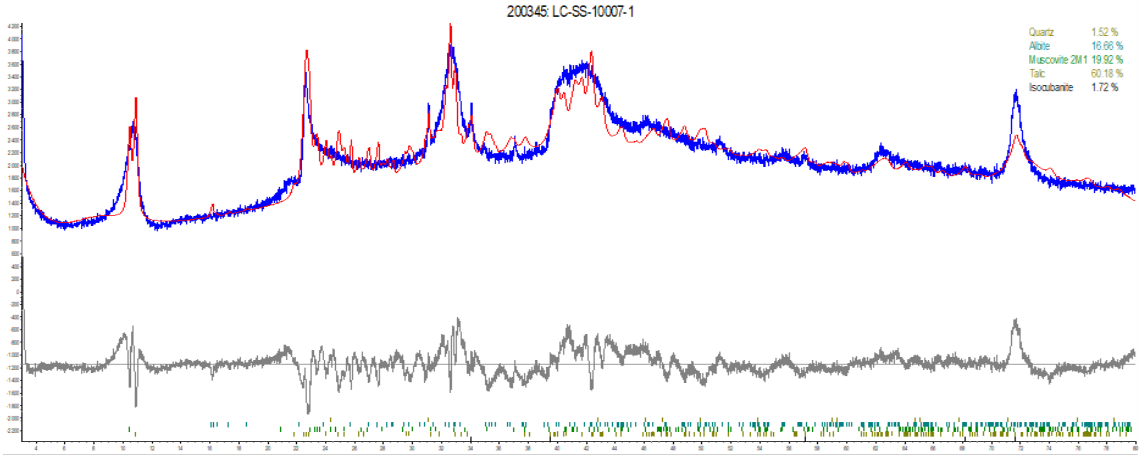

200346: LC-SS-10007-2

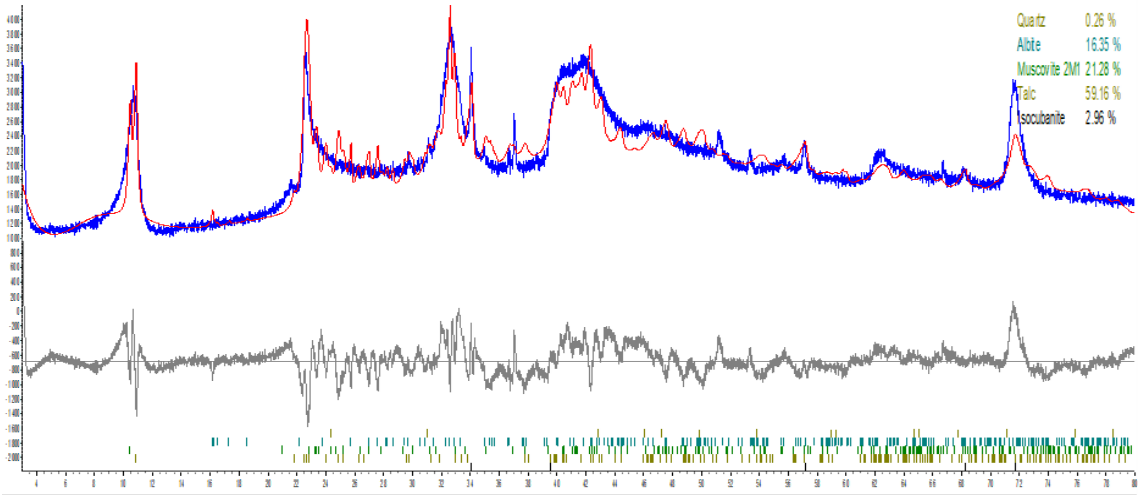


200347: LC-SS-10007-3

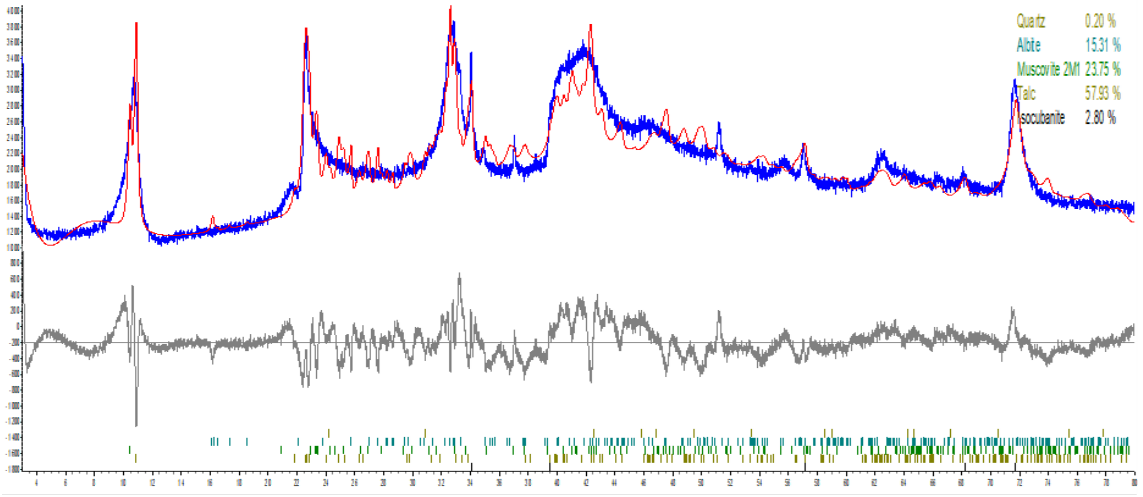


200348: LC-Samle-10007-4

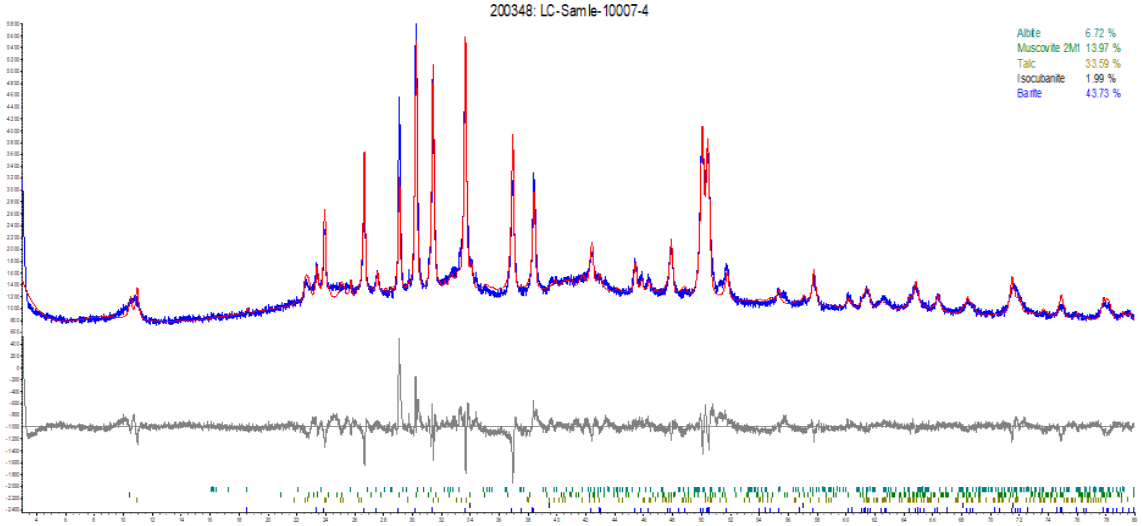

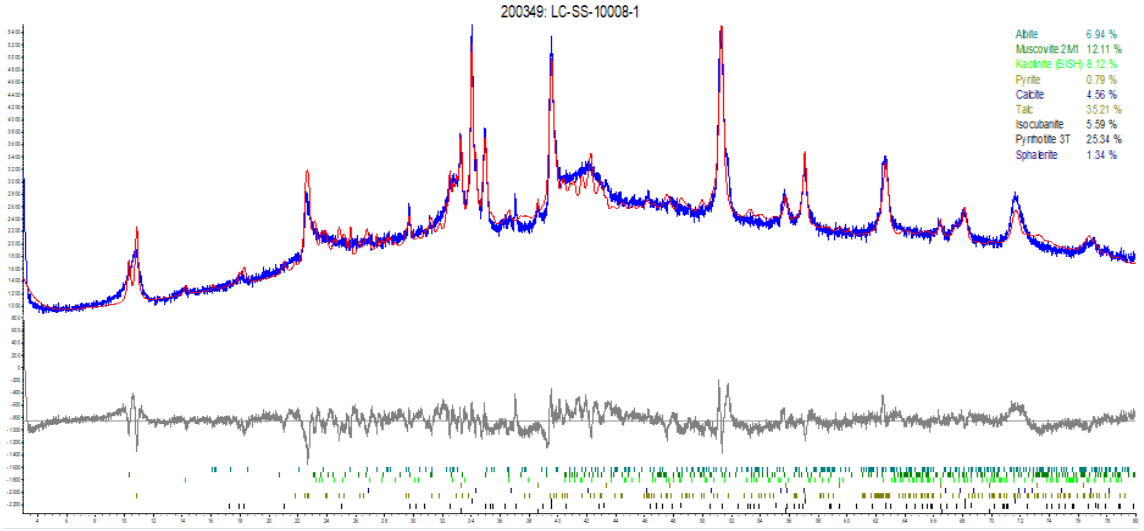


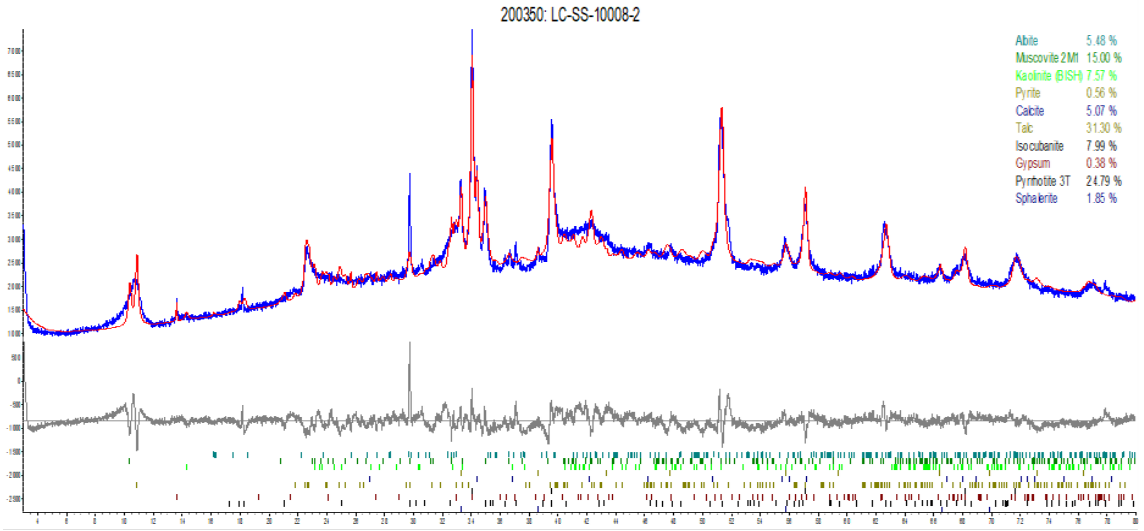


## Mohn's Treasure

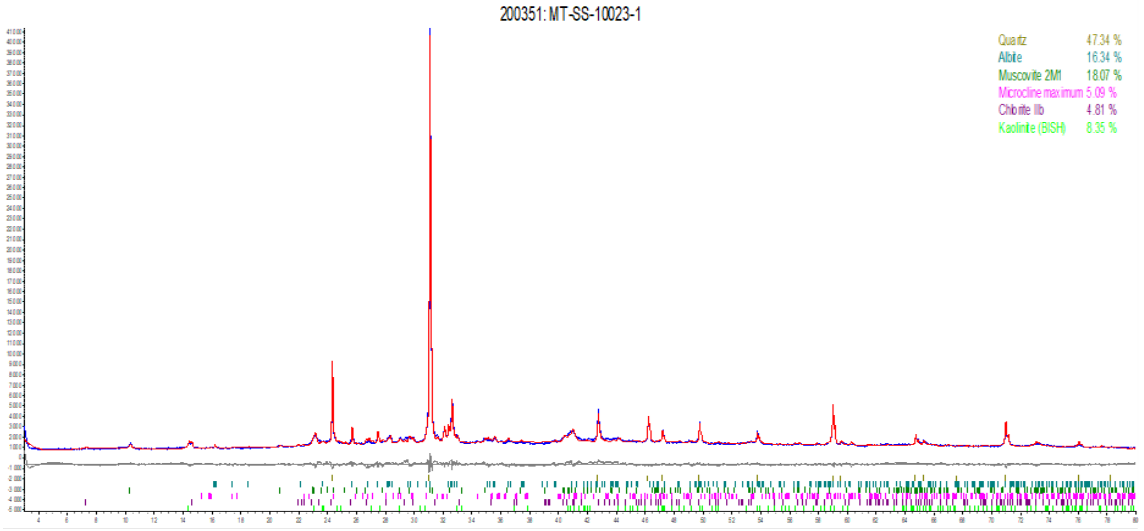

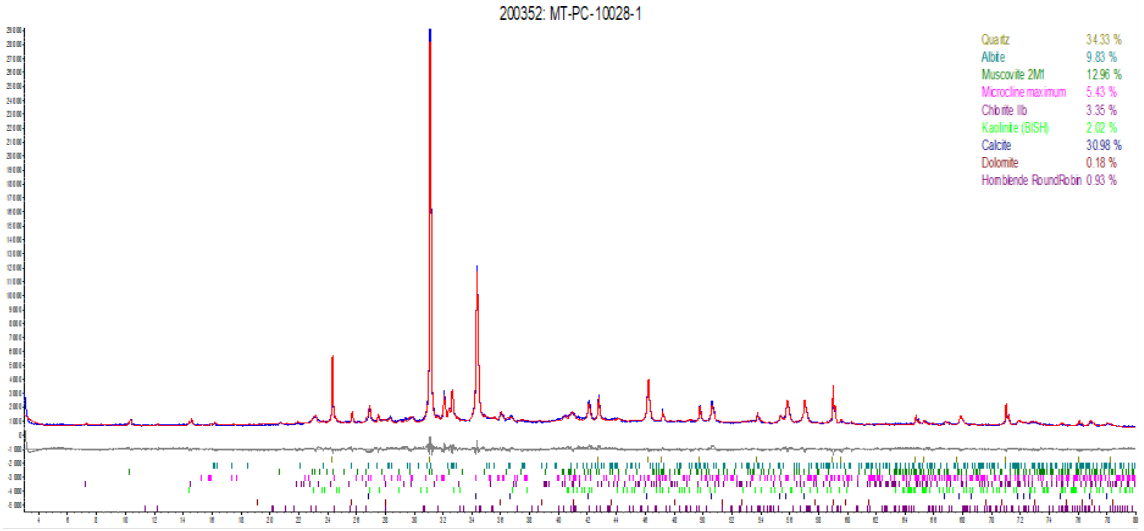
200352: MT-PC-10028-1
Quartz 34.33 %
Albite 9.83 %
Muscovite 2M1 12.96 %
Microcline maximum 5.43 %
Chlorite IIb 3.35 %
Kaolinite (BISH) 2.02 %
Calcite 30.98 %
Dolomite 0.18 %
Hornblende RoundRobin 0.93 %

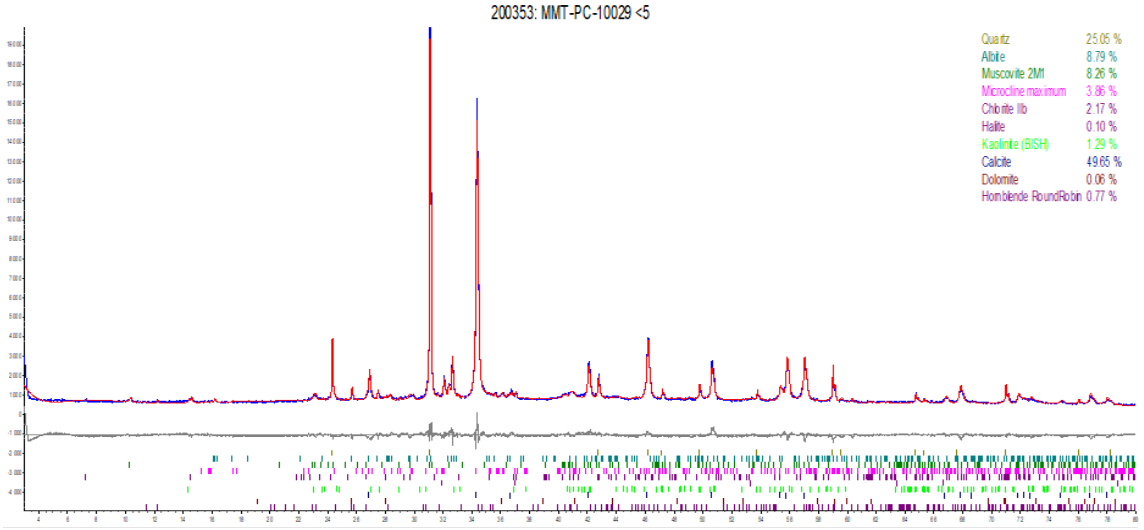
200353: MMT-PC-10029 <5
Quartz 25.05 %
Albite 8.79 %
Muscovite 2M1 8.26 %
Microcline maximum 3.86 %
Chlorite IIb 2.17 %
Halite 0.10 %
Kaolinite (BISH) 1.29 %
Calcite 49.65 %
Dolomite 0.06 %
Hornblende RoundRobin 0.77 %

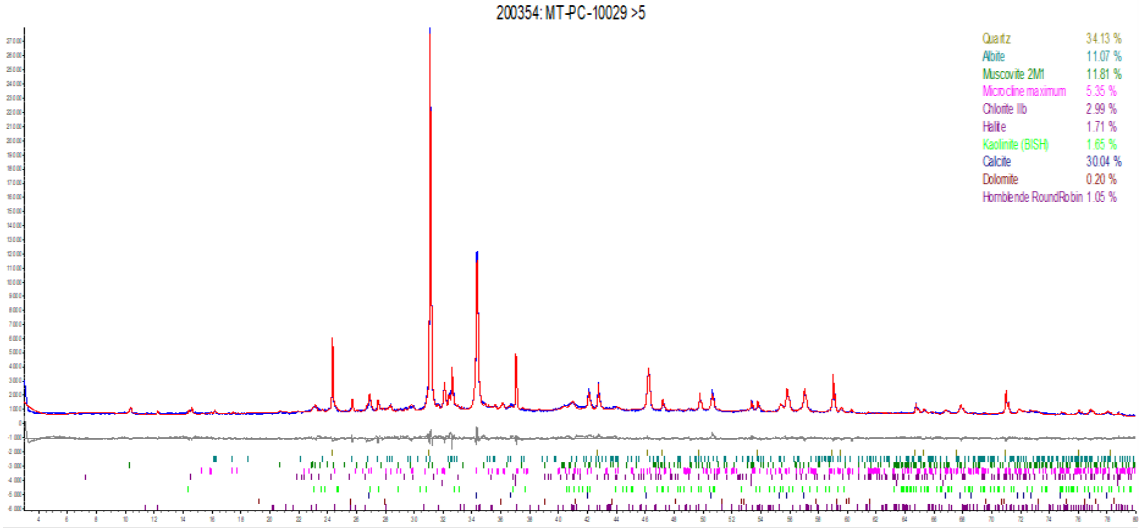
200354: MT-PC-10029 >5
Quartz 34.13 %
Albite 11.07 %
Muscovite 2M1 11.81 %
Microcline maximum 5.35 %
Chlorite IIb 2.99 %
Halite 1.71 %
Kaolinite (BISH) 1.65 %
Calcite 30.04 %
Dolomite 0.20 %
Hornblende RoundRobin 1.05 %

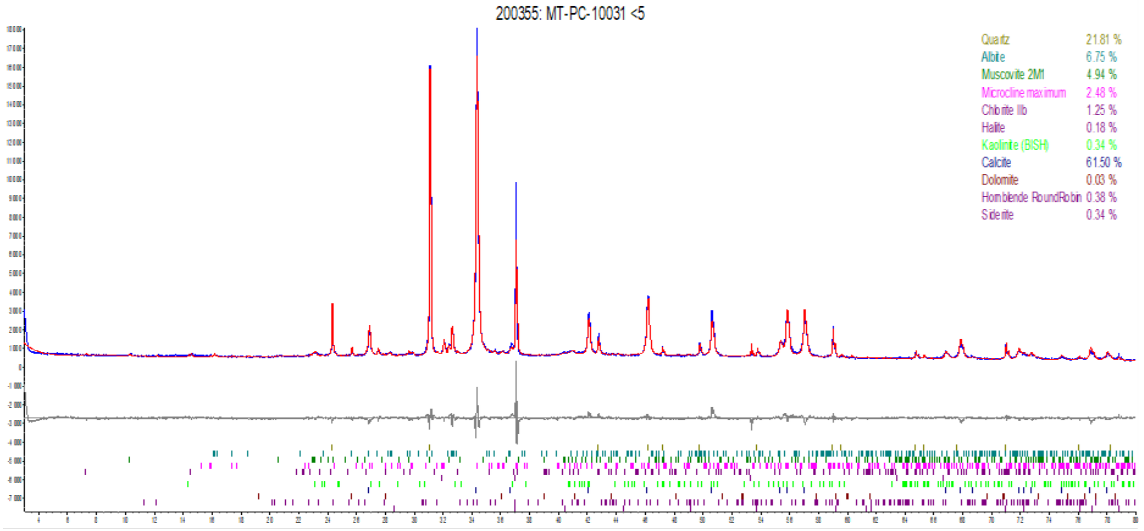
200355: MT-PC-10031 <5
Quartz 21.81 %
Albite 6.75 %
Muscovite 2M1 4.94 %
Microcline maximum 2.48 %
Chlorite IIb 1.25 %
Halite 0.18 %
Kaolinite (BISH) 0.34 %
Calcite 61.50 %
Dolomite 0.03 %
Hornblende RoundRobin 0.38 %
Siderite 0.34 %

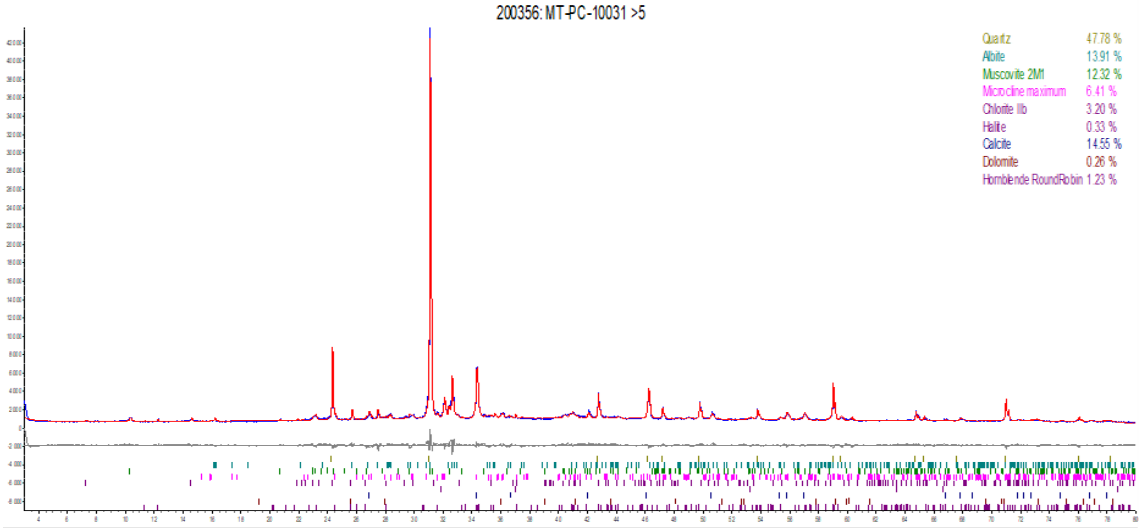
200356: MT-PC-10031 >5
Quartz 47.78 %
Albite 13.91 %
Muscovite 2M1 12.32 %
Microcline maximum 6.41 %
Chlorite IIb 3.20 %
Halite 0.33 %
Calcite 14.55 %
Dolomite 0.26 %
Hornblende RoundRobin 1.23 %

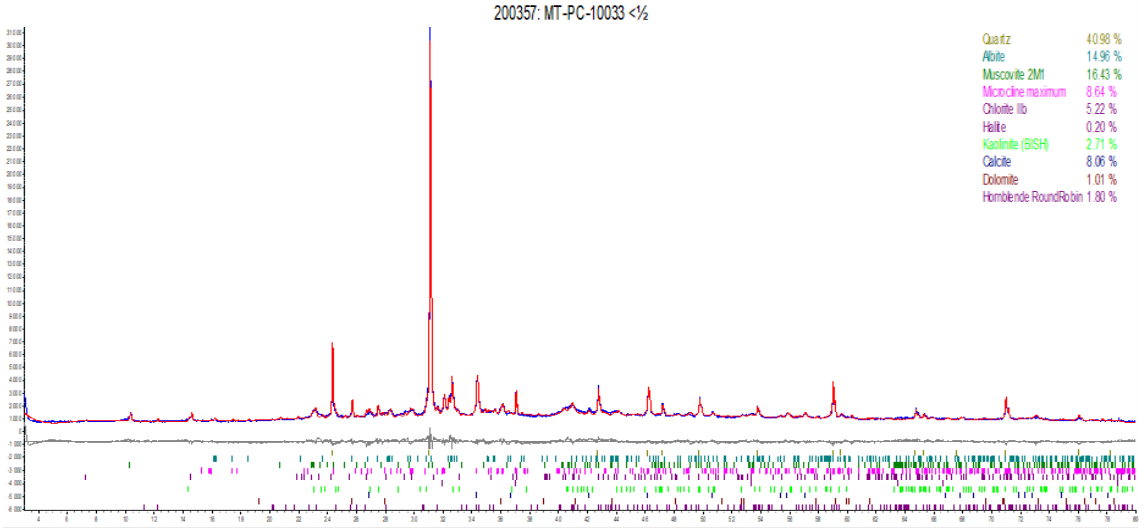
200357: MT-PC-10033 <½
Quartz 40.98 %
Albite 14.96 %
Muscovite 2M1 16.43 %
Microcline maximum 8.64 %
Chlorite IIb 5.22 %
Halite 0.20 %
Kaolinite (BISH) 2.71 %
Calcite 8.06 %
Dolomite 1.01 %
Hornblende RoundRobin 1.80 %

200358: MT-PC-10033 >½

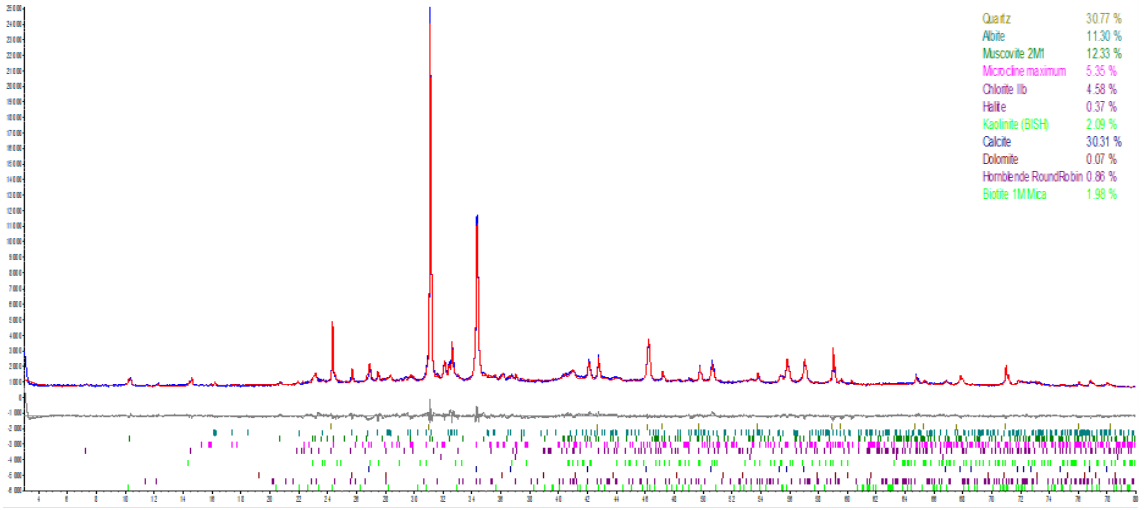


200359: MT-PC-10035 <½

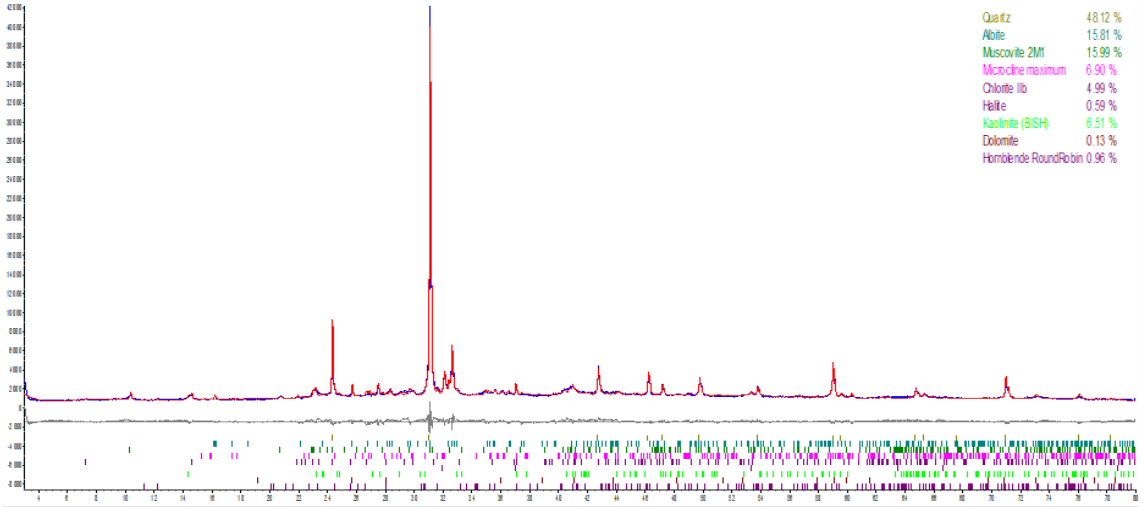


200360: MT-PC-10035 >½

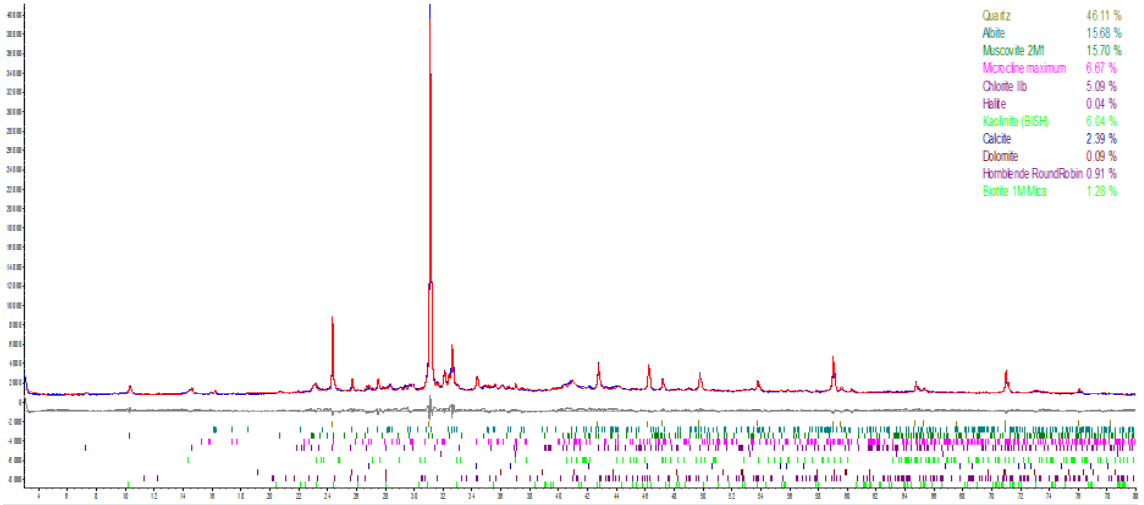

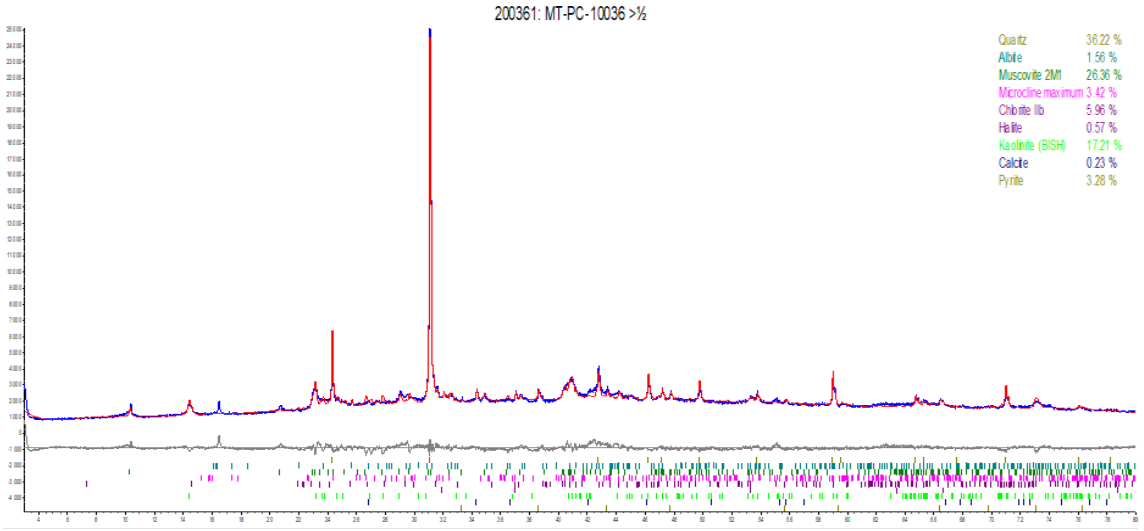
200361: MT-PC-10036 >½
Quartz 36.22 %
Albite 1.56 %
Muscovite 2M1 26.36 %
Microcline maximum 3.42 %
Chlorite IIb 5.96 %
Halite 0.57 %
Kaolinite (BISH) 17.21 %
Calcite 0.23 %
Pyrite 3.28 %

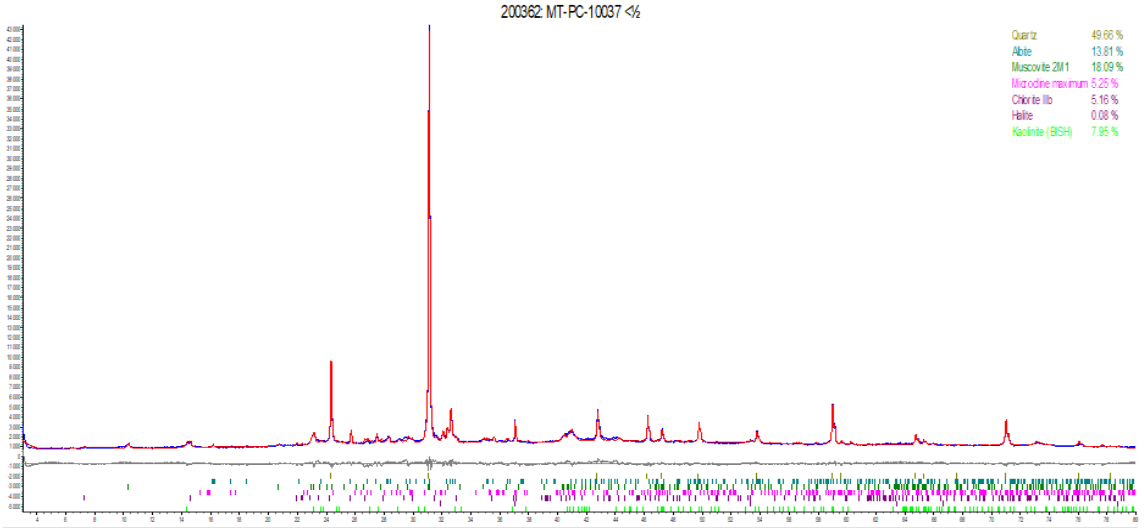
200362: MT-PC-10037 <½
Quartz 49.66 %
Albite 13.81 %
Muscovite 2M1 18.09 %
Microcline maximum 5.25 %
Chlorite IIb 5.16 %
Halite 0.08 %
Kaolinite (BISH) 7.95 %

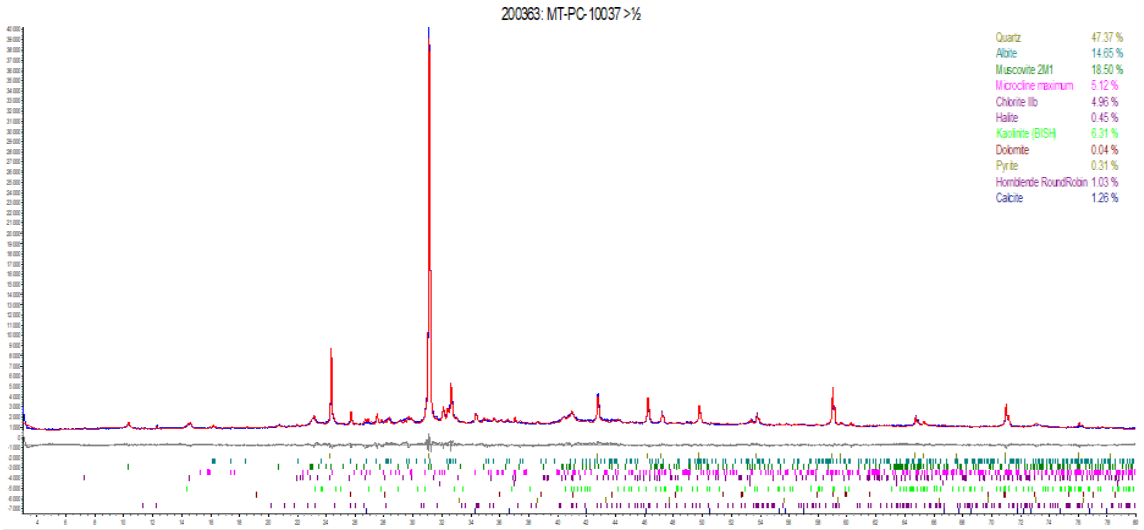
200363: MT-PC-10037 >½
Quartz 47.37 %
Albite 14.65 %
Muscovite 2M1 18.50 %
Microcline maximum 5.12 %
Chlorite IIb 4.96 %
Halite 0.45 %
Kaolinite (BISH) 6.31 %
Dolomite 0.04 %
Pyrite 0.31 %
Hornblende RoundRobin 1.03 %
Calcite 1.26 %

**Table B.6:** The calculated wt.% hydrohtermal component based on XRF and XRD. The XRF method used is the WROXI method.

| | Al WROXI | Bio. Comp XRD: | Lit. Comp WROXI: | Hyd.Comp WROXI | Fe WROXI |
|---|---|---|---|---|---|
| LC-SS-10007-1 | 0.841 | 0.000 | 8.410 | 91.590 | 9.734 |
| LC-SS-10007-2 | 0.855 | 0.000 | 8.548 | 91.452 | 8.659 |
| LC-SS-10007-3 | 0.684 | 0.000 | 6.840 | 93.160 | 8.506 |
| LC-Samle-10007 | 0.421 | 0.000 | 4.209 | 95.791 | 8.145 |
| LC-SS-10008-1 | 0.534 | 4.560 | 5.345 | 90.095 | 18.606 |
| LC-SS-10008-2 | 0.452 | 5.070 | 4.519 | 90.411 | 19.413 |
| MT-PC-10023-1 | 8.035 | 0.000 | 80.347 | 19.653 | 4.767 |
| MT-PC-10028-1 | 5.471 | 30.980 | 54.705 | 14.315 | 3.177 |
| MT-PC-10029<5 | 4.021 | 49.650 | 40.214 | 10.136 | 2.466 |
| MT-PC-10029>5 | 5.100 | 30.040 | 51.000 | 18.960 | 2.930 |
| MT-PC-10031<5 | 2.962 | 61.500 | 29.617 | 8.883 | 1.826 |
| MT-PC-10031>5 | 5.611 | 14.550 | 56.106 | 29.344 | 2.987 |
| MT-PC-10033<1/2 | 7.081 | 9.070 | 70.807 | 20.123 | 4.060 |
| MT-PC-10033>1/2 | 5.701 | 30.310 | 57.010 | 12.680 | 3.517 |
| MT-PC-10035<1/2 | 7.479 | 0.000 | 74.794 | 25.206 | 4.143 |
| MT-PC-10035>1/2 | 7.408 | 2.390 | 74.077 | 23.533 | 3.904 |
| MT-PC-10036>1/2 | 8.787 | 0.000 | 87.869 | 12.131 | 9.841 |
| MT-PC-10037<1/2 | 7.677 | 0.000 | 76.772 | 23.228 | 4.979 |
| MT-PC-10037>1/2 | 7.652 | 1.260 | 76.525 | 22.215 | 4.580 |

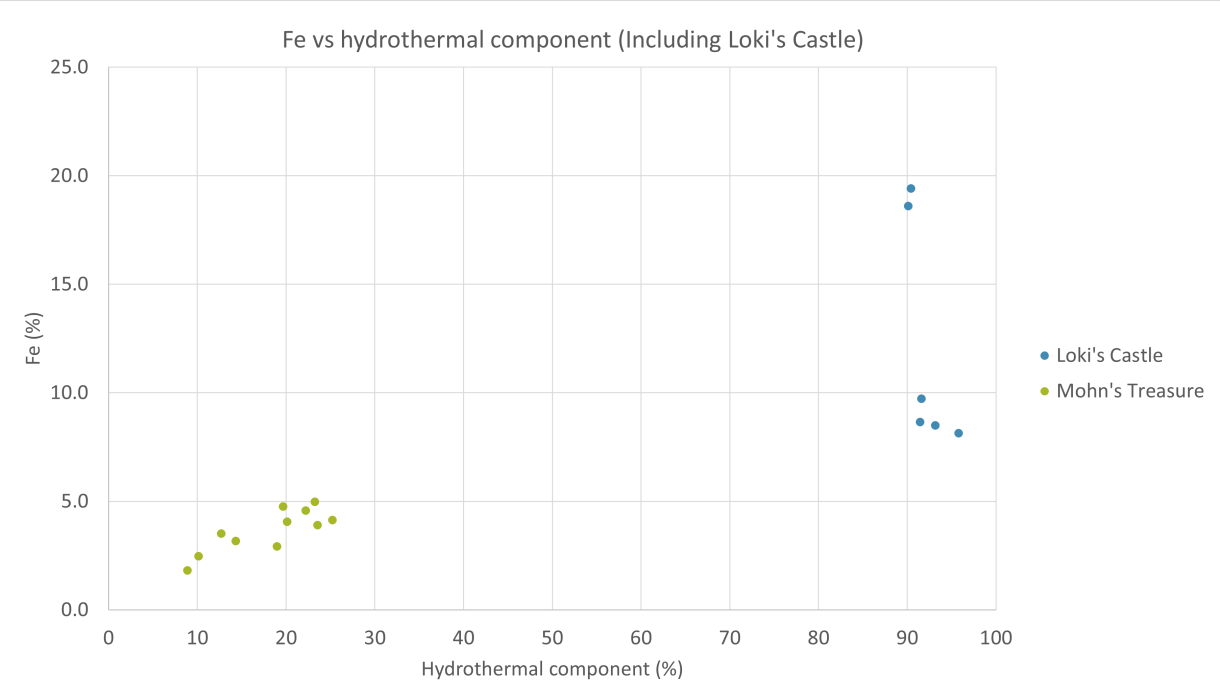


**Figure B.1:** Estimation of hydrothermal component vs total iron content in the *sediment* samples from Mohn's Treasure and Loki's Castle. The hydrothermal component is calculated using the WROXI data and the calcite estimations from XRD. The Fe-concentrations are also from WROXI.

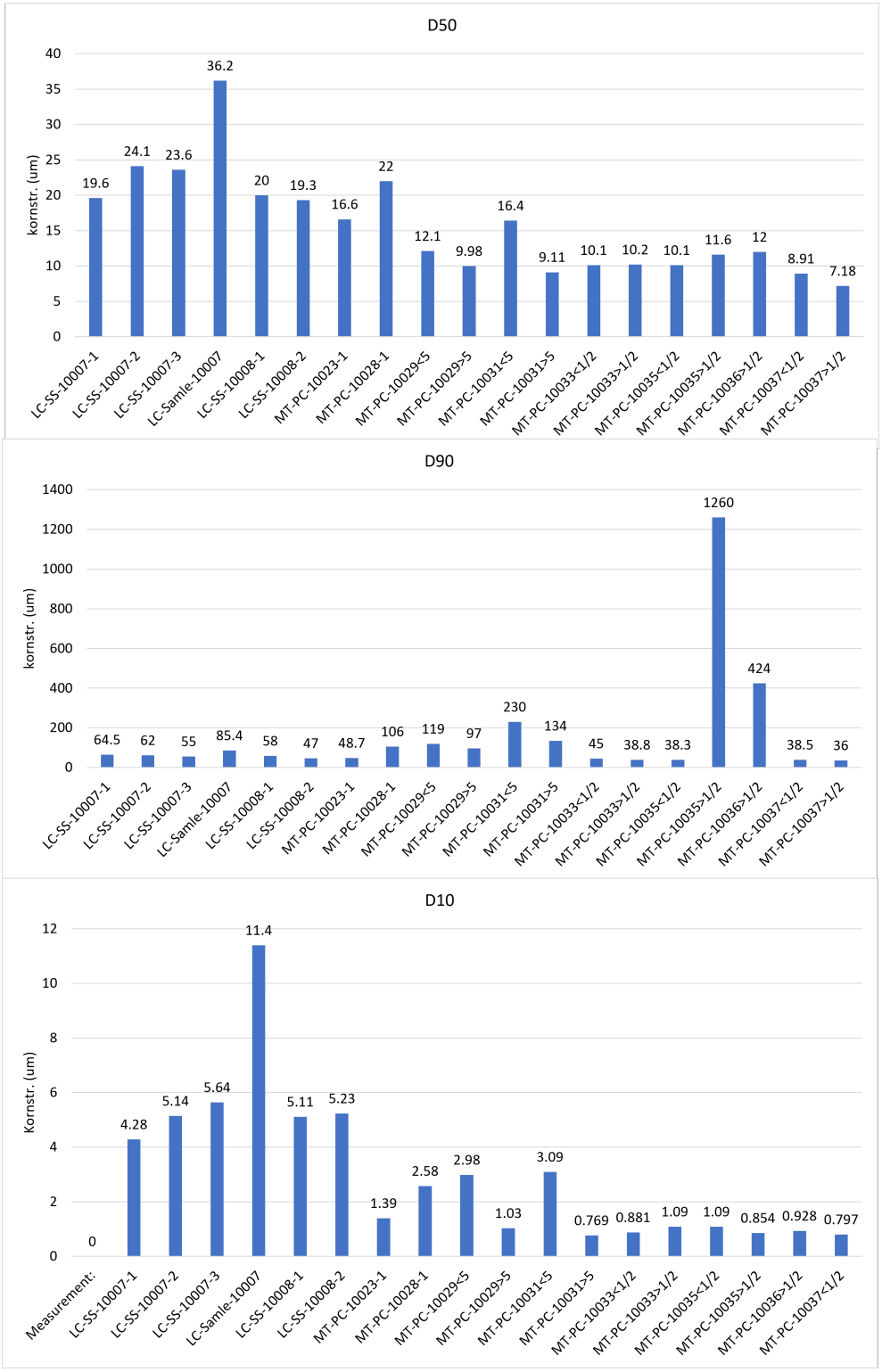


**Figure B.2:** Particle size distribution patterns for the sediment samples

## B.2 Stub Images

### B.2.1 Sediments Polished Block

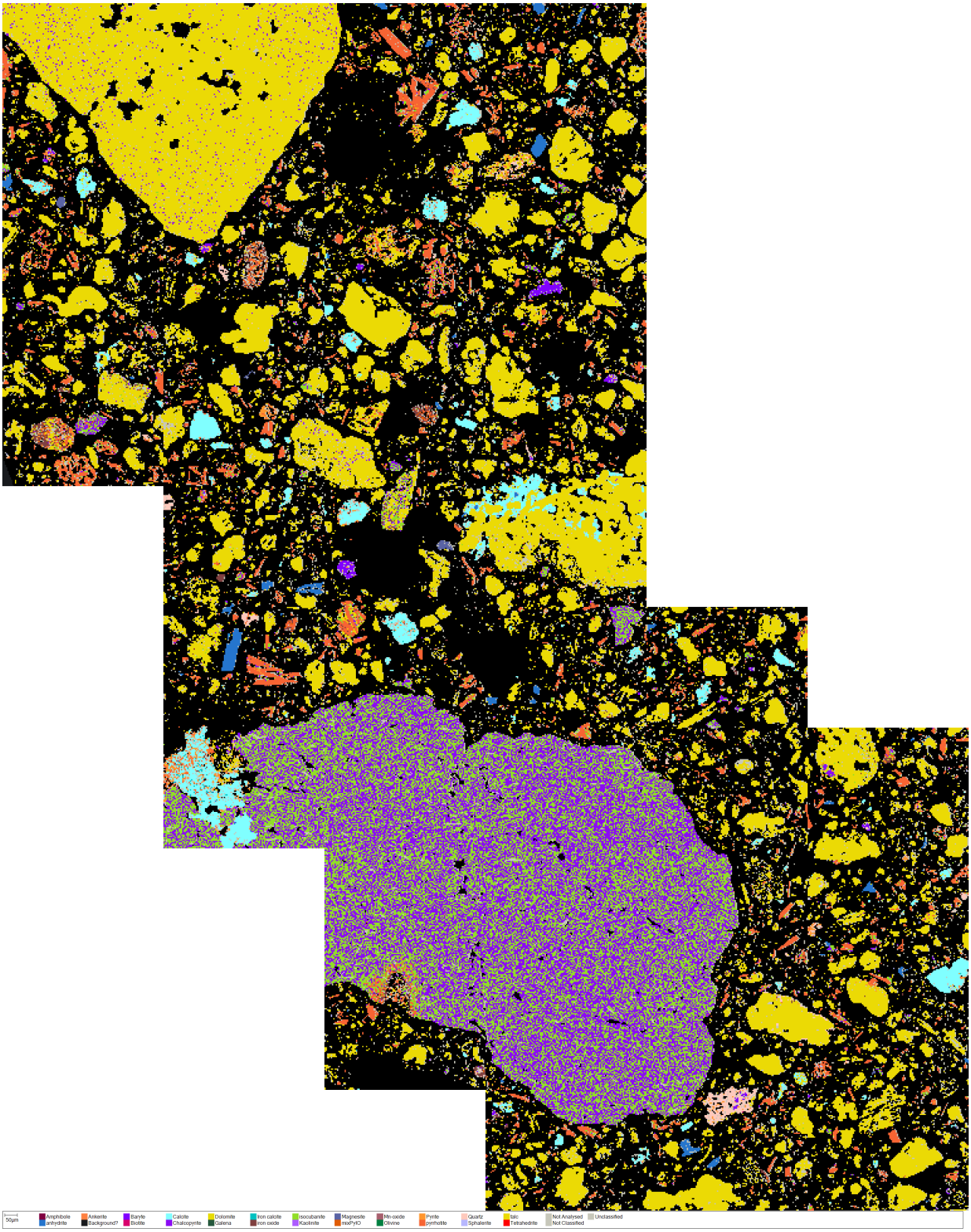


**Figure B.3:** AMS montage of the sediment block from LC-SS-10008-2

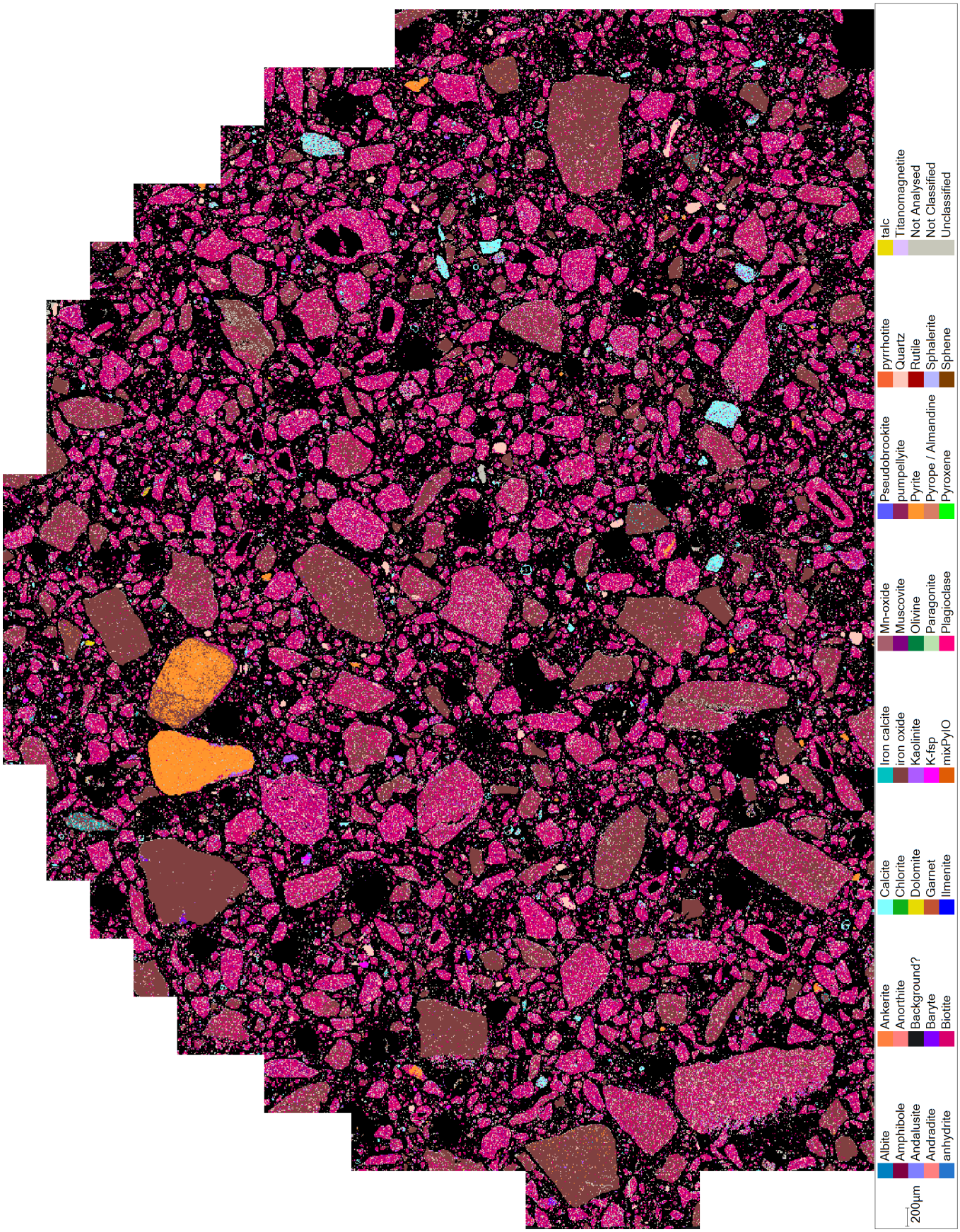


**Figure B.4:** AMS montage of the sediment block from MT-PC-10036

### B.2.2 Polished Blocks and Thin Sections of Fragments

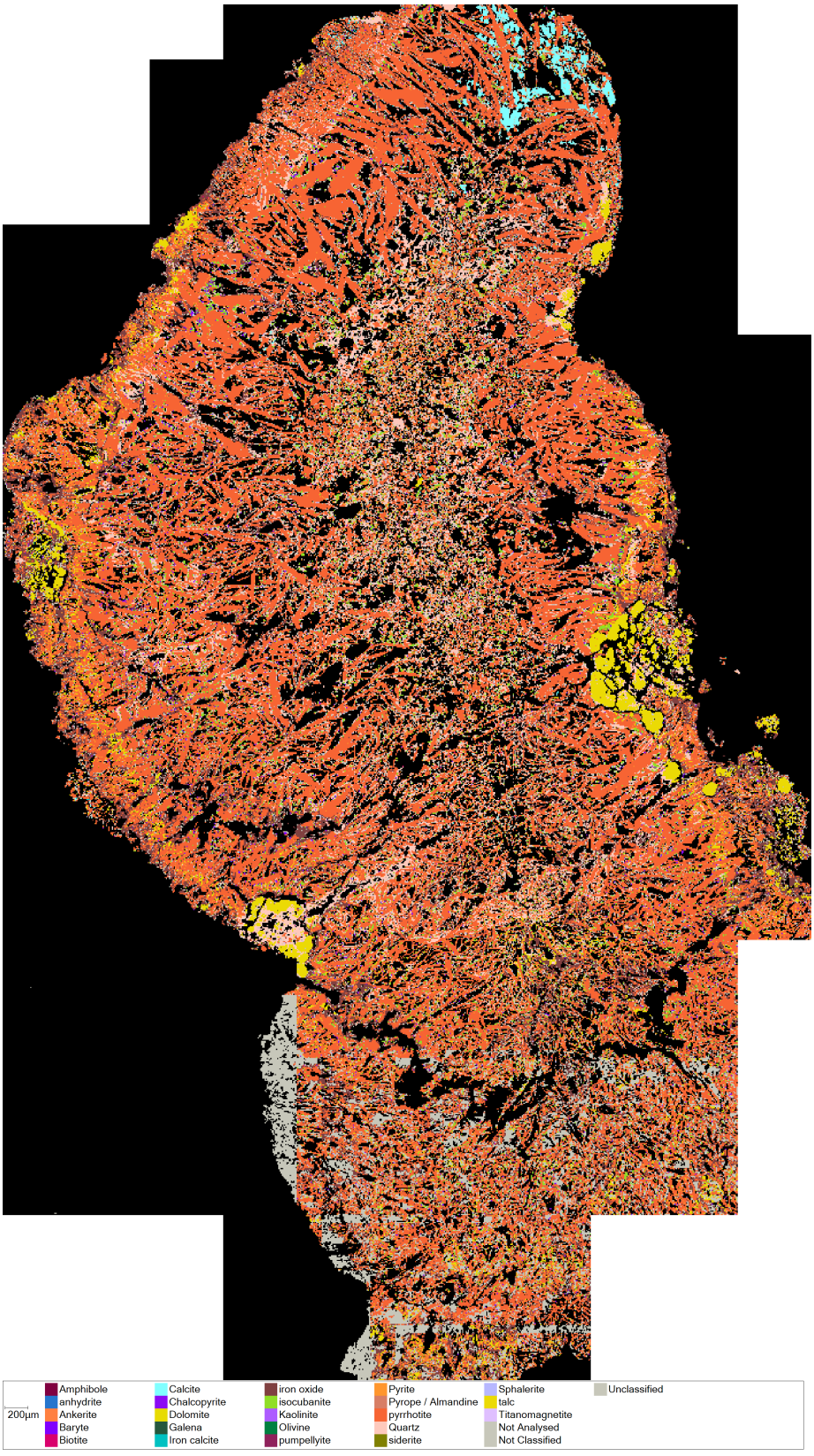


**Figure B.5:** AMS montage of the polished block made from the fragment from LC-SS-10008-1

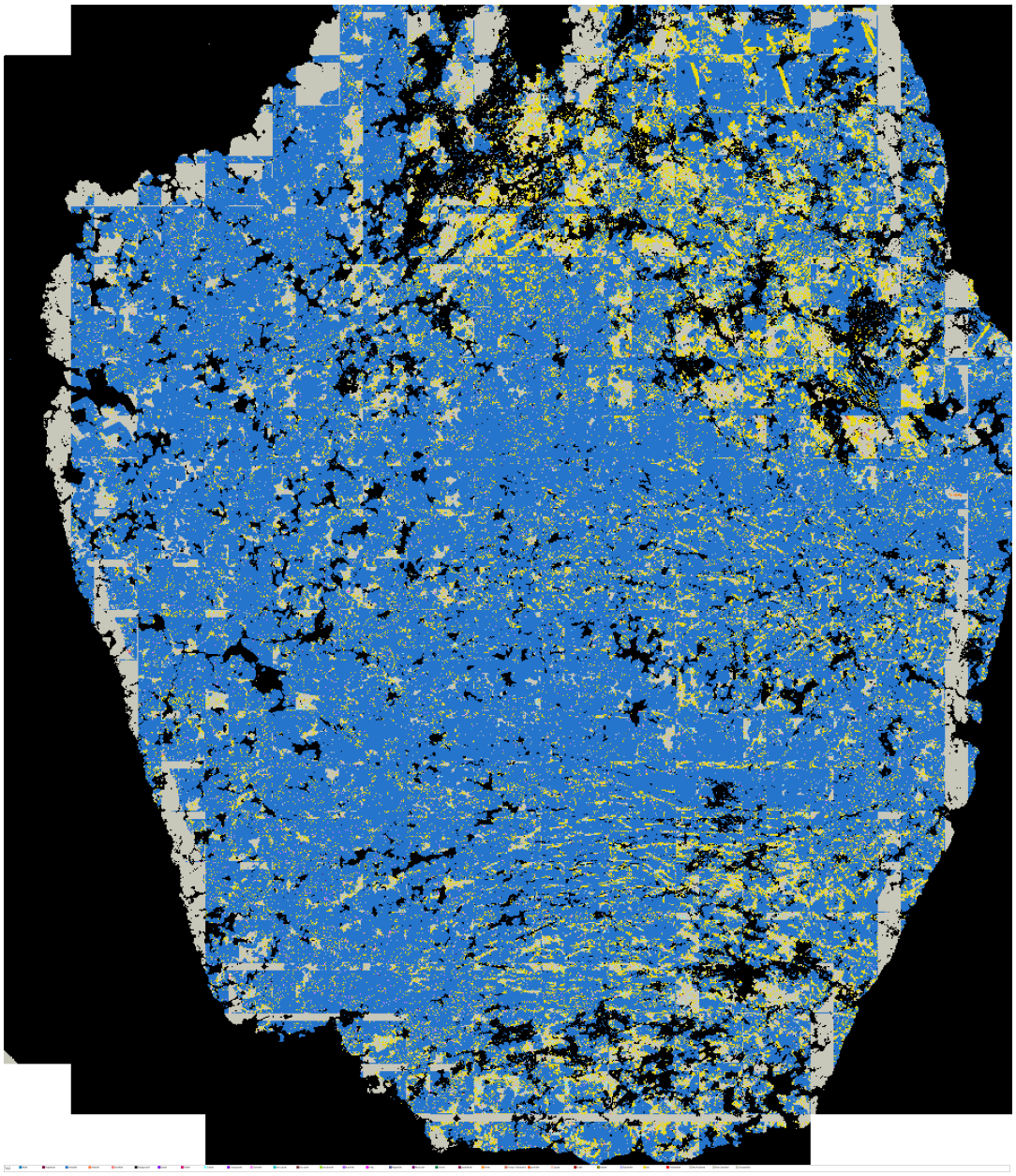

**Figure B.6:** AMS montage of the polished block made from the fragment from LC-SS-10008-2.

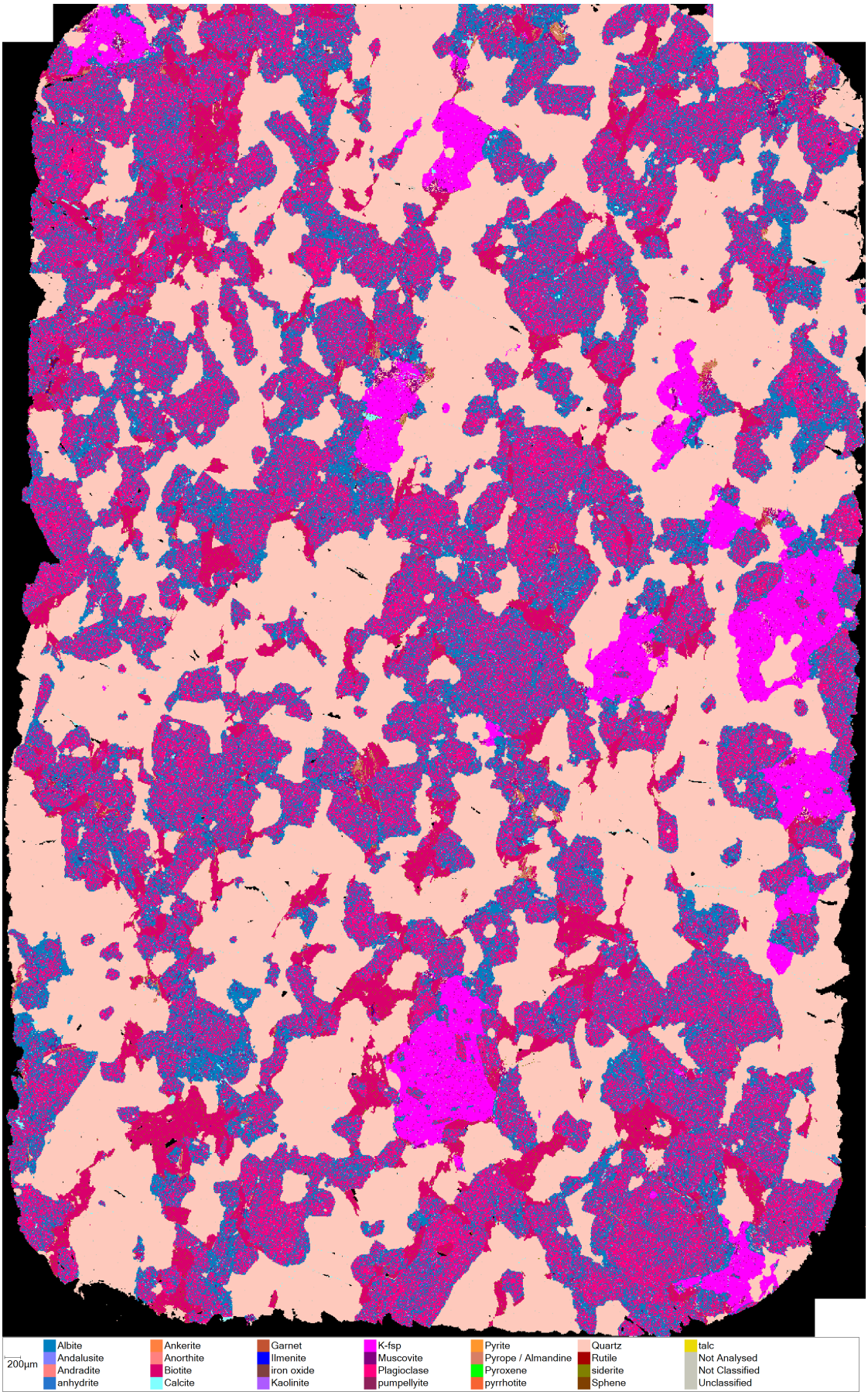


**Figure B.7:** AMS montage of the polished thin section made from the fragment from MT-PC-10023-1-1.

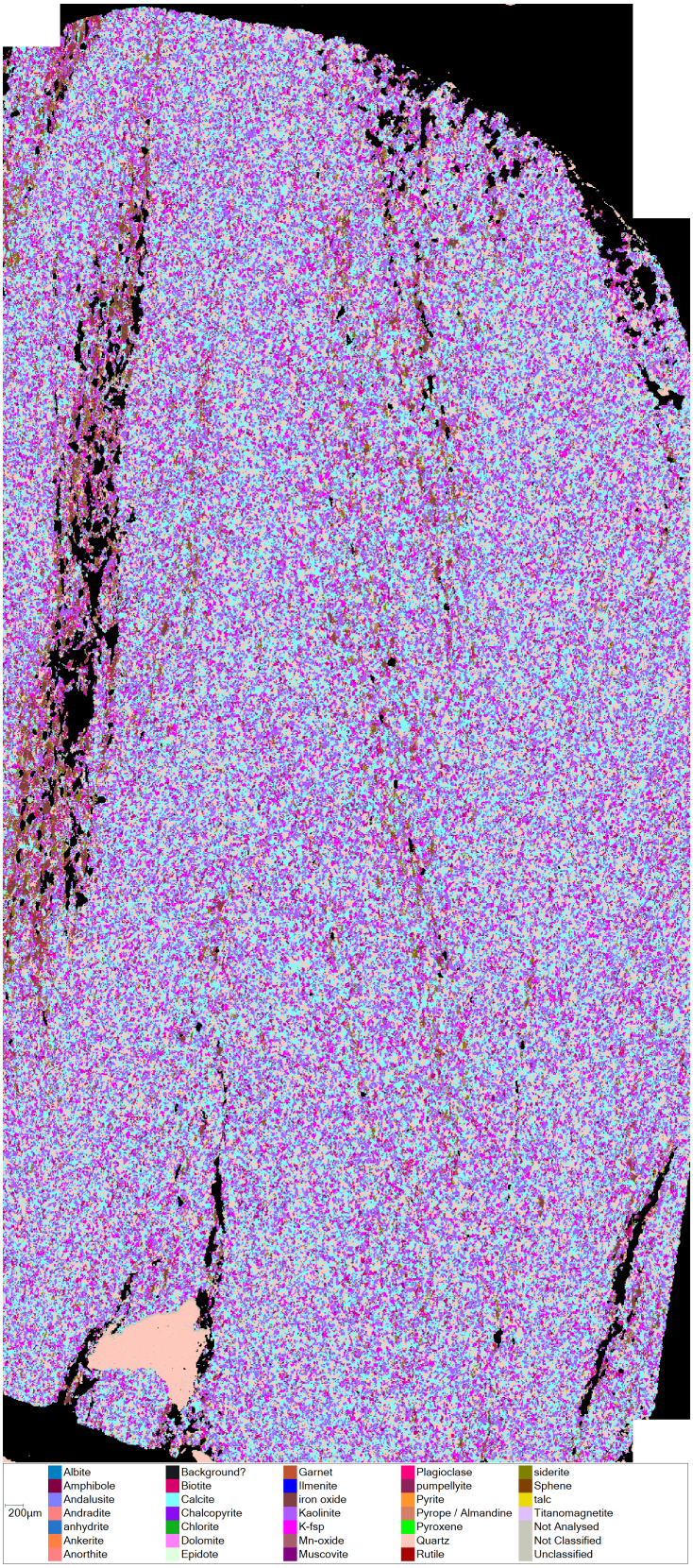


**Figure B.8:** AMS montage of the polished thin section made from the fragment from MT-PC-10023-1-2.

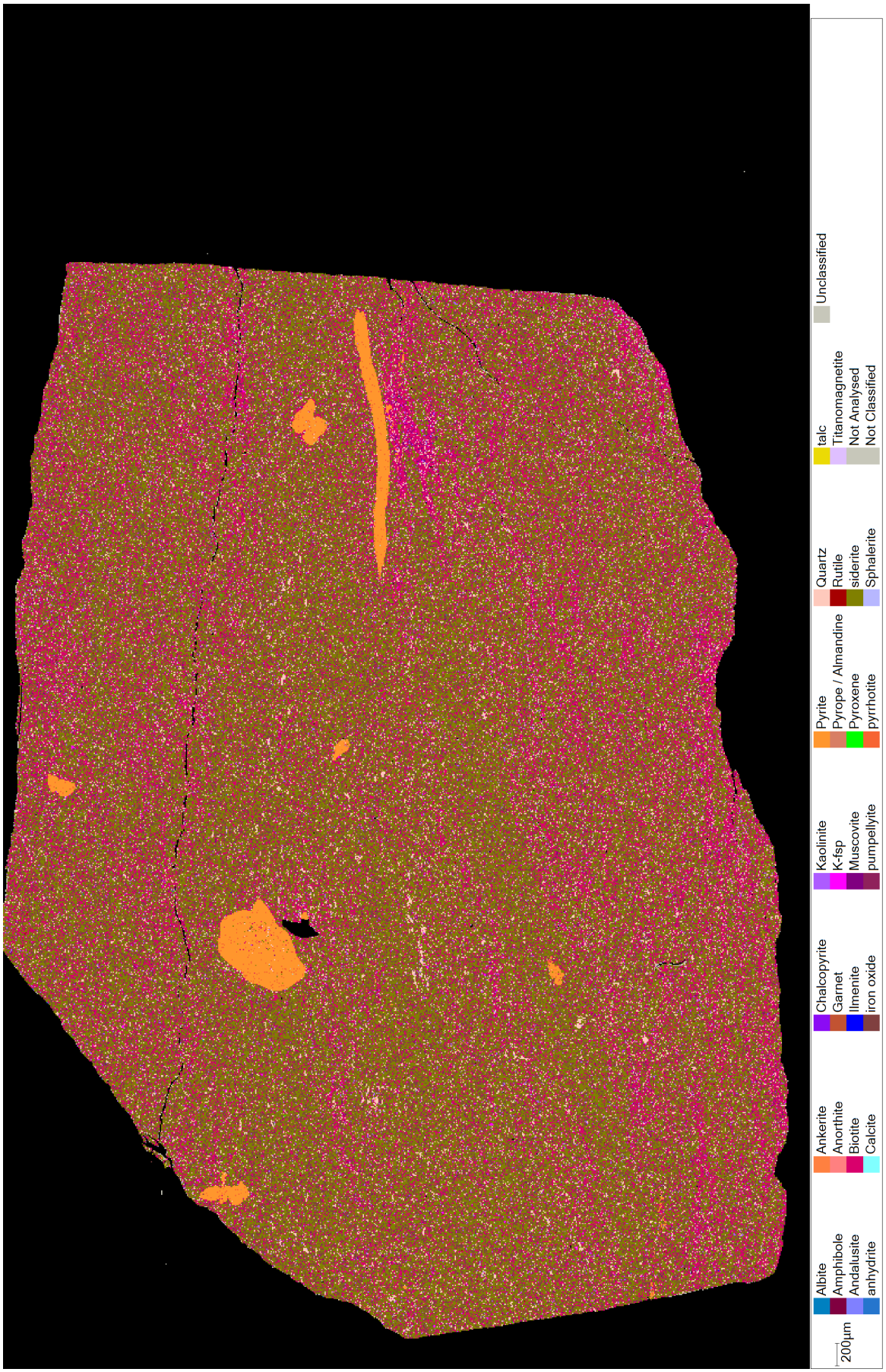


**Figure B.9:** AMS montage of the polished thin section made from the fragment from MT-PC-10036>1/2.

## B.3 ALS Certificate

Below follows the recieved analyses from ALS. Additional analyses was requested for sample LC-SS-10008-1 and LC-SAMLE-10007.

ALS Scandinavia AB
Hammarvagen 22
SE-943 36, Ojebyn
www.alsglobal.com/geochemistry

To: **NTNU**
**SEM SELANDSVEI 1**
**NO-7491 TRONDHEIM**
**NORWAY**


**Finalized Date: 2-APR-2021**
**Account: MINGOR**

# CERTIFICATE PI21064020

Project: MarMine

P.O. No.: 21UV20991

This report is for 8 samples of Pulp submitted to our lab in Pitea, Sweden on 17-MAR-2021.

The following have access to data associated with this certificate:

| | | |
|---|---|---|
| KURT AASLY | ANNE HYLSETH | |

## SAMPLE PREPARATION

| ALS CODE | DESCRIPTION |
|---|---|
| WEI-21 | Received Sample Weight |
| LOG-24 | Pulp Login - Rcd w/o Barcode |
| PUL-31 | Pulverize up to 250g 85% <75 um |
| LOG-QC | QC Test on Received Samples |

## ANALYTICAL PROCEDURES

| ALS CODE | DESCRIPTION | INSTRUMENT |
|---|---|---|
| MS41L-REE | REE Add-on to ME-MS41L | |
| ME-MS41L | Super Trace Lowest DL AR by ICP-MS | |

This is the Final Report and supersedes any preliminary report with this certificate number.Results apply to samples as submitted.All pages of this report have been checked and approved for release.

***** See Appendix Page for comments regarding this certificate *****

**Signature:**

Andrey Tairov, Technical Manager, Ireland

Comments: Samples were received on 17-Mar-2021 and the SSF/Request on 15-Mar-2021. Pulverization added due to Pulp QC failure. No PUL-QC test performed on these samples after pulverization due to the low received weight.

ALS Scandinavia AB
Hammarvagen 22
SE-943 36, Ojebyn
www.alsglobal.com/geochemistry

To: NTNU
SEM SELANDSVEI 1
NO-7491 TRONDHEIM
NORWAY



Project: MarMine

# CERTIFICATE OF ANALYSIS PI21064020

| Sample Description / Method / Analyte / Units / LOD | WEI-21 Recvd Wt. kg 0.02 | LOG-QC Pass75um % 0.01 | ME-MS41L Au ppm 0.0002 | ME-MS41L Ag ppm 0.001 | ME-MS41L Al % 0.01 | ME-MS41L As ppm 0.01 | ME-MS41L B ppm 10 | ME-MS41L Ba ppm 0.5 | ME-MS41L Be ppm 0.01 | ME-MS41L Bi ppm 0.0005 | ME-MS41L Ca % 0.01 | ME-MS41L Cd ppm 0.001 | ME-MS41L Ce ppm 0.003 | ME-MS41L Co ppm 0.001 | ME-MS41L Cr ppm 0.01 |
|---|---|---|---|---|---|---|---|---|---|---|---|---|---|---|---|
| 10007-1 | <0.02 | | 0.184 | 2.19 | 0.73 | 85.8 | 70 | 573 | 0.34 | 5.51 | 0.23 | 2.15 | 1.420 | 9.83 | 3.14 |
| 10007-2 | <0.02 | | 0.174 | 2.61 | 0.79 | 74.7 | 60 | 164.5 | 0.30 | 5.27 | 0.26 | 3.06 | 0.713 | 11.80 | 3.14 |
| 10007-3 | <0.02 | | 0.153 | 2.20 | 0.62 | 59.8 | 50 | 138.5 | 0.33 | 6.01 | 0.26 | 5.53 | 0.689 | 8.66 | 4.50 |
| 10007-4 | <0.02 | | 2.64 | 46.1 | 0.37 | 505 | 50 | 111.0 | 0.15 | 9.07 | 0.43 | 8.89 | 1.695 | 15.60 | 23.0 |
| 10008-1 | 0.02 | | 0.305 | 7.85 | 0.47 | 117.0 | 30 | 33.3 | 0.23 | 8.87 | 1.07 | 23.0 | 0.182 | 27.6 | 1.81 |
| 10008-2 | <0.02 | 52.0 | 0.355 | 9.88 | 0.44 | 131.5 | 40 | 40.4 | 0.22 | 9.58 | 2.42 | 27.8 | 0.275 | 40.2 | 1.84 |
| 10036 | <0.02 | | 0.0014 | 0.117 | 2.20 | 36.9 | 100 | 363 | 1.48 | 0.348 | 1.27 | 0.105 | 109.5 | 22.8 | 24.2 |
| 10037 | 0.02 | | 0.0014 | 0.009 | 2.01 | 26.1 | 50 | 101.5 | 0.95 | 0.259 | 1.24 | 0.046 | 49.4 | 17.35 | 39.8 |

Comments: Samples were received on 17-Mar-2021 and the SSF/Request on 15-Mar-2021. Pulverization added due to Pulp QC failure. No PUL-QC test performed on these samples after pulverization due to the low received weight.

***** See Appendix Page for comments regarding this certificate *****

ALS Scandinavia AB
Hammarvagen 22
SE-943 36, Ojebyn
www.alsglobal.com/geochemistry

To: NTNU
SEM SELANDSVEI 1
NO-7491 TRONDHEIM
NORWAY


Finalized Date: 2-APR-2021
Account: MINGOR

Project: MarMine

# CERTIFICATE OF ANALYSIS PI21064020

| Sample Description | Method | ME-MS41L | ME-MS41L | ME-MS41L | ME-MS41L | ME-MS41L | ME-MS41L | ME-MS41L | ME-MS41L | ME-MS41L | ME-MS41L | ME-MS41L | ME-MS41L | ME-MS41L | ME-MS41L | ME-MS41L |
|---|---|---|---|---|---|---|---|---|---|---|---|---|---|---|---|---|
| | Analyte | Cs | Cu | Fe | Ga | Ge | Hf | Hg | In | K | La | Li | Mg | Mn | Mo | Na |
| | Units | ppm | ppm | % | ppm | ppm | ppm | ppm | ppm | % | ppm | ppm | % | ppm | ppm | % |
| | LOD | 0.005 | 0.01 | 0.001 | 0.004 | 0.005 | 0.002 | 0.004 | 0.005 | 0.01 | 0.002 | 0.1 | 0.01 | 0.1 | 0.01 | 0.001 |
| 10007-1 | | 0.402 | 4960 | 9.52 | 8.72 | 0.697 | 0.021 | 2.88 | 0.036 | 0.09 | 0.789 | 79.6 | 12.15 | 513 | 11.35 | 0.614 |
| 10007-2 | | 0.340 | 5860 | 8.43 | 9.36 | 0.651 | 0.012 | 2.41 | 0.050 | 0.09 | 0.417 | 81.1 | 12.20 | 485 | 6.29 | 0.736 |
| 10007-3 | | 0.379 | 4750 | 8.09 | 8.04 | 0.663 | 0.016 | 2.14 | 0.033 | 0.07 | 0.400 | 83.7 | 12.00 | 498 | 6.01 | 0.520 |
| 10007-4 | | 0.240 | 4250 | 8.73 | 4.31 | 0.527 | 0.029 | 3.55 | 0.017 | 0.05 | 0.500 | 35.6 | 5.27 | 1450 | 21.7 | 0.186 |
| 10008-1 | | 0.227 | >10000 | 17.30 | 6.27 | 1.095 | 0.011 | 3.57 | 0.062 | 0.05 | 0.072 | 53.4 | 9.31 | 522 | 6.96 | 0.551 |
| 10008-2 | | 0.220 | >10000 | 19.60 | 5.77 | 1.200 | 0.013 | 4.50 | 0.106 | 0.05 | 0.119 | 50.0 | 8.62 | 652 | 4.59 | 0.455 |
| 10036 | | 2.20 | 50.1 | 9.14 | 6.02 | 0.228 | 0.209 | 0.123 | 0.053 | 0.69 | 32.0 | 45.0 | 0.55 | 809 | 15.45 | 0.647 |
| 10037 | | 1.660 | 39.5 | 3.89 | 6.56 | 0.103 | 0.243 | 0.072 | 0.049 | 0.54 | 19.15 | 36.6 | 0.88 | 632 | 2.22 | 0.643 |

Comments: Samples were received on 17-Mar-2021 and the SSF/Request on 15-Mar-2021. Pulverization added due to Pulp QC failure. No PUL-QC test performed on these samples after pulverization due to the low received weight.

***** See Appendix Page for comments regarding this certificate *****

ALS Scandinavia AB
Hammarvagen 22
SE-943 36, Ojebyn
www.alsglobal.com/geochemistry

To: NTNU
SEM SELANDSVEI 1
NO-7491 TRONDHEIM
NORWAY


Finalized Date: 2-APR-2021
Account: MINGOR

Project: MarMine

# CERTIFICATE OF ANALYSIS PI21064020

| Sample Description | Method | ME-MS41L | ME-MS41L | ME-MS41L | ME-MS41L | ME-MS41L | ME-MS41L | ME-MS41L | ME-MS41L | ME-MS41L | ME-MS41L | ME-MS41L | ME-MS41L | ME-MS41L | ME-MS41L | ME-MS41L |
|---|---|---|---|---|---|---|---|---|---|---|---|---|---|---|---|---|
| | Analyte | Nb | Ni | P | Pb | Pd | Pt | Rb | Re | S | Sb | Sc | Se | Sn | Sr | Ta |
| | Units | ppm | ppm | % | ppm | ppm | ppm | ppm | ppm | % | ppm | ppm | ppm | ppm | ppm | ppm |
| | LOD | 0.002 | 0.04 | 0.001 | 0.005 | 0.001 | 0.002 | 0.005 | 0.0002 | 0.01 | 0.005 | 0.005 | 0.003 | 0.01 | 0.01 | 0.005 |
| 10007-1 | | 0.010 | 1.82 | 0.054 | 271 | 0.005 | <0.002 | 3.40 | 0.0002 | 0.90 | 1.460 | 1.810 | 29.4 | 2.50 | 118.5 | <0.005 |
| 10007-2 | | 0.003 | 2.13 | 0.034 | 201 | 0.001 | 0.002 | 2.70 | 0.0002 | 1.44 | 1.235 | 1.790 | 31.5 | 2.07 | 138.5 | <0.005 |
| 10007-3 | | 0.003 | 3.13 | 0.030 | 189.5 | 0.001 | <0.002 | 2.54 | 0.0002 | 1.75 | 1.125 | 1.615 | 32.5 | 2.22 | 132.0 | <0.005 |
| 10007-4 | | 0.022 | 25.5 | 0.035 | 1280 | 0.002 | <0.002 | 1.705 | 0.0006 | 2.44 | 17.20 | 1.075 | 46.5 | 13.85 | 256 | <0.005 |
| 10008-1 | | 0.003 | 1.52 | 0.011 | 533 | 0.001 | <0.002 | 1.595 | 0.0006 | 10.00 | 2.91 | 1.225 | 170.5 | 4.26 | 177.5 | <0.005 |
| 10008-2 | | 0.002 | 0.97 | 0.007 | 637 | 0.006 | <0.002 | 1.460 | 0.0007 | >10.0 | 3.68 | 1.075 | 211 | 4.74 | 270 | <0.005 |
| 10036 | | 0.103 | 99.1 | 0.386 | 24.6 | <0.001 | 0.002 | 38.1 | 0.0023 | 1.12 | 0.898 | 11.25 | 0.873 | 0.83 | 270 | <0.005 |
| 10037 | | 0.360 | 39.1 | 0.085 | 17.15 | 0.004 | <0.002 | 32.5 | 0.0002 | 0.05 | 0.428 | 6.92 | 0.242 | 0.95 | 76.3 | <0.005 |

Comments: Samples were received on 17-Mar-2021 and the SSF/Request on 15-Mar-2021. Pulverization added due to Pulp QC failure. No PUL-QC test performed on these samples after pulverization due to the low received weight.

***** See Appendix Page for comments regarding this certificate *****

ALS Scandinavia AB
Hammarvagen 22
SE-943 36, Ojebyn
www.alsglobal.com/geochemistry

To: NTNU
SEM SELANDSVEI 1
NO-7491 TRONDHEIM
NORWAY


Finalized Date: 2-APR-2021
Account: MINGOR

Project: MarMine

# CERTIFICATE OF ANALYSIS PI21064020

| Sample Description | Method | ME-MS41L | ME-MS41L | ME-MS41L | ME-MS41L | ME-MS41L | ME-MS41L | ME-MS41L | ME-MS41L | ME-MS41L | ME-MS41L | MS41L-REE | MS41L-REE | MS41L-REE | MS41L-REE | MS41L-REE |
|---|---|---|---|---|---|---|---|---|---|---|---|---|---|---|---|---|
| | Analyte | Te | Th | Ti | Tl | U | V | W | Y | Zn | Zr | Dy | Er | Eu | Gd | Ho |
| | Units | ppm | ppm | % | ppm | ppm | ppm | ppm | ppm | ppm | ppm | ppm | ppm | ppm | ppm | ppm |
| | LOD | 0.003 | 0.002 | 0.001 | 0.001 | 0.005 | 0.1 | 0.001 | 0.003 | 0.1 | 0.01 | 0.002 | 0.002 | 0.002 | 0.002 | 0.001 |
| 10007-1 | | 1.585 | 0.167 | 0.003 | 1.445 | 2.42 | 68.7 | 0.072 | 1.155 | 1735 | 1.00 | 0.162 | 0.085 | 0.228 | 0.171 | 0.032 |
| 10007-2 | | 1.420 | 0.080 | 0.002 | 1.165 | 1.920 | 38.1 | 0.053 | 0.757 | 1635 | 0.64 | 0.081 | 0.053 | 0.203 | 0.088 | 0.019 |
| 10007-3 | | 1.480 | 0.070 | 0.001 | 1.100 | 1.745 | 33.1 | 0.078 | 0.663 | 2150 | 0.75 | 0.083 | 0.049 | 0.220 | 0.085 | 0.016 |
| 10007-4 | | 2.14 | 0.087 | 0.005 | 4.48 | 2.08 | 59.5 | 0.176 | 1.440 | 3710 | 1.65 | 0.224 | 0.123 | 0.170 | 0.255 | 0.046 |
| 10008-1 | | 4.84 | 0.009 | <0.001 | 4.44 | 2.55 | 9.4 | 0.063 | 0.252 | 6690 | 0.31 | 0.027 | 0.020 | 0.171 | 0.030 | 0.009 |
| 10008-2 | | 6.19 | 0.019 | 0.001 | 5.68 | 2.55 | 6.5 | 0.096 | 0.281 | 8030 | 0.50 | 0.034 | 0.021 | 0.203 | 0.035 | 0.008 |
| 10036 | | 0.263 | 8.85 | 0.010 | 0.245 | 6.49 | 90.9 | 0.093 | 95.1 | 103.0 | 9.57 | 13.10 | 7.20 | 2.88 | 14.65 | 2.57 |
| 10037 | | 0.081 | 7.87 | 0.040 | 0.170 | 0.784 | 83.3 | 0.086 | 12.80 | 91.3 | 10.40 | 2.74 | 1.180 | 0.918 | 3.93 | 0.469 |

Comments: Samples were received on 17-Mar-2021 and the SSF/Request on 15-Mar-2021. Pulverization added due to Pulp QC failure. No PUL-QC test performed on these samples after pulverization due to the low received weight.

***** See Appendix Page for comments regarding this certificate *****

ALS Scandinavia AB
Hammarvagen 22
SE-943 36, Ojebyn
www.alsglobal.com/geochemistry

To: NTNU
SEM SELANDSVEI 1
NO-7491 TRONDHEIM
NORWAY


Finalized Date: 2-APR-2021
Account: MINGOR

Project: MarMine

# CERTIFICATE OF ANALYSIS PI21064020

| Sample Description | Method | MS41L-REE | MS41L-REE | MS41L-REE | MS41L-REE | MS41L-REE | MS41L-REE | MS41L-REE |
|---|---|---|---|---|---|---|---|---|
| | Analyte | Lu | Nd | Pr | Sm | Tb | Tm | Yb |
| | Units | ppm | ppm | ppm | ppm | ppm | ppm | ppm |
| | LOD | 0.001 | 0.002 | 0.002 | 0.002 | 0.001 | 0.001 | 0.002 |
| 10007-1 | | 0.014 | 0.792 | 0.203 | 0.138 | 0.024 | 0.015 | 0.087 |
| 10007-2 | | 0.010 | 0.404 | 0.110 | 0.087 | 0.015 | 0.008 | 0.058 |
| 10007-3 | | 0.008 | 0.390 | 0.104 | 0.080 | 0.013 | 0.008 | 0.051 |
| 10007-4 | | 0.018 | 1.095 | 0.259 | 0.232 | 0.038 | 0.018 | 0.125 |
| 10008-1 | | 0.005 | 0.107 | 0.028 | 0.027 | 0.005 | 0.004 | 0.023 |
| 10008-2 | | 0.004 | 0.134 | 0.039 | 0.033 | 0.007 | 0.003 | 0.026 |
| 10036 | | 0.754 | 49.5 | 11.50 | 12.25 | 2.12 | 0.879 | 5.59 |
| 10037 | | 0.114 | 21.7 | 5.59 | 4.53 | 0.514 | 0.142 | 0.888 |

Comments: Samples were received on 17-Mar-2021 and the SSF/Request on 15-Mar-2021. Pulverization added due to Pulp QC failure. No PUL-QC test performed on these samples after pulverization due to the low received weight.

***** See Appendix Page for comments regarding this certificate *****

ALS Scandinavia AB
Hammarvagen 22
SE-943 36, Ojebyn
www.alsglobal.com/geochemistry

To: **NTNU**
**SEM SELANDSVEI 1**
**NO-7491 TRONDHEIM**
**NORWAY**


**Finalized Date: 2-APR-2021**
**Account: MINGOR**

Project: MarMine

# CERTIFICATE OF ANALYSIS PI21064020

## CERTIFICATE COMMENTS

### ANALYTICAL COMMENTS

Applies to Method: Gold determinations by this method are semi-quantitative due to the small sample weight used (0.5g).
ME-MS41L

### LABORATORY ADDRESSES

Applies to Method: Processed at ALS Pitea located at Hammarvagen 22, SE-943 36, Ojebyn, Sweden.
LOG-24 LOG-QC PUL-31 WEI-21

Applies to Method: Processed at ALS Loughrea located at Dublin Road, Loughrea, Co. Galway, Ireland.
ME-MS41L MS41L-REE

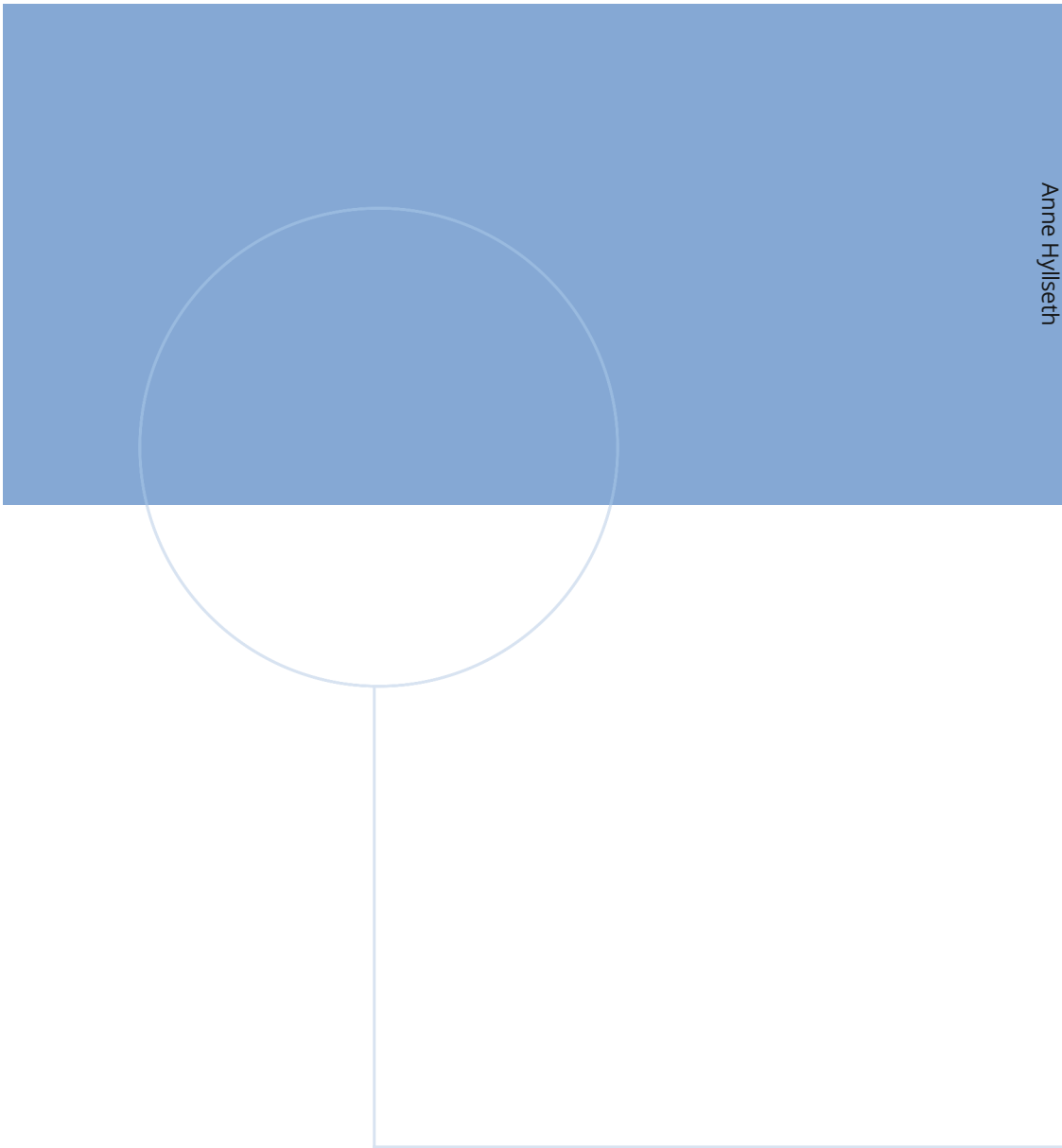

Anne Hyllseth

NTNU
Norwegian University of
Science and Technology